Experimental Coherent X-Ray Diffractive Imaging:

Capabilities and Limitations of the Technique

Dissertation
zur Erlangung des Doktorgrades
des Department Physik
der Universität Hamburg

vorgelegt von
Andreas Schropp
aus Freiburg i. Br.

Hamburg
2008

Gutachter der Dissertation:	Prof. Dr. E. Weckert
	Prof. Dr. C. G. Schroer
Gutachter der Disputation:	Prof. Dr. E. Weckert
	Prof. Dr. W. Wurth
Datum der Disputation:	May 28th, 2008
Vorsitzender des Prüfungsausschusses:	Dr. K. Petermann
Vorsitzender des Promotionsausschusses:	Prof. Dr. J. Bartels
Dekan der Fakultät für Mathematik, Informatik und Naturwissenschaften:	Prof. Dr. A. Frühwald

Abstract

Since the experimental demonstration that the inversion of sufficiently sampled continuous diffraction data is possible [Mia99] the method of coherent x-ray diffractive imaging (CXDI) gained a strong interest in x-ray science as a candidate for high-resolution microscopy. In the meantime different successful and promising experiments were reported using soft [Cha06a, Cha06b, Thi06] and hard x rays [Mia02, Mia03a, Mia06, Pfe06, Jia08]. The great appeal of the method is that it is purely based on diffraction rather than focusing and, therefore, the achievable resolution depends only on the wavelength and the largest scattering angle where a statistically significant signal can be measured.

The investigations pursued during this work were focused on the testing of the applicability of the CXDI-method in the hard x-ray regime and different measurements were carried out at photon energies between 7 keV and 10 keV. Obviously, the motivation to use these energies is related to the fact that only at higher energies sub-nanometer resolution might be possible in the future. The samples investigated were lithographically prepared two-dimensional gold structures with a size ranging from 3 µm to 10 µm as well as a cluster of gold spheres with a lateral extension of about 3.5 µm. Continuous diffraction patterns were recorded in small angle scattering geometry. In some of the measurements a scattering signal up to the edge of the detector could be measured which corresponds to a lateral resolution of about 30 nm. For certain samples it was possible to reconstruct the object from the measured diffraction data.
However, at these energies several experimental challenges were encountered concerning missing low-resolution data and partial coherence effects. The former aspect is related to a certain degree of indetermination of low spatial frequencies of the object and it is often very difficult to recover this information by state-of-the-art reconstruction algorithms. The latter involves the reduced visibility of diffraction fringes which is not properly taken into account by current reconstruction algorithms [Var01]. The influence of these effects on the result of a reconstruction as well as the definition of resolution for a given photon flux is thoroughly discussed in this work.
Since the scattered intensity of non-periodic objects is weak at large scattering angles, the available photon flux is finally the main limitation of the method with regard to the achievable resolution [Say98, Wil07]. The experimental data were used to get an estimate of photon flux required for sub-nanometer resolution.

The ptychographic iterative phase retrieval algorithm proposed by J. M. Rodenburg et al. [Rod04] was implemented and tested on simulated diffraction data. Due to the possibility to image extended objects this method is very promising for future applications. Additionally, a genetic algorithm has been developed and implemented for phase retrieval. This algorithm is very different from state-of-the-art algorithms and allows to introduce further experimentally important parameters such as a certain illumination function and partial coherence of the x-ray light.

Zusammenfassung

Seit dem experimentellen Nachweis, dass die Phasenrekonstruktion von Intensitätsdaten von nicht-periodischen Objekten möglich ist [Mia99], wird die sogenannte Beugungsmikroskopie mit kohärenter Röntgenstrahlung als eine vielversprechende Abbildungsmethode mit hoher räumlicher Auflösung gehandelt. In der Zwischenzeit wurden weitere erfolgreiche Experimente im weichen [Cha06a, Cha06b, Thi06] und harten [Mia02, Mia03a, Mia06, Pfe06, Jia08] Bereich der Röntgenstrahlung durchgeführt. Der große Vorteil dieser Methode ist, dass sie ausschließlich auf dem Prinzip der Röntgenbeugung basiert. Aus diesem Grund ist die räumliche Auflösung im Prinzip nur von der verwendeten Energie der Röntgenstrahlung sowie dem größten Streuwinkel, bei dem ein statistisch signifikantes Signal detektiert werden konnte, abhängig.

Die Untersuchungen dieser Arbeit beschäftigen sich im Wesentlichen mit der Anwendbarkeit dieser Methode im harten Bereich der Röntenstrahlung und verschiedene Experimente wurden bei Photonenenergien zwischen 7 keV und 10 keV durchgeführt. Die Motivation hierfür liegt darin begründet, dass nur bei höheren Photonenenergien schlussendlich auch eine hohe Auflösung erreichbar ist. Bei den verwendeten Proben handelte es sich um lithographisch hergestellte, zwei-dimensionale Strukturen aus Gold, deren Größe im Bereich zwischen 3 µm und 10 µm lag, sowie einem Goldkügelchen-Cluster. Von diesen Proben wurden Beugungsbilder mit kontinuierlicher Intensitätsverteilung in Kleinwinkelstreugeometrie gemessen. Bei bestimmten Proben war es unter gewissen Einschränkungen möglich, deren Struktur aus dem gemessenen Beugungsbild zu rekonstruieren. Allerdings treten bei diesen Energien experimentelle Schwierigkeiten auf, die hauptsächlich mit dem Verlust von Daten im zentralen Bereich des Beugungsbildes sowie einer Verschlechterung des Kontrastes im Beugungsbild, hervorgerufen durch eine partiell kohärente Beleuchtung, einhergehen. Der erste Aspekt ist mit dem Verlust an Information betreffend langer räumlicher Frequenzen der Probe begleitet, der meist nur sehr schwer von aktuellen Algorithmen rekonstruiert werden kann. Die partielle Kohärenz andererseits bereitet Schwierigkeiten, da sie im Modell der Rekonstruktion bisher nicht berücksichtigt wird [Var01]. Der Einfluss dieser Effekte wird im Rahmen dieser Arbeit sorgfältig an gemessenen und simulierten Intensitätsdaten diskutiert.

Ein weiterer wichtiger Aspekt ist die Abhängigkeit der Auflösung von der insgesamt vorhandenen Zahl der Photonen. Es zeigt sich, da die Streueffizienz zu großen Winkeln stark abfällt, dass dieses Kriterium schlussendlich die Auflösung limitiert [Say98, Wil07]. Anhand der gemessenen Daten lässt sich der Photonenfluss abschätzen, der notwendig wäre, um sub-nanometer Auflösungen erreichen zu können.
Weiterhin wurde der Ptychographie-Algorithmus, vorgeschlagen von Rodenburg et al. [Rod04], implementiert, sowie ein genetischer Algorithmus zur Phasenrekonstruktion entwickelt. Die Ptychographie-Methode ist geeignet für das Abbilden von größeren Proben und ist aus diesem Grund, sowie auch aufgrund sehr guter Konvergenzeigenschaften, sehr vielversprechend für zukünftige Anwendungen der hochauflösenden Röntgenmikroskopie.

Contents

1 Introduction

Microscopy is a fascinating field of science allowing for the visualization of the two- or three-dimensional structure of an object. This knowledge is very useful for the description and understanding of physical processes occurring on short length scales. One example is optical light microscopy which is widely used in life science for characterization of biological samples. In this field confocal microscopy which is able to extract information on the three-dimensional structure as well as stimulated emission-depletion-microscopy (STED) [Hel94] which is able to overcome the diffraction limit are important microscopic methods. Electron microscopy on the other hand allows for imaging applications with very high resolution. Nevertheless, due to the strong interaction of electrons with matter the penetration depth of electrons is small and only thin samples or their surfaces can be investigated with transmission electron microsopy (TEM) or scanning electron microscopy (SEM).

The use of x rays, i.e., photons with an energy ranging from a few hundred eV to more than 100 keV, to probe structural information with very high lateral resolution is the natural extension of optical light microscopy. X rays are especially important for structure determination at the atomic length scale since firstly, their wavelength is comparable to typical inter-atomic distances and secondly, their weak interaction with matter allows to extract information of the inner structure of opaque objects without destructive sample preparation. This weak interaction was already described by W. C. Röntgen when he presented his discovery of a new kind of radiation in 1895 [Rön95]. In the first experiments with x rays he could not find any indication of refraction or diffraction of the unknown radiation on prism optics or glass lenses but characterized primarily the absorption of the radiation by different materials. However, today it is well known that the index of refraction n is not equal to unity for x rays but slightly smaller, e.g. $n \approx 1 - 10^{-6}$ for 10 keV photon energy. This means, x rays are also refracted by matter, though refraction effects are very small. For this reason, designing an imaging lens as it is known in optical light microscopy is difficult for x rays.
Despite this, various focusing optics that are required for image formation exist today. They are based on physical effects such as diffraction on crystals and artificial gratings, external total reflection and refraction: namely Fresnel zone plates, bent crystal optics, waveguides, Kirkpatrick-Baez-mirrors, and refractive lenses. Fresnel zone plates are among the most successful devices for photon energies lower than about 2 keV. They allow for image formation with a lateral resolution smaller than 20 nm in the soft x-ray regime [Jac99, Cha05]. Nevertheless, the diffraction efficiency of Fresnel zone plates decreases quickly for harder x rays. Recent work to increase the efficiency in the hard x-ray regime is presented in [Jef07]. In the hard x-ray regime focal spot sizes of 20 nm

to 50 nm could be achieved by multilayer Laue optics, Kirkpatrick-Baez-mirrors and refractive lenses [Kan06, Mim05, Sch05].

In order to overcome these resolution limits which are related to technical challenges in the fabrication of these optical elements, a relatively new method, known as coherent x-ray diffractive imaging (CXDI), is discussed as a candidate for high-resolution x-ray imaging. The advantage of the method is that no optical components are used which could limit the resolution. It is purely based on diffraction and, therefore, the resolution is directly related to the largest diffraction angle where a statistically significant signal can be recorded. A coherent illumination of the specimen is required since only in this case a characteristic speckle pattern is created which is suitable for the recovery of the structure of the object. This implies that presently only synchrotron radiation sources of the third generation, such as the European Synchrotron Radiation Facility (ESRF), are appropriate for this kind of experiment. At these sources, the lateral coherence length can exceed a few tens of micrometers which is large enough to coherently illuminate small samples with a size of a few microns. In a small angle scattering geometry the diffraction pattern of such a small, non-periodic, object is not concentrated in distinct Bragg-reflections, as it is the case for crystalline samples, but is distributed over a large area in reciprocal space.
The main challenge at hand is that structure determination requires the knowledge of the phase of the diffracted field. However, this phase is not directly measurable but has to be recovered numerically with iterative computational methods. The feasibility of phase recovery from amplitude measurements in both real- and reciprocal-space was first proven by Gerchberg and Saxton in 1972 [Ger72]. A modification of this algorithm was presented by Fienup in 1978 allowing one to recover the phase from the amplitude of the measured diffraction pattern only. However, it is necessary to apply certain constraints in object space [Fie78]. In some sense, these algorithms adopt the role of an objective lens as it is used in a standard optical microscope.
First experimental evidence that coherent x-ray microscopy of a non-periodic, micrometer-sized object is possible was given by J. Miao et al. in 1999 using soft x rays ($E = 730\,\mathrm{eV}$) [Mia99, Mia00a]. Since then, a lot of effort was spent to improve and verify this so-called lensless imaging method. Major progress was demonstrated in the soft x-ray regime by imaging of an unstained yeast cell ($E = 750\,\mathrm{eV}$) [Sha05, Thi06] and of three-dimensional test structures [Cha06b]. In the hard x-ray regime a three-dimensional reconstruction of a GaN-quantum dot particle was reported by J. Miao et al. ($E = 5\,\mathrm{keV}$) [Mia05, Mia06] as well as the imaging of *Escherichia coli bacteria* ($E = 6.2\,\mathrm{keV}$) [Mia03a]. The three-dimensional mapping of a deformation field inside a nano-crystal using phase retrieval techniques was reported by M. A. Pfeifer et al. ($E = 9\,\mathrm{keV}$) [Pfe06]. In this contribution the continuous diffraction patterns were not measured in forward scattering geometry but instead around the (111)-Bragg reflection. First experiments with short VUV-laser pulses were carried out by H. Chapman et al. [Cha06a], and different scientific cases as well as possible applications of the CXDI-method at upcoming x-ray sources like the European X-Ray Free Electron Laser (XFEL) and the Linac Coherent Light Source (LCLS) are for example presented by I. Vartanyants et al. [Var07].

In this thesis the applicability of the CXDI-method in the hard x-ray regime has been investigated. For this purpose different CXDI-experiments on lithographically prepared samples were carried out in small angle scattering geometry at the ESRF using hard x rays between 7 keV and 10 keV photon energy. Obviously, the motivation to carry out these experiments is ultimately driven by the fact that only at higher photon energies atomic resolution imaging may be achievable.

However, at these energies further experimental challenges were encountered. One of them is the proper measurement of low frequency information contained in the central part of the diffraction pattern. In the forward scattering geometry it is necessary to use a beam-stop to block the direct x-ray beam and, typically, a certain amount of diffracted intensity is also covered by the beam-stop. This problem becomes more severe at higher photon energies. Additionally, around the beam-stop a parasitic scattering signal related to scattering from optical components upstream or a certain contribution of higher harmonic photons smears the diffraction signal of the sample. The missing low resolution data often makes the reconstruction of the object difficult. Another difficulty is related to a smaller coherence length which is responsible for a reduced contrast in visibility of diffraction fringes. The lower contrast is not properly treated by current reconstruction algorithms and leads to artifacts in the result of a reconstruction. Different reconstruction results obtained both from simulated and measured diffraction data will be presented in this work in order to illustrate the influence of partial coherence and missing low resolution information in CXDI-experiments.

During this work the so-called ptychographic reconstruction method [Rod04] has been numerically implemented. In difference to other reconstruction algorithms this method does rely on the measurement of multiple diffraction patterns that were recorded from different parts of the object. The area of the object that is contributing to a single diffraction pattern is defined by a certain illumination wave front. In case that there is an overlap between different illuminated areas, the reconstruction of the object is working very efficiently. A main advantage of this method is that also extended objects with a size larger than the coherence length of the incoming light can be imaged.
Furthermore, a so-called genetic algorithm has been developed for phase retrieval. It is especially interesting if further experimental parameters such as the influence of partially coherent light has to be considered in the reconstruction model. Different reconstruction results and limitations of these algorithms are presented in Chap. 5.

The remainder of this work is organized as follows. Chap. 2 provides the theoretical background for coherent x-ray diffraction. It describes predominantly the coherence properties of x-ray radiation at synchrotron radiation sources, the interaction between x rays and matter, wave propagation in free space and gives an overview of different state-of-the-art reconstruction algorithms. In Chap. 3 technical details of the experimental setup, designed and constructed during this work, are presented. The setup is especially adapted to the CXDI-method allowing for the positioning of the sample with a precision

of 10 nm. Chap. 4 is devoted to the presentation of experimental data measured at the ESRF. Parameters like partial coherence and photon flux are estimated for the different experimental environments, specially for the beamlines ID01 and ID10C of the ESRF, where experimental data were collected. In Chap. 5 numerical simulations concerning the relation between photon flux and achievable resolution as well as the influence of partial coherence on the reconstruction result are discussed. In Chap. 6 reconstruction results from the measured data are presented. The discussion is focused on the influence of missing low frequency data. Chap. 7 summarizes the most significant findings.

2 Theoretical Background

In this chapter a brief introduction into the field of x-ray microscopy based on the method of coherent x-ray diffractive imaging (CXDI) is presented. Various physical aspects related to the method, including the properties of synchrotron radiation, propagation and partial coherence of electromagnetic wave fields, x ray – matter interaction, and different phase retrieval algorithms will be introduced.

2.1 Lensless Coherent Imaging

In Fig. 2.1 a schematic drawing of the setup as it is used in coherent x-ray diffraction experiments in the small angle scattering geometry is shown.

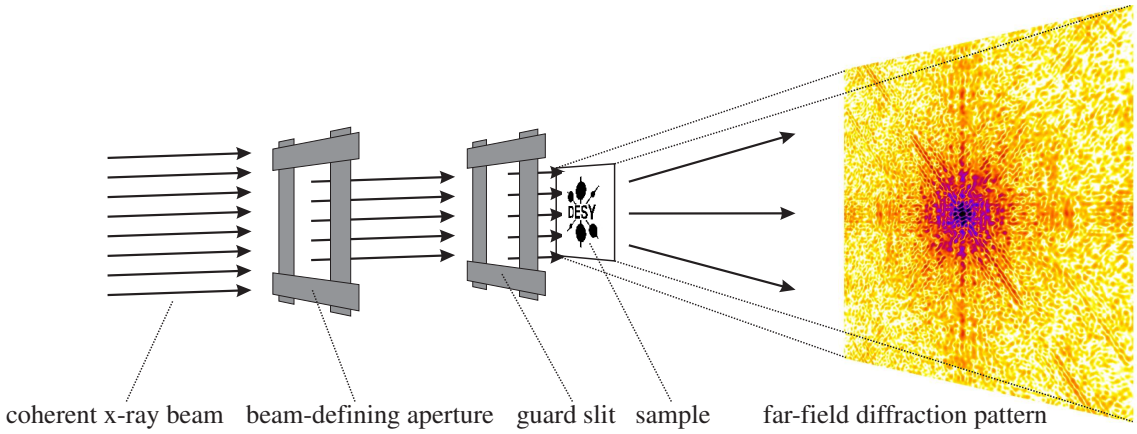

Figure 2.1: Generic setup used in lensless imaging experiments.

The setup consists of different slit-systems upstream of the sample which are used in order to select a coherent portion of the x-ray beam as well as a detector positioned in the far-field regime of the sample at the given wavelength. The detector is used to measure the Fraunhofer diffraction pattern of the sample which is in this geometry just proportional to the Fourier-transform of the electron density of the object. Apart from a beam-stop which is positioned closely in front of the detector in order to block the direct x-ray beam no other optical components are introduced.
If the incoming wave field is coherent over the size of the sample, i.e., the lateral coherence length is much larger than the sample size, a typical interference pattern will be produced containing all the information about the exit wave field after the sample. Since the CXDI-method relies on the coherent illumination of the sample this kind of

experiment has not been feasible with x rays until the construction of modern third generation x-ray sources with high brilliance (cf. Sec. 2.2 and Sec. 2.6).
The CXDI-method is based on free propagation of the wave field from the exit surface of the sample to the detector. In Sec. 2.3 and Sec. 2.4 details concerning free-space propagation of a complex wave field and the calculation of the transmission function of a thin object are presented. Since no optical components between sample and detector are used in this imaging setup the achievable spatial resolution of the reconstructed image is only limited by the wavelength of the x-ray radiation and the largest diffraction angle where a statistically significant signal can be measured. Therefore, the resolution in CXDI-experiments can, at least in principle, be diffraction limited.

The main difficulty of CXDI-microscopy is that the phase of the diffracted wave field can not be measured due to the high frequency ($\nu \approx 1.9 \cdot 10^{18}\,\mathrm{s}^{-1}$ for 8 keV photon energy) and the small wavelength of x rays. The only measurable quantity is the intensity, i.e., the modulus squared of the amplitude. Nevertheless, during the last decades a number of numerical phase retrieval methods have been developed which are able to recover this phase information only from the measured intensity [Fie78, Fie82]. This is feasible if the diffraction pattern is sufficiently sampled as compared to the Nyquist frequency of the sample (cf. Sec. 2.5 and Sec. 2.7). If this phase information is known the projection of the electron density of the object can be obtained by an inverse Fourier-transform of the diffraction pattern in the case of kinematical scattering.

In the following an overview of properties of synchrotron radiation is presented.

2.2 Synchrotron Radiation

Synchrotron radiation denotes the electromagnetic radiation that is produced when charged particles of relativistic energy are accelerated by external fields. These particles can be kept in a so-called storage ring and are forced to move on a closed orbit with a polygonal shape having round and straight sections. The magnetic structure deflecting the particles from the straight flight path is called a bending magnet (BM). It is one source of synchrotron radiation. Further magnetic devices, known as insertion devices (ID's), can be introduced in the straight sections of a storage ring. In this case, the structure of the magnetic field changes periodically in the direction of propagation of the particle forcing it to perform a nearly sinusoidal movement. Two types of magnetic structures have to be distinguished: undulators and wigglers. The main differences of the synchrotron light produced by these devices will be described in the following.

Due to the high velocity of the charged particles – close to the speed of light – the emitted radiation is concentrated in the forward direction of the particles' movement. This property of synchrotron radiation can be attributed to relativistic aberration. While the emitted radiation shows dipole characteristics in the reference frame of the electron (cf. Fig. 2.2(a)) this spatial distribution changes considerably after the Lorentz-

transformation to the laboratory frame (cf. Fig. 2.2(b)). The main part of the electromagnetic radiation is emitted into a small cone in forward direction with an angle of $\Theta \approx \gamma^{-1}$, where

$$\gamma = \frac{1}{\sqrt{1 - \left(\frac{v}{c}\right)^2}} = \frac{1}{\sqrt{1 - \beta^2}} \tag{2.1}$$

is a relativistic parameter and

$$\beta = \frac{v}{c} \approx 1 - \frac{1}{2\gamma^2}. \tag{2.2}$$

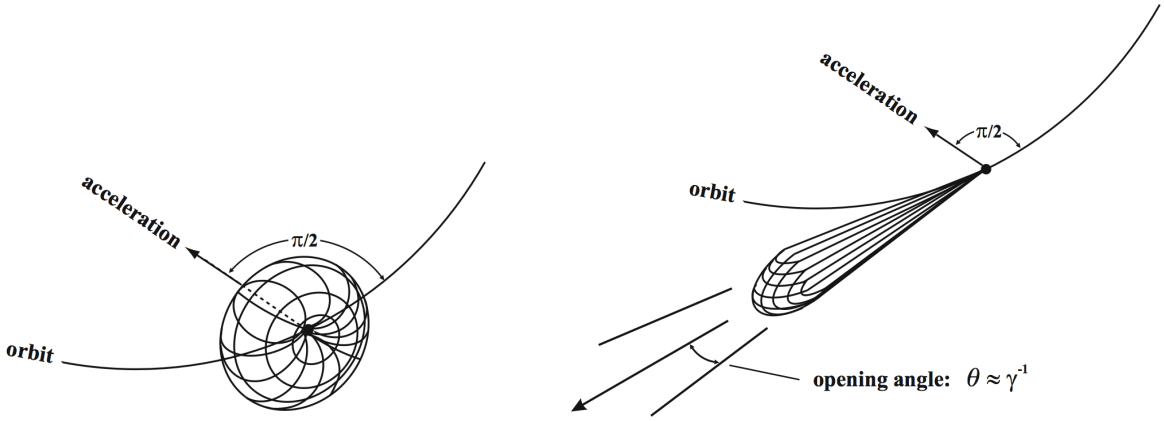

(a) non-relativistic electron **(b)** relativistic electron

Figure 2.2: Spatial distribution of emitted radiation for different electron energies [Len96, Ben05].

Modern synchrotron sources such as the European Synchrotron Radiation Facility (ESRF), the Advanced Photon Source (APS) and the Super Photon Ring-8 (SPring-8) operate at an electron energy of 6 GeV, 7 GeV, and 8 GeV, respectively. The value of γ for an electron with an energy of 6 GeV can easily be calculated by using the relativistic relation $E = \gamma m_e c^2$, where E is the energy, m_e is the rest mass of the electron and c is the speed of light, i.e., $\gamma = E/(m_e c^2) \approx 6000\,\text{MeV}/0.511\,\text{MeV} \approx 11750$. Therefore, the light is emitted into a cone with angle $\Theta \approx 0.085$ mrad for a 6 GeV electron-beam. This is valid for radiation of the bending magnet where no interference effects are present.
These so-called third generation x-ray sources are especially designed to produce synchrotron radiation and offer an x-ray beam with extraordinary properties like high brightness, small angular divergence and small source size. In order to define the quality of an x-ray source these parameters are combined in a quantity called brilliance. It is given by

$$\text{brilliance} = \frac{\text{photons/second}}{(\text{solid angle } [\text{mrad}^2])(\text{source area } [\text{mm}^2])(0.1\%\text{ bandwidth})}. \tag{2.3}$$

The larger the brilliance the more photons are available for imaging experiments.

Some details concerning the power of the emitted radiation of a Wiggler as well as some characteristics of the undulator are presented in the next paragraphs. In Fig. 2.3 an arrangement of a periodic magnetic structure is shown.

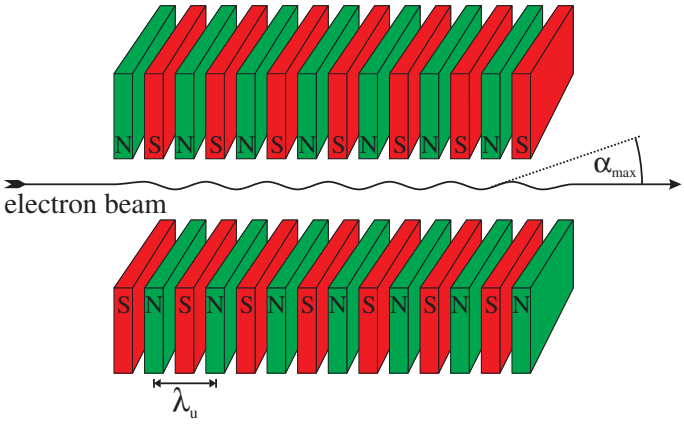

Figure 2.3: Electron beam passing an insertion device (ID).

An important parameter is the maximum deflection angle indicated by $\alpha_{\max}$. Typically, this angle is defined as a multiple of γ^{-1} and the device is then classified by a certain value of a factor κ given by $\kappa = \alpha_{\max} \cdot \gamma$. By changing the gap of the magnetic device the averaged magnetic field B_0 can be varied and as a result the value of κ can be adjusted. It is given by [AN01]

$$\kappa = \frac{e_0 B_0}{m_e c k_u} = 0.934 \cdot \lambda_u[\text{cm}] B_0[\text{T}], \tag{2.4}$$

where $k_u = 2\pi/\lambda_u$, λ_u is the period of the magnetic structure (cf. Fig. 2.3), e_0 is the charge of the electron, m_e is the mass of the electron and c is the speed of light in vacuum.

For a wiggler $\kappa \gtrsim 10$ [Tho01] and, hence, the radiation emitted from different magnetic periods is uncorrelated. The emitted intensity scales with $2N$, where N is the number of successive magnetic periods. In this case the intensity of the electromagnetic field of all produced photons is summed up. The radiated power of the wiggler is given by [AN01]

$$P[\text{kW}] = 0.633 \cdot E^2[\text{GeV}] B_0^2[\text{T}] L[\text{m}] I[\text{A}], \tag{2.5}$$

where E is the energy of the electron, L is the length of the whole device and I is the ring current. The radiated power of the wiggler is very large, typically in the order of kilowatts or more.

In the case of undulators the deviation angle $\alpha_{\max}$ is small, i.e. $\kappa \sim 1$. In this range interference effects become important and for certain wavelengths the probability ampli-

tudes related to the emission of photons from subsequent magnetic periods add constructively. This gives rise to an enhanced emission of radiation in narrow energy bands and the emitted intensity is proportional to N^2 at these special wavelengths. The condition for constructive interference is related to the period of the magnetic structure as well as the magnetic field B_0 which gives rise to a characteristic line spectrum. The wavelength of the j-th harmonic of the undulator is given by [Cla04]

$$\lambda_j(\vartheta) = \frac{\lambda_u}{2\gamma^2 \cdot j}\left(1 + \frac{\kappa^2}{2} + (\gamma\vartheta)^2\right), \tag{2.6}$$

where ϑ is the angle between the direction of observation and the undulator axis. The parameter κ depends on the magnetic field B_0. By changing the gap of the undulator the parameter κ can be varied and, therefore, the wavelength of the emitted radiation is tunable over a certain wavelength range as can be deduced from Eq. (2.6). The x-ray light of an undulator is polarized in the horizontal direction. Due to interference effects the angular divergence of the undulator x-ray light is smaller compared to the radiation of the wiggler or the bending magnet. For radiation emitted on-axis the angle $\Delta\vartheta$ where the emitted intensity falls to zero is given by [Cla04]

$$\Delta\vartheta = \frac{1}{\gamma}\sqrt{\frac{1 + \kappa^2/2}{j \cdot N}} \approx 0.16 \cdot \frac{1}{\gamma}, \tag{2.7}$$

for an undulator with $N = 33$ periods and $\kappa = 1.28$.

The size $\sigma_{h,v}$ and the divergence $\sigma'_{h,v}$ of the electron beam in the horizontal and vertical directions are important parameters defining the quality of an x-ray source. The product of them is denoted as the emittance ε of the source, e.g. in horizontal direction $\varepsilon_h = \sigma_h\sigma'_h$. The emittance of the electron beam in vertical direction is related to the emittance in horizontal direction by the coupling parameter $\varkappa$, i.e., $\varepsilon_v = \varkappa \cdot \varepsilon_h$. The emittance is a constant along the electron orbit.
At the storage ring the so-called β-function, defined for example in horizontal direction by $\beta_h = \sigma_h/\sigma'_h$, can be technically adjusted for the different straight sections. If the undulator is located in a section with low-β-function, i.e., the size of the electron beam is small, this section of the storage ring is referred to as a low-beta section and vice versa. At the ESRF there are alternating sections with low-beta- (odd ID's) and high-beta-function (even ID's).
Typical values for beamlines at the ESRF reported by the machine division are $\sigma_h = 379.0\,\mu\text{m}$, $\sigma_v = 9.1\,\mu\text{m}$, $\sigma'_h = 10.8\,\mu\text{rad}$, $\sigma'_v = 2.6\,\mu\text{rad}$ for a high-beta section, and $\sigma_h = 53.0\,\mu\text{m}$, $\sigma_v = 9.1\,\mu\text{m}$, $\sigma'_h = 105.0\,\mu\text{rad}$, $\sigma'_v = 2.6\,\mu\text{rad}$ for a low-beta section [ESR07]. For the PETRA III-storage ring which is currently under construction a horizontal emittance of 1 nmrad and a coupling of $\varkappa = 1\,\%$ are planned [Bal04].

The most important difference between second and third generation synchrotron radiation sources is the smaller emittance. Additionally, due the higher energy of the

electron beam it is possible to operate undulators in the straight sections of the storage ring with a fundamental wavelength smaller than 1 Å [Mil02].

2.3 X Ray – Matter Interaction

Scattering of x rays from matter is based on the interaction of the electromagnetic field with charged particles. The major contribution to the scattering process is given by electrons of the material. This section provides a summary of the main physical processes of x ray – matter interaction and gives an introduction of wave propagation through a thin slab of material.

2.3.1 Interaction with Free Electron

It is well known from the electrodynamic theory that accelerated charged particles emit electromagnetic radiation with a certain angular distribution. This distribution depends on the direction of the acceleration.
In Fig. 2.4 a schematic drawing is presented. The charge q, located in the origin of the coordinate system, is accelerated along the direction indicated by the vector $\mathbf{a}(t)$.

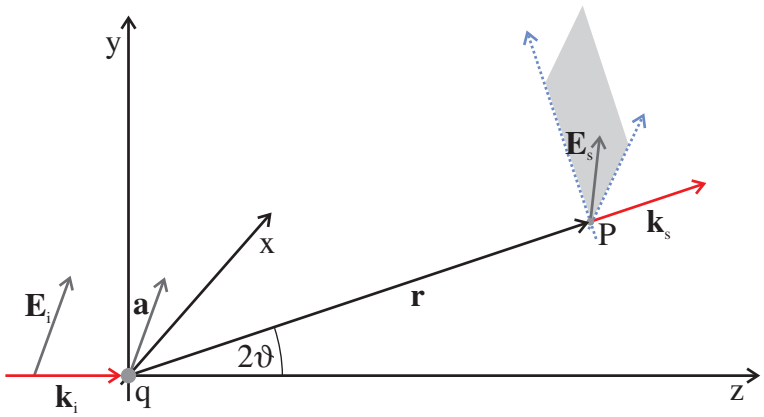

Figure 2.4: Radiation emitted by an accelerated charged particle.

The emitted amplitude $\mathbf{E}_s(\mathbf{r}, t)$ is proportional to the projection of the acceleration into the plane perpendicular to the direction of propagation $\mathbf{r}$. The electric dipole does not emit photons in the direction defined by the acceleration vector $\mathbf{a}$. The amplitude of the emitted wave field is given by [Jac82]

$$\mathbf{E}_s(\mathbf{r}, t) = -\frac{q}{4\pi\varepsilon_0 c^2 r}\left[\mathbf{a}(t') - (\mathbf{a}(t')\cdot\hat{\mathbf{r}})\hat{\mathbf{r}}\right], \tag{2.8}$$

where $\mathbf{E}_s(\mathbf{r}, t)$ is the scattering amplitude, q is the charge, c is the speed of light, $\hat{\mathbf{r}}$ is the unit vector in the direction of observation and $\mathbf{a}(t')$ is the acceleration of the particle evaluated at the retarded time $t' = t - r/c$.

In the special case that the charge is a free electron which is forced by an external electromagnetic field $\mathbf{E}_i(t)$ to perform an oscillating movement the acceleration of the electron is given by $\mathbf{a}(t) = e_0/m_e \cdot \mathbf{E}_i(t)$, where $e_0 = -1.6 \cdot 10^{-19}\,\mathrm{C}$ is the charge and $m_e = 9.1 \cdot 10^{-31}\,\mathrm{kg}$ the rest mass of the electron. Inserting this relation into Eq. (2.8) the scattering amplitude is described by

$$\mathbf{E}_s(\mathbf{r},t) = -\frac{e_0^2}{4\pi\varepsilon_0 m_e c^2 r}\left[\hat{\mathbf{e}}_i - (\hat{\mathbf{e}}_i\cdot\hat{\mathbf{r}})\hat{\mathbf{r}}\right] E_i(t') \tag{2.9}$$

$$= -r_0 \cdot p(\vartheta)\hat{\mathbf{e}}_s \cdot \frac{1}{r} E_i(t'), \tag{2.10}$$

where $p(\vartheta)\hat{\mathbf{e}}_s$ is called polarization factor and $r_0 = e_0^2/(4\pi\varepsilon_0 m_e c^2)$ is denoted the classical electron radius, or the Thomson scattering length. The latter is a measure for the coupling between photons and electrons. The unit-vectors $\hat{\mathbf{e}}_i$ and $\hat{\mathbf{e}}_s$ define the direction of polarization of the incoming and scattered wave field, e.g. $\mathbf{E}_i(t) = E_i(t)\cdot\hat{\mathbf{e}}_i$.

The differential cross-section defined by $d\sigma/d\Omega$ is a measure of the probability that a photon passing through the infinitesimal space area $d\sigma$ is scattered into the solid angle $d\Omega$. It can be deduced from the following expression

$$I_i d\sigma = I_s r^2 d\Omega. \tag{2.11}$$

Eq. (2.11) states the conservation of the number of incoming and outgoing photons. By noting further that the energy flow is related to the time-averaged Poynting-vector $\langle S\rangle$, that is defined by the following relation $\mathbf{S} = \mathbf{E}\times\mathbf{H}$, the intensities related to $\mathbf{E}_i$ and $\mathbf{E}_s$ are given in this case by

$$I = \langle S\rangle = (\varepsilon_0 c/2) E_{\max}^2, \tag{2.12}$$

where I is the intensity and $E_{\max}$ is the maximum amplitude of the electric field. Eq. (2.12) applies to both the incoming and scattered wave field $\mathbf{E}_i$ and $\mathbf{E}_s$.

Inserting Eq. (2.10) into Eq. (2.12) the cross-section of Thomson scattering can finally be obtained from Eq. (2.11)

$$\frac{d\sigma}{d\Omega} = r_0^2 p^2(\vartheta) = r_0^2\left(1 - (\hat{\mathbf{e}}_i\cdot\hat{\mathbf{r}})^2\right). \tag{2.13}$$

In Fig. 2.5 the angular dependence of emitted intensity of an electric dipole oscillating along the x-axis is illustrated. The radiation of the dipole is emitted preferentially perpendicular to the axis of acceleration, i.e., perpendicular to the x-axis in Fig. 2.5. The distribution is rotationally symmetric around this axis.

Since the Thomson cross-section is proportional to the square of the classical electron radius $r_0 = e_0^2/(4\pi\varepsilon_0 m_e c^2) = \alpha^2\cdot a_0 \approx 2.818\cdot 10^{-5}$Å, the interaction between x rays and matter is small. Here, $\alpha = e_0^2/(4\pi\epsilon_0\hbar c) \approx 1/137$ is the fine structure constant and

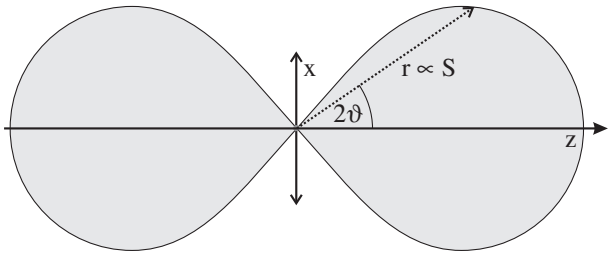

Figure 2.5: Angular intensity distribution for an electric dipole oscillating along the x-axis.

$a_0 = 4\pi\varepsilon_0\hbar^2/(m_e e_0^2) \approx 0.53\,\text{Å}$ is the Bohr radius.
Furthermore, the rest mass of the electron m_e in the denominator of r_0 explains that the main contribution to x-ray scattering is due to electrons. The cross section of x-ray scattering with the lightest charged particle of the atomic nucleus, the proton, is $(m_p/m_e)^2 = 1839^2$ times smaller compared to that of the electron.

Since synchrotron radiation is linearly polarized in the horizontal plane it is worth illustrating the influence of the polarization factor on the scattering scenario in the vertical and horizontal plane (cf. Fig. 2.6).

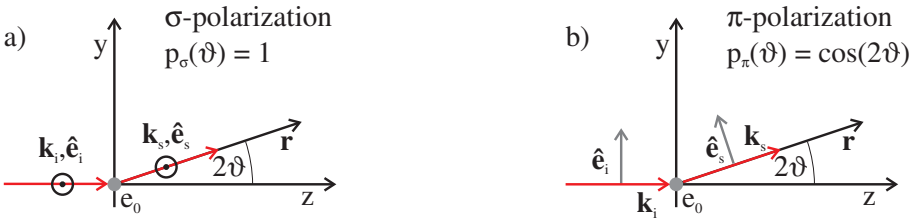

Figure 2.6: a) Polarization of the incident radiation perpendicular and b) parallel to the scattering plane.

If the polarization of the incident electric field is perpendicular to the scattering plane (so-called σ-polarization) the polarization factor $p_\sigma(\vartheta) = 1$ everywhere ($\hat{\mathbf{e}}_i \cdot \mathbf{r} = 0$). An observer positioned in this plane can always observe the full acceleration of the particle. At the synchrotron this scenario describes the scattering into the vertical plane. On the other hand, if the polarization is parallel to the scattering plane (so-called π-polarization) the polarization factor is given by $p_\pi(\vartheta) = \cos(2\vartheta)$. The scattered intensity is proportional to the squared of the polarization factor. The latter is then given by

$$p^2(\vartheta) = \begin{cases} 1 & \sigma\text{-polarization}, \\ \cos^2(2\vartheta) & \pi\text{-polarization}. \end{cases}$$

For an unpolarized source with equal probability of σ- and π-polarization the emitted intensity is given by

$$p^2(\vartheta) = \frac{1}{2} \cdot (1 + \cos^2(2\vartheta)). \tag{2.14}$$

The experiments carried out during this work were performed in small angle x-ray scattering geometry. This means that the maximum scattering angle recorded in our experiments was about $4 \cdot 10^{-3}$ rad. Therefore, the polarization factor is very close to unity for every pixel of the detector and is not considered any more during this work. Nevertheless, it is important to note its significance for crystallography due to the large diffraction angles involved in crystallographic measurements, for coherent diffraction experiments at lower energies, or eventually for high spatial resolution measurements.

2.3.2 Atomic Formfactor

From the quantum mechanical point of view the elastic scattering process on the free electron (cf. Sec. 2.3.1) can be described by absorption and reemission of an x-ray photon with the same energy but a phase shift of π. The interaction is transmitted over the electromagnetic field. In this sense the interpretation of the different terms of Eq. (2.10) is as follows: $-r_0 p(\vartheta)\hat{\mathbf{e}}_s$ is the scattering amplitude defining the coupling that the incoming photon $(\mathbf{k}_i, \hat{\mathbf{e}}_i)$ is scattered into the state $(\mathbf{k}_s, \hat{\mathbf{e}}_s)$ and $1/r \cdot E_i(t - r/c)$ is the amplitude for the propagation of the photon from the origin to $\mathbf{r}$. This picture can easily be extended to the scattering of photons from atoms with a certain number of bound electrons. The distribution of charges is now described by a continuous function $\rho(\mathbf{r})$ that defines the probability that an electron is positioned at a certain position $\mathbf{r}$ of the atom. To the first approximation the binding force, damping terms as well as the influence of the nucleus on the elastic scattering process are neglected.

In the following the probability that a photon is elastically scattered by an atom with electron density $\rho(\mathbf{r})$ into a certain state defined by the scattering vector $\mathbf{k}_s$ will be determined. In Fig. 2.7 a schematic drawing of an atom is shown. From this figure the path length difference introduced by scattering events taking place at different positions $\mathbf{r} = 0$, the origin, and $\mathbf{r} = \mathbf{r}_j$ can be determined. Let $\mathbf{E}_0(t)$ denote the amplitude that a photon is scattered at the origin O. The amplitude for a scattering event at position $\mathbf{r}_j$ is then given by

$$\begin{aligned} \mathbf{E}_j(t) &= \mathbf{E}_0(t) \cdot e^{i\omega(L_j - L_0 + L'_j - L'_0)/c} \\ &= \mathbf{E}_0(t) \cdot e^{-i(\mathbf{k}_s \mathbf{r}_j - \mathbf{k}_i \mathbf{r}_j)} \\ &= \mathbf{E}_0(t) \cdot e^{-i\mathbf{q}\mathbf{r}_j}, \end{aligned} \tag{2.15}$$

where ω is the frequency of the light, and $L_{0,j}$ and $L'_{0,j}$ are the distances between source and scattering point, and between scattering point and observation point respectively. The quantity $\mathbf{q} = \mathbf{k}_s - \mathbf{k}_i$ is called the scattering vector. In Eq. (2.15) it has been assumed that the optical paths are almost parallel, i.e., the distance between source and atom as well as the distance from the atom to the observation point is much larger compared to

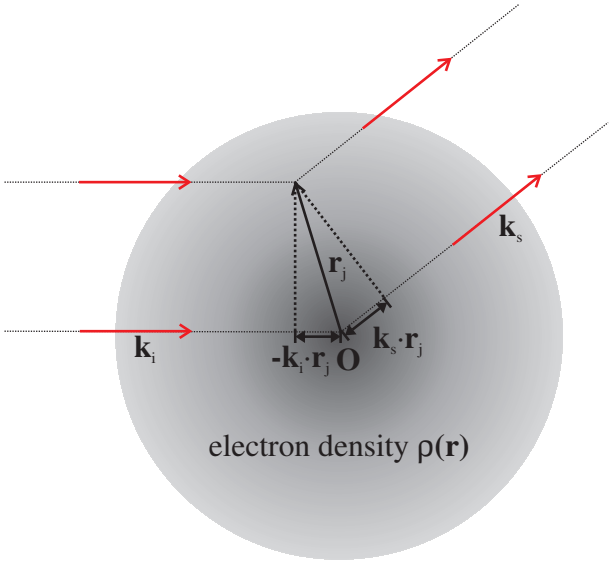

Figure 2.7: Schematic drawing illustrating the path length difference between scattering events at different positions of the atom. In order to calculate the probability that a photon is scattered into the state defined by $\mathbf{k}_s$ all probability amplitudes of possible scattering events have to be summed up.

typical distances of the atom.
The total amplitude is then given by integration of the scattering amplitude over all possible paths:

$$\mathbf{E}(\mathbf{q},t) = \mathbf{E}_0(t)\int_{\text{Atom}} \rho(\mathbf{r})e^{-i\mathbf{qr}}d^3r \tag{2.16}$$

$$= \mathbf{E}_0(t)\cdot f_0(\mathbf{q}). \tag{2.17}$$

The term $f_0(\mathbf{q}) = \int_{\text{Atom}} \rho(\mathbf{r})\exp(-i\mathbf{qr})\,d^3r$ is called the atomic form factor. It is the Fourier-transform of the atomic electron density.

By replacing further the scattering amplitude $E_0(t)$ with the scattering amplitude of a single electron (cf. Eq. (2.10)) it follows that

$$\mathbf{E}(\mathbf{q},t) = E_i(t)(-r_0)p(\vartheta)\hat{\mathbf{e}}_s\cdot f_0(\mathbf{q})\frac{1}{L_0'}e^{-i\omega(t-L_0'/c)}, \tag{2.18}$$

where $E_i(t)$ is the incident amplitude, r_0 is the classical electron radius, $p(\vartheta)$ the polarization factor, and $1/L_0'\cdot\exp(-i\omega(t-L_0'/c))$ is the amplitude for the propagation from the origin to the observation point. This means that the scattering efficiency of an atom is $f_0(\mathbf{q})$ times larger as compared to that of a single electron. In the forward direction all electrons scatter in phase, i.e., $f_0(\mathbf{q}=0)=Z$, where Z is the atomic number.

The picture of the atomic electron density as a continuous medium of free oscillators is a rough approximation. In reality the electrons are bound to the atom and are kept in distinct quantum mechanical states with specified energy. This means that the electrons can not instantly follow the oscillation of the incoming wave field and additional forces such as the binding force and a certain damping factor have to be taken into account. As a result of these additional forces the atomic form factor has two correction terms

$$f(\mathbf{q}) = f_0(\mathbf{q}) + f'(\omega) - if''(\omega). \tag{2.19}$$

In general, $f'(\omega)$ is almost always smaller than zero. It considers the reduced scattering power related to the binding of the electron. This effect is especially strong in the vicinity of resonant frequencies of the electrons. The quantity $f''(\omega)$ is always larger than zero and is related to the absorption of photons. In the next section the connection between these quantities and the phenomenological refractive index n of a material will be described.

2.3.3 Refractive Index

In order to determine the transmission and reflection of x rays on a thin slab of material with thickness Δz the scattering amplitude of all atoms needs to be integrated over the whole plane of material. The schematic drawing presented in Fig. 2.8 illustrates the scattering scenario.

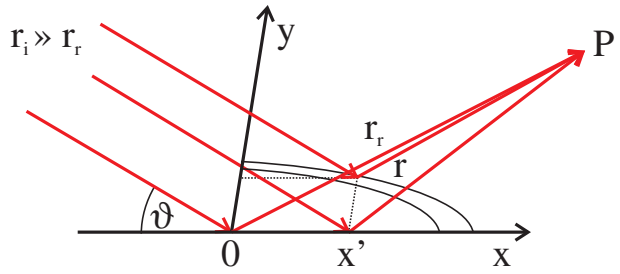

Figure 2.8: Illustration of x-ray scattering from a plane.

In the frame of the first Born-approximation, i.e., single scattering, the scattering contribution of an infinitesimal volume element $dxdy \cdot \Delta z$ is given by

$$d\mathbf{E}_r(t) = E_i(t)(-r_0)p(2\vartheta)f(\mathbf{q}) \cdot \hat{\mathbf{e}}_r \cdot e^{ik_i(x' \cos\vartheta + r - r_r)} \frac{1}{r_r} e^{-i\omega(t - r_r/c)} \cdot n_{EZ}\Delta z \cdot dxdy, \tag{2.20}$$

where n_{EZ} is the atomic density, r_r is the distance from the origin to the observation point, r is the distance between the volume element and the observation point, ϑ is the angle of incidence and $p(2\vartheta)$ is the polarization factor. The term $\exp(ik_i(x' \cos\vartheta) + r - r_r)$ considers the phase shift of the scattering amplitude related to the propagation over the

origin and the surface element $dxdy$. The integration of Eq. (2.20) over the xy-plane yields the reflected amplitude $\mathbf{E}_r(t)$:

$$\mathbf{E}_r(t) = E_i(t)(-r_0)p(\vartheta)f(\mathbf{q})\cdot\hat{\mathbf{e}}_r\cdot i\frac{\lambda r_r n_{EZ}\Delta z}{\sin\vartheta}\frac{1}{r_r}e^{-i\omega(t-r_r/c)}. \tag{2.21}$$

The transmitted amplitude can easily be found from Eq. (2.21) by assuming the forward scattering geometry, i.e., f($\mathbf{q}=0$), and taking into account the superposition with the undisturbed incoming wave field:

$$\mathbf{E}_t(t) = \left(\hat{\mathbf{e}}_i - r_0 f(0)\hat{\mathbf{e}}_t\cdot i\frac{\lambda r_t n_{EZ}\Delta z}{\sin\vartheta}\right)\frac{E_i}{r_t}e^{-i\omega(t-r_t/c)}. \tag{2.22}$$

Phenomenologically, reflection and absorption of x rays can be described by the complex refractive index n. This is due to the fact, that the macroscopic result looks as if a certain part of the incoming wave is reflected on the surface and another part permeate the material under a certain angle of refraction. However, from the microscopic perception all atoms contribute independently to absorption and refraction.

In a next step the macroscopic description of wave propagation through a thin slab of material is considered. The incoming wave may be described by the electric field amplitude $E_i(t) = E_q\cdot\exp\left(-i\omega(t-r/c)\right)$ incident on the thin slab of material with thickness Δz.

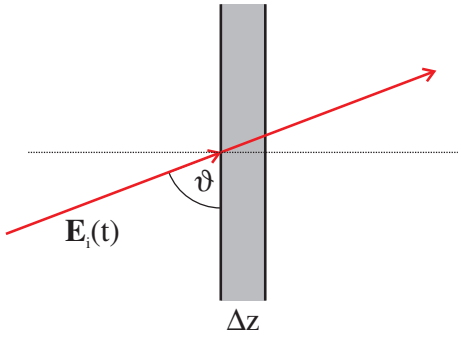

Figure 2.9: Wave transmission through a thin slab of material.

Due to the interaction with the material the phase velocity of the wave is different from that in vacuum, i.e., $v = c/n$, and a certain phase retardation relative to the undisturbed propagation is accumulated on the optical path through the slab. It is related to the thickness of the material and the angle of incidence:

$$\begin{aligned}\Delta t &= \frac{\Delta z/\sin\vartheta}{c/n} - \frac{\Delta z/\sin\vartheta}{c} \\ &= (n-1)\frac{\Delta z}{c\cdot\sin\vartheta}.\end{aligned} \tag{2.23}$$

This means that the wave field after a thin slab of material is described by

$$\begin{aligned} E_t(t) &= E_i(t) e^{i\omega(n-1)\frac{\Delta z}{c \sin\vartheta}} \\ &\approx E_i(t)\left(1 + i\omega(n-1)\frac{\Delta z}{c\cdot \sin\vartheta}\right), \end{aligned} \tag{2.24}$$

where $E_i(t)$ defines the unperturbed wave field. The applied approximation is valid in case of x rays if the induced phase shift is small. The comparison between Eq. (2.22) and Eq. (2.24) establishes the connection between the macroscopic refractive index and microscopic properties of the material such as the atomic density n_{EZ} and the atomic form factor $f(\mathbf{q}=0)$:

$$\begin{aligned} n &= 1 - \frac{1}{2\pi} r_0 \lambda^2 n_{EZ} f(\mathbf{q}=0) \\ &= 1 - \frac{N_a}{2\pi} r_0 \lambda^2 \frac{\rho}{A} f(\mathbf{q}=0), \end{aligned} \tag{2.25}$$

where N_a is the Avogadro-constant, A is the atomic weight, ρ is the density and $n_{EZ} = \rho/A \cdot N_a$ is the atomic density.
By replacing further the atomic form factor using Eq. (2.19) the refractive index is given by

$$n = 1 - \frac{N_a}{2\pi} r_0 \lambda^2 \frac{\rho}{A}(Z + f') + i\frac{N_a}{2\pi} r_0 \lambda^2 \frac{\rho}{A} f'' \tag{2.26}$$

$$= 1 - \delta + i\beta. \tag{2.27}$$

For hard x rays the real part of the refractive index is very close to 1 and is defined by the parameter $\delta \approx 10^{-6}$. The absorption of x rays is related to the parameter β. The comparison between Eq. (2.26) and Eq. (2.27) yields

$$\delta = \frac{N_a}{2\pi} r_0 \lambda^2 \frac{\rho}{A}(Z + f'), \tag{2.28}$$

$$\beta = \frac{N_a}{2\pi} r_0 \lambda^2 \frac{\rho}{A} f''. \tag{2.29}$$

Using these parameters of δ and β the wave field after the slab given by Eq. (2.24) can be written in the following way

$$E_t(t) = E_i(t) \cdot e^{-ik\delta\frac{\Delta z}{\sin\vartheta}} \cdot e^{-k\beta\frac{\Delta z}{\sin\vartheta}}, \tag{2.30}$$

where $k = \omega/c$ is the wave number. The law of Lambert-Beer states that the transmitted intensity ($I \propto E_t^2$) is given by $I_t = I_i \cdot \exp(-\mu d)$, where μ is the linear absorption coefficient and d is the projected thickness of the material, in this case, $d = \Delta z/\sin\vartheta$. The comparison of parameters yields the following relationship between β and μ:

$$\beta = \frac{\mu}{2k}. \tag{2.31}$$

The phase shift introduced by propagation of the wave field through the material is given by

$$\Delta\phi(x,y) = -k\delta d(x,y), \tag{2.32}$$

where $d(x,y)$ defines the projected thickness of the material along the optical path at a certain position (x,y) in the plane perpendicular to the direction of propagation. In case that the material is inhomogeneous it is necessary to carry out the following integration:

$$\Delta\phi(x,y) = -k\int_{z_1}^{z_2}\delta(x,y,z)dz. \tag{2.33}$$

For example, the phase shift accumulated by propagation of x rays with energy of 8 keV through a thin Au-layer with a thickness of $d = 150\,\text{nm}$ is given by $\Delta\phi = -0.29\,\text{rad}$, where $\lambda(E = 8\,\text{keV}) = 1.55\,\text{Å}$ and $\delta_{\text{Au}}(8\,\text{keV}) = 4.7\cdot10^{-5}$ were used.

In numerical simulations presented in this work the material dependent parameters like f', f'', μ, or ρ were obtained from a database [Cha95].

For reasons of completeness the inelastic scattering process, also known as Compton-scattering, is mentioned here. It considers the scattering scenario that a certain amount of energy may be transferred to kinetic energy of the electron, i.e., the energy of the scattered photon is smaller compared to the incident photon energy. As a result of the law of conservation of energy and momentum the possible energy transfer is related to the scattering angle ϑ. The shift in wavelength $\Delta\lambda$ is given by

$$\Delta\lambda = \lambda_c(1-\cos\vartheta), \tag{2.34}$$

where $\lambda_c = h/(m_e c) \approx 2.43\cdot10^{-12}\,\text{m}$ is denoted as Compton wavelength.
The differential cross section for Compton-scattering can be deduced from the relativistic quantum mechanical Klein-Nishina-formula [Kle29]. For photon energies smaller than 100 keV and unpolarized light it is given by [Gün03]

$$\left(\frac{d\sigma}{d\Omega}\right)_{KN} \approx \frac{r_0^2(1+\cos^2\vartheta)}{2[1+l(1-\cos\vartheta)]^2}, \tag{2.35}$$

where r_0 is the classical electron radius, $l = E/m_e c^2$ and E is energy of the photon. For small photon energies the cross section approaches the Thomson scattering cross section. Integration over the solid angle yields

$$\sigma_{KN} = 8\pi r_0^2\cdot\frac{1+2l+1.2l^2}{3(1+2l)^2}. \tag{2.36}$$

Since the interaction with the electron is taking place at a certain position of the sample which, in principle, can be experimentally identified, inelastic scattering with x rays is

an incoherent process. Therefore, scattering events at different positions of the sample are distinguishable from each other and as a result, the scattering amplitudes have to be summed incoherently. Interference effects related to inelastic x-ray scattering are not observable. Nevertheless, Compton-scattering can contribute to a certain background signal which becomes especially important at higher photon energies.

2.4 Wave Propagation in Free Space

The understanding of free-space propagation of an x-ray wave field from the sample to the detector is important for the CXDI-method. An outline of the theoretical description of wave propagation based on the Maxwell-equations is given in this section.
However, in practice the goal is to solve the inverse problem, i.e., we are looking for the exit wave field after the sample knowing the measured intensity of the electromagnetic field at some distance in the far-field downstream (Fraunhofer-regime).

It is well known from electrodynamics that the evolution of a wave field in free-space obeys the differential wave equation

$$\left(\frac{1}{c^2}\frac{\partial^2}{\partial t^2} + \Delta\right)\mathbf{E}(\mathbf{r},t) = 0, \tag{2.37}$$

where $\mathbf{E} = (E_x, E_y, E_z)$ is the electromagnetic wave vector. It can be shown that in free-space the electromagnetic wave field can be described by a scalar complex field [Bor99]. This is mainly due to the fact that each of the components of the electric field vector $\mathbf{E}(\mathbf{r},t)$, namely E_x, E_y and E_z, have to fulfill the same differential equation. The same is valid for the components of the magnetic field $\mathbf{B}(\mathbf{r},t)$. Therefore, in the following only one component of the field vector, say $E(\mathbf{r},t) = E_x(\mathbf{r},t)$, is considered for the description of the electric field. This implies that polarization effects are not considered here.

The time dependence of $E(\mathbf{r},t)$ can be separated using the method of spectral decomposition. This leads to the introduction of the Fourier transform in time and frequency domain:

$$E(\mathbf{r},t) = \frac{1}{\sqrt{2\pi}}\int_0^\infty E_\omega(\mathbf{r})e^{-i\omega t}d\omega. \tag{2.38}$$

The subscript ω denotes that the quantity depends on the frequency. By substituting Eq. (2.38) into Eq. (2.37) it can be shown that the amplitude $E_\omega(\mathbf{r})$ has to be a solution of the time-independent Helmholtz-equation:

$$\left(\Delta + k^2\right)E_\omega(\mathbf{r}) = 0, \tag{2.39}$$

where $k = \omega/c$ is the wave number.

In the following, the aim is to determine the wave field $E(x,y,z_2)$ in a plane defined by z_2 knowing its distribution $E(x,y,z_1)$ at z_1. In Fig. 2.10 a schematic drawing of wave

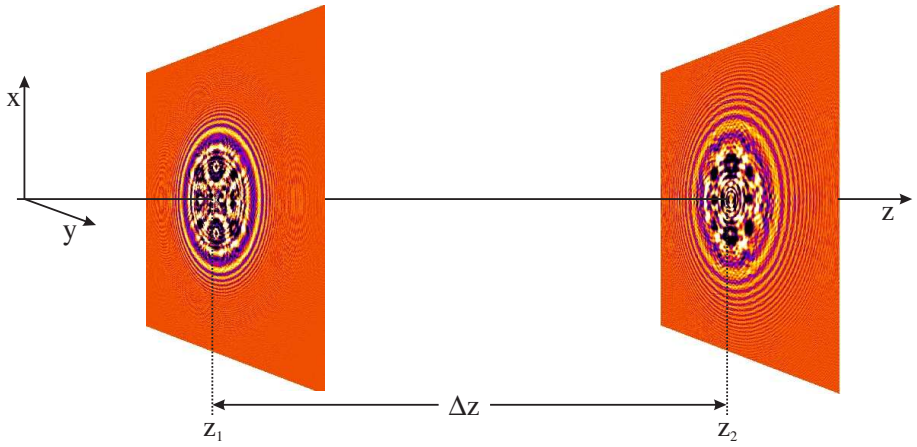

Figure 2.10: Free-space propagation of a wave field in paraxial approximation from one plane defined by z_1 to another plane at position z_2.

propagation in free space is presented.

The elementary solution of the Helmholtz-equation (2.39) is given by plane waves $E_\omega = E_A \cdot \exp(i(k_x x + k_y y + k_z z))$, where $k^2 = k_x^2 + k_y^2 + k_z^2$ and E_A is a constant amplitude. In case that $k^2 > k_x^2 + k_y^2$ the solution is called a propagating wave. Otherwise, it is denoted as an evanescent wave.
That is, the propagation of the plane wave from one plane at $z = z_1$ to another at $z = z_2$ can be described by

$$E_\omega(x, y, z_2) = E_\omega(x, y, z_1) \cdot e^{i\Delta z\sqrt{k^2 - k_x^2 - k_y^2}}, \tag{2.40}$$

where k_z was replaced by $\sqrt{k^2 - k_x^2 - k_y^2}$ and $\Delta z = z_2 - z_1$.
The general method to propagate an arbitrary wave field $E_\omega(x, y, z_1)$ to a plane $z = z_2$ is obtained by 2D-Fourier-decomposition of the wave field into its plane wave components, followed by the multiplication with the propagator factor $\exp\left(i\Delta z\sqrt{k^2 - k_x^2 - k_y^2}\right)$ of Eq. (2.40) and finally the summation over all plane wave components. The first step, the decomposition of the wave field, is done using the two-dimensional Fourier-transform:

$$E_\omega(x, y, z_1) = \frac{1}{2\pi} \iint \tilde{E}_\omega(k_x, k_y, z_1) e^{i(k_x x + k_y y)} dx dy. \tag{2.41}$$

For each of these plane wave components $\tilde{E}_\omega(k_x, k_y, z_1)$ the propagation to the plane defined by $z = z_2$ is just implemented by multiplication with the so-called free-space propagator. Altogether, the general solution is obtained by summation over all plane wave components. This yields

$$E_\omega(x, y, z_2) = \frac{1}{2\pi} \iint \tilde{E}_\omega(k_x, k_y, z_1) \cdot e^{i\Delta z\sqrt{k^2 - k_x^2 - k_y^2}} \cdot e^{i(k_x x + k_y y)} dk_x dk_y. \tag{2.42}$$

A shorter notation for the propagation of a wave field from plane z_1 to plane z_2 is:

$$E_\omega(x,y,z_2) = \mathscr{F}^{-1}\left[e^{i\Delta z\sqrt{k^2-k_x^2-k_y^2}}\mathscr{F}\left[E_\omega(x,y,z_1)\right]\right]. \tag{2.43}$$

where $\mathscr{F}$ denotes the 2D-Fourier transform.

2.4.1 Fresnel Diffraction

In the paraxial approximation, i.e., when the angle between the **k**-vector and a certain main direction of propagation, say **z**, is small ($k_x^2 + k_y^2 \ll k^2$), the exponent of the propagator can be approximated using the Taylor-expansion, i.e.,

$$\Delta z\sqrt{k^2-k_x^2-k_y^2} \approx k\Delta z\left(1-\frac{k_x^2+k_y^2}{2k^2}\right). \tag{2.44}$$

Using this approximation in Eq. (2.43) gives for the wave field at distance $z = z_2$

$$E_\omega(x,y,z_2) = e^{ik\Delta z}\mathscr{F}^{-1}\left[e^{-\frac{i\Delta z(k_x^2+k_y^2)}{2k}}\mathscr{F}\left[E_\omega(x,y,z_1)\right]\right]. \tag{2.45}$$

The factor $\exp\left(-\frac{i\Delta z(k_x^2+k_y^2)}{2k}\right)$ is called the kernel of the Fresnel propagator.
Eq. (2.45) can be represented in another form using the convolution theorem $\mathscr{F}[f(x,y)\otimes g(x,y)] = 2\pi\mathscr{F}[f(x,y)]\cdot\mathscr{F}[f(x,y)]$, where '$\otimes$' denotes the convolution operation

$$f(x,y)\otimes g(x,y) = \iint_{-\infty}^{\infty} f(x',y')g(x-x',y-y')dx'dy'. \tag{2.46}$$

Applying the convolution theorem to Eq. (2.45) and using the following relation

$$\exp\left(\frac{-i\Delta z\left(k_x^2+k_y^2\right)}{2k}\right) = \mathscr{F}\left\{-\frac{ik}{\Delta z}\exp\left(\frac{ik\left(x^2+y^2\right)}{2\Delta z}\right)\right\}, \tag{2.47}$$

the Fresnel diffraction integral can be deduced:

$$E_\omega(x,y,z_2) = -\frac{ik}{2\pi\Delta z}e^{ik\Delta z}\iint_{-\infty}^{\infty} E_\omega(x',y',z_1)\exp\left\{\frac{ik}{2\Delta z}\left((x-x')^2+(y-y')^2\right)\right\}dx'dy'. \tag{2.48}$$

In the paraxial approximation the propagation of a complex two-dimensional wave-field from one plane at $z = z_1$ to another plane at $z = z_2$ can be implemented numerically in two different ways. The convolutional approach is based on Eq. (2.45). It involves three steps:

1. Take the Fourier-transform of the wave field at position $z = z_1$ in order to get $\tilde{E}_\omega(k_x,k_y,z_1)$.
2. Multiply the result with the phase factor $\exp\left(-\frac{i}{2k}(k_x^2+k_y^2)\Delta z\right)$.

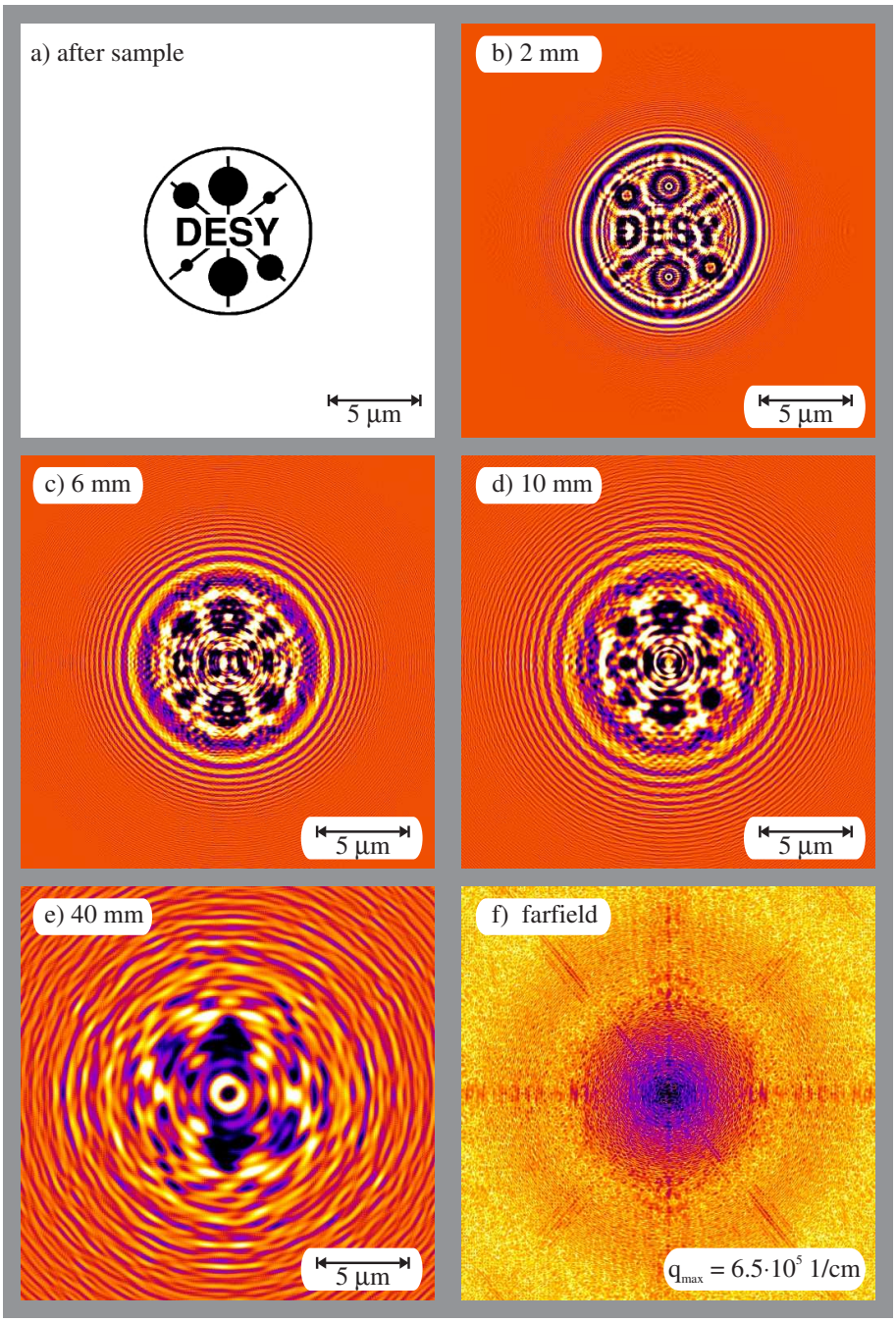

Figure 2.11: Intensity distribution of a wave field produced by a two-dimensional Au-sample with a size of 10 µm and a thickness of 150 nm for different propagation distances and a photon energy of 8 keV. The propagation distance is indicated in each image. The Fresnel-regime extends to propagation distances of around 65 cm ($N_F = 1$). In Fig. f) the far-field diffraction pattern is shown.

3. Take the inverse Fourier-transform and multiply with the phase factor $\exp(ik\Delta z)$ to get the field distribution at $z_2 = z_1 + \Delta z$.

Since the propagation distance Δz appears in the numerator of the phase factor this approach is especially accurate in numerical calculations for small propagation distances. In the limit $\Delta z \to 0$ the intensity distribution remains unchanged, as expected.

Another approach is based on the direct application of the Fresnel diffraction integral. By expansion of the quadratic terms Eq. (2.48) can be represented in the following form

$$E_\omega(x,y,z_2) = -\frac{ik}{2\pi\Delta z} e^{ik\Delta z} P_{\Delta z}(x,y) \iint_{-\infty}^{\infty} \{E_\omega(x',y',z_1)\cdot P_{\Delta z}(x',y')\}\, e^{-\frac{ik}{\Delta z}(xx'+yy')} dx'dy', \tag{2.49}$$

where $P_{\Delta z}(x,y) = \exp\left(\frac{ik}{2\Delta z}(x^2+y^2)\right)$ is a phase factor in real space. The numerical calculation requires also three operations:

1. Multiply the initial field distribution with the phase factor $P_{\Delta z}(x',y')$.
2. Calculate the Fourier-transform with respect to x' and y'.
3. Multiply the result with the phase factor $P_{\Delta z}(x,y)$ and take into account the prefactor of Eq. (2.49).

Since Δz appears in the denominator of the phase factor $P_{\Delta z}$ the latter method is especially suitable in calculations of large propagation distances $\Delta z \gtrsim k/2 \cdot D^2$, where D is a characteristic distance in the initial plane z_1. In this case the propagator is a slowly varying function.
If the propagation distance is even larger the phase factor inside the integral approaches one and can be left out. In this case Eq. (2.49) gives an expression for Fraunhofer-diffraction. The intensity of the wave field after propagation is then fully determined by the Fourier-transform of the initial field distribution $E_\omega(x,y,z_1)$:

$$E_\omega(x,y,z_2) = -\frac{ik}{2\pi\Delta z} e^{ik\Delta z} \iint_{-\infty}^{\infty} E_\omega(x',y',z_1) e^{-\frac{ik}{\Delta z}(xx'+yy')} dx'dy'. \tag{2.50}$$

The Fraunhofer approximation is fulfilled if the Fresnel number $N_F \ll 1$. It is defined as

$$N_F = \frac{D^2}{\lambda\Delta z}. \tag{2.51}$$

Notice further that, due to the single application of the Fourier-transform, the assumed pixel size of a discrete, two-dimensional field changes when using this method of propagation. The pixel size after the propagation can be calculated by using the general relation valid for the discrete Fast-Fourier-Transformation (FFT):

$$\Delta x \Delta q_x = 2\pi/N, \tag{2.52}$$

where Δx and Δq_x define a resolution element in real and reciprocal space, respectively. N is the total number of pixels. The minimum distance in reciprocal space Δq_x needs to be identified with the pixel size after propagation $\Delta x_{\Delta z}$. It is physically related to the wavelength λ of the radiation by $\Delta q_x = 2\pi/\lambda \cdot (\Delta x_{\Delta z}/\Delta z)$. The insertion of this equation into Eq. (2.52) yields

$$\Delta x_{\Delta z} = \frac{\Delta z \cdot \lambda}{N \cdot \Delta x}. \tag{2.53}$$

The pixel size after propagation is directly proportional to the propagation distance Δz and the wavelength λ. Obviously, Eq. (2.53) is valid for the x- and y-coordinate.
The convolutional approach on the other hand does not change the pixel size used in the simulation since it involves the forward and inverse Fourier transform.

2.5 Sampling of the Diffraction Pattern

The far-field diffraction pattern of the sample is related by the Fourier-transform to the exit wave field after the sample (cf. Eq. 2.50). Experimentally, it is impossible to measure the continuous diffraction pattern, but instead, the intensity is integrated over small distinct areas of reciprocal space. The distance between these discrete points determines how well the diffraction pattern is sampled which depends on the pixel size p and the distance from the sample to the detector L. Whether this is sufficient to resolve the diffraction pattern is defined by the lateral size of the sample D, and the wavelength λ. In the case that the object has a finite size D, the smallest distance in reciprocal space corresponding to this size is given by $\Delta q = 2\pi/D$. The minimum distance of the fringes on the detector is then given by $\Delta x_s \approx \Delta q/k \cdot L = \lambda L/D$, where L is the distance between sample and detector and $k = |\mathbf{k}|$ is the wave number of the incident radiation.

As illustrated in Fig. 2.12(a) the recording of intensity variations of the diffraction pattern would be impossible if the pixel size of the detector is equal or larger than Δx_s. However in principle, according to the Shannon-theorem, this sampling distance would be fine enough to recover the continuous spatial variation of the finite bandwidth signal measured with its phase. Since in this case only the amplitude of the field is measurable, the effective period of the intensity variations in reciprocal space appears shortened. In Fig. 2.13 an illustration is given for the 1-dimensional case. For this reason the maximum sampling distance in reciprocal space is given by $\Delta q \leq \pi/D$ (cf. Fig. 2.12(b)). This means, in order to accurately sample the diffraction pattern of a finite sample of size D, the pixel size p of the detector must be at least smaller than half the speckle size, i.e.,

$$p \leq \frac{\lambda L}{2D}. \tag{2.54}$$

A different way to justify the oversampling is given by looking at the number of unknowns in real space that have to be determined from the diffraction pattern. From this point

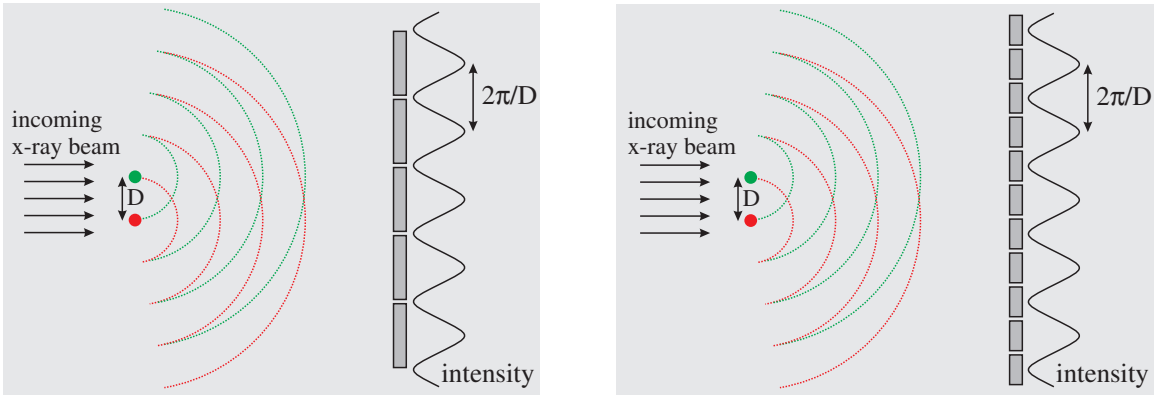

(a) Pixel size as large as a the speckle size. **(b)** 2-fold oversampling

Figure 2.12: Due to the finite size of the specimen the signal in reciprocal space is band-limited, i.e., the minimum distance between minima or maxima of intensity is defined by $\Delta q = 2\pi/D$. In order to resolve the diffraction fringes the area of reciprocal space covered by a single pixel has to be smaller than π/D. This case is named by 2-fold oversampling.

of view, the phase retrieval method is considered as a mathematical problem to solve a set of non-linear equations related by the Fourier transform. This approach is also applicable for problems in more than one or two dimensions. For illustration the discrete 2D-Fourier-transform may be introduced:

$$G(q_x, q_y) = \sum_{n_x=0}^{N_x-1} \sum_{n_y=0}^{N_y-1} g(x, y) e^{-i(q_x n_x/N_x + q_y n_y/N_y)}, \tag{2.55}$$

where $g(x, y)$ is the two dimensional complex real-space function and $G(q_x, q_y)$ its 2D-discrete Fourier-pair. Eq. (2.55) reveals the defined relationship between the complex quantities of $g(x, y)$ and $G(q_x, q_y)$. However, in the case that the object occupies the whole area of $N_x \cdot N_y$ pixels on a two-dimensional grid the number of knowns in reciprocal space is by a factor of two too few since only the intensity is measurable but not the phase. This means that in order to have the same number of unknowns and knowns in real and reciprocal space it is necessary to sample the diffraction pattern on a finer scale. In this case the system is over-determined by a certain factor.

This so-called oversampling is related to the creation of a no-density region surrounding the object. As already mentioned, in case of a twofold oversampling the number of unknowns in real space is identical to the number of measured diffraction intensities at the detector position. This over-determination is the basis for a successful reconstruction of the object. The oversampling ratio σ can be defined as [Mia00b]

$$\sigma = \frac{\text{total region}}{\text{electron density region}}, \tag{2.56}$$

where the total region includes the empty area around the object.

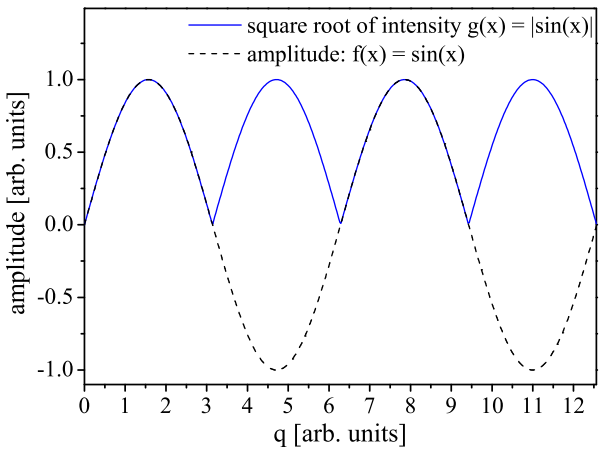

Figure 2.13: Comparison between the spatial variation of the amplitude and the measurable quantity of the magnitude of the electromagnetic field.

If the diffraction pattern is sampled on a finer grid then the empty region surrounding the object is further enlarged as it is illustrated in Fig. 2.14 on simulated data. In Fig. 2.14(a) the size of a detector pixel is small enough that the fringes of the diffraction pattern are sampled by approximately eight pixels in each dimension. The inset shows the corresponding real space object. Imagine now that you would have measured the same diffraction pattern with a detector whose pixel size is four times larger in each dimension then you would get the result shown in Fig. 2.14(b). The oversampling criteria is still fulfilled in this case. However, the size of the 2D-matrix is by a factor of 16 smaller compared to the previous situation. Its real-space analog is given in the inset. Due to the fact that the largest diffraction angle is the same for both diffraction patterns they provide theoretically the same resolution in real space. Though, in the case of the 8-fold oversampling the size of the array in real space is 16 times larger. This additional space around the object is filled with zeros.

The measurement of intensity values on a discrete grid causes also a discrete sampling in real space. In the following the relationship between sampling distance in real- and reciprocal space will be given.
The pixel size of the detector p in combination with the wavelength λ and the distance L between sample and detector determines the sampling distance Δq in reciprocal space (cf. Fig. 2.15):

$$\begin{aligned} \Delta q &= 2|k| \cdot \sin\vartheta \\ &\approx |k| \cdot \frac{p}{L}. \end{aligned} \tag{2.57}$$

The distance L is assumed to be large enough that the approximation in Eq. (2.57) is valid.

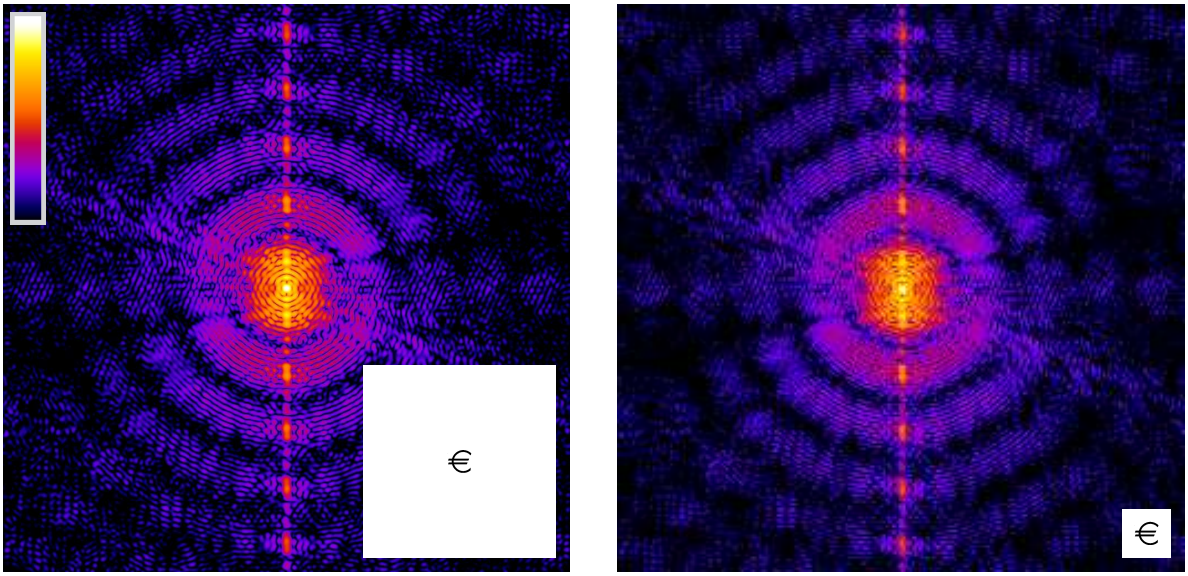

(a) 8-fold oversampling **(b)** 2-fold oversampling

Figure 2.14: Illustration of the empty region around the object due to oversampling of the diffraction pattern. The diffraction pattern in (a) is 8-fold oversampled in each dimension whereas in (b) the oversampling ratio is only 2, i.e., 4×4 pixels of pattern (a) were binned to define one pixel in pattern (b) and, therefore, the size of the array in (b) is 16 times smaller than in pattern (a). The insets show the corresponding images of the object for each diffraction pattern. Since the effective pixel size in real space is related to the maximum diffraction angle recorded the lateral resolution is the same in both images. The fire-color table is used throughout this work for illustration of the diffraction patterns in logarithmic intensity scale. It is indicated in Fig. a).

By using further the general property of the Fourier-transform for a discrete data set with number of variables N, $\Delta x \cdot \Delta q = 2\pi/N$, the corresponding sampling distance in real space Δx is given by

$$\begin{aligned} \Delta x &= \frac{2\pi}{Nk} \cdot \frac{L}{p} \\ &= \frac{\lambda L}{Np}. \end{aligned} \tag{2.58}$$

Eq. (2.58) applies to both the x- and y-dimension.

As a remark, the sampling situation presented in Fig. 2.12(a) is well known from crystallography, where the intensity of the scattered photons is measured at discrete points in reciprocal space (Nyquist-Sampling). These so-called Bragg-peaks lie on a lattice in reciprocal space and the distance between them is determined by the size of the unit cell. For that reason the crystallographic phase problem is twice undetermined and it is not easily possible to derive the crystal structure from the intensity of the

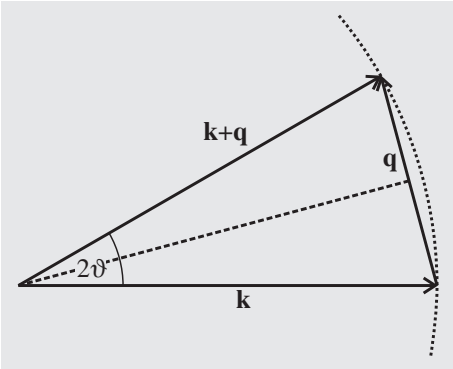

Figure 2.15: Scattering vector for elastic scattering.

Bragg-peaks alone without introduction of additional information. An overview of phase retrieval in crystallography and optics is given by R. Millane in [Mil90].

2.6 Partial Coherence

The emission of x-ray synchrotron radiation is a random process and the emission of photons is uncorrelated. Nevertheless, depending on the geometry of the experiment and the spectrum of the radiation, it is possible to observe interference effects related to the partial coherence of the light. In Fig. 2.16 a simple schematic drawing illustrating longitudinal and transverse coherence is shown [AN01].

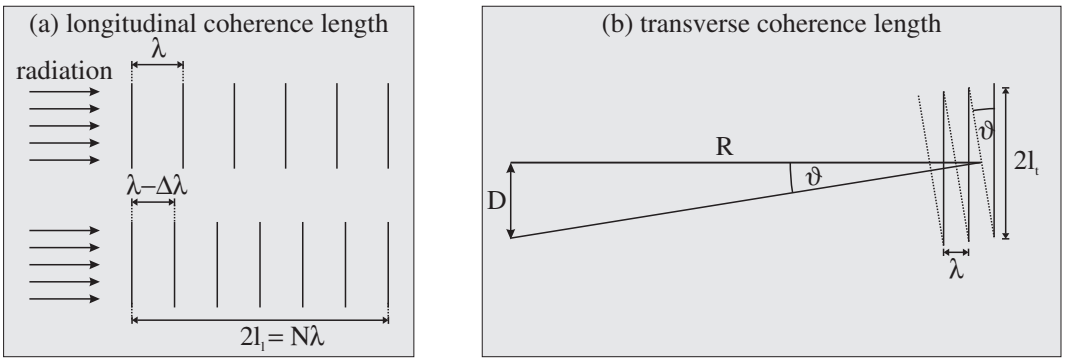

Figure 2.16: Schematic drawing illustrating the longitudinal and transverse coherence properties of light. Although the emission of photons is an incoherent process at x-ray sources, interference effects can be observed due to the large propagation distance from the source to the sample position. (a) The longitudinal coherence length is related to the monochromaticity of the radiation. (b) The lateral coherence length is defined by the source size, the distance from the source to the sample as well as the wavelength.

The longitudinal, or temporal, coherence is related to the monochromaticity of light. Imagine to have two different components of the wave field with wavelengths λ and

$\lambda - \Delta\lambda$ propagating in the same direction then after a certain propagation distance of $l_l \approx \lambda/2 \cdot (\Delta\lambda/\lambda)^{-1}$ these wave field components will be out of phase. This distance is named the longitudinal coherence length of the light (cf. Fig. 2.16 (a)).
Furthermore, the spatial separation of distinct points of an extended source produces a difference in path length at a certain observation point. In Fig. 2.16 (b) a schematic drawing illustrating the path length difference due to an extension of the source D is shown. The larger is the source the smaller is the distance l_t between two points in the observation plane where these wave amplitudes are out of phase (cf. Fig. 2.16 (b)). Therefore, the transverse coherence length is related to the inverse of the solid angle under which the source is seen by the observer, i.e., $l_t \approx \lambda/2 \cdot (D/R)^{-1}$.
The diffraction pattern of a quasi-monochromatic extended source is just the sum over all diffraction patterns that would have been created by a single point inside the source individually. Due to the relative displacement of these diffraction patterns the final diffraction pattern is smeared and the interference fringes disappear if the offset between these individual diffraction patterns is larger than given by the Rayleigh-criterion, i.e., the main maximum of one diffraction pattern is overlapping the first minimum of a second one.

A more detailed theoretical description is based on the formulation of a correlation function, the so-called mutual coherence function $\Gamma_{12}(\tau)$. It expresses the correlation of the wave field between point P_1 and P_2 at a certain time delay τ. The general expression for the mutual coherence function is given by [Bor99]

$$\Gamma_{12}(\tau) = \langle E_1(t+\tau) \cdot E_2^*(t) \rangle, \tag{2.59}$$

where $E_1(t)$ and $E_2(t)$ define the wave field at P_1 and P_2, the function $\Gamma_{12}(\tau)$ refers to the correlation between the points P_1 and P_2, and $\langle \dots \rangle$ denotes time averaging over many cycles.

The quantity of mutual coherence becomes important in the calculation of the wave-field in plane B (Fig. 2.17) after an opaque screen with two pinholes P_1 and P_2 positioned in the plane A. The interference pattern observed in the plane B depends on the properties of the wave fields emanating from P_1 and P_2, as well as the path length differences s_1 and s_2. In Fig. 2.17 an illustration of the geometrical arrangement is shown [Bor99]. The observed intensity distribution in plane B is directly related to the mutual coherence function in plane A and can be calculated according to

$$I(Q) = I^{(1)}(Q) + I^{(2)}(Q) + 2\sqrt{I^{(1)}(Q)}\sqrt{I^{(2)}(Q)} \cdot \gamma_{12}^{(r)} \left(\frac{s_2 - s_1}{c} \right), \text{ with} \tag{2.60}$$

$$\gamma_{12}(\tau) = \frac{\Gamma_{12}(\tau)}{\sqrt{\Gamma_{11}(0)}\sqrt{\Gamma_{22}(0)}} = \frac{\Gamma_{12}(\tau)}{\sqrt{I_1}\sqrt{I_2}}. \tag{2.61}$$

The function $\gamma_{12}(\tau)$ is called the complex degree of coherence. The superscript (r) denotes the real part of the function. It is the normalized function of the mutual coherence

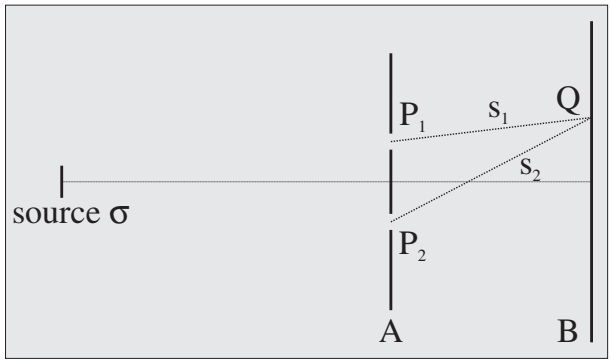

Figure 2.17: Mutual coherence is defined by the correlation of the wave field at two arbitrary points P_1 and P_2 in plane A. The intensity distribution in plane B is defined by the wave fields emanating from P_1 and P_2 to the point Q.

and can assume values between 0 and 1. The variables $I^{(1)}(Q)$ and $I^{(2)}(Q)$ define the intensities at point Q that would have been observed if only pinhole P_1, or respectively pinhole P_2, are opened. Intensities I_1 and I_2 are absolute values measured at P_1 or P_2. By rearranging Eq. (2.60) it can be deduced that the mutual coherence function is a measurable quantity:

$$\gamma_{12}^{(r)}\left(\frac{s_2 - s_1}{c}\right) = \frac{I(Q) - I^{(1)}(Q) - I^{(2)}(Q)}{2\sqrt{I^{(1)}(Q)}\sqrt{I^{(2)}(Q)}}. \tag{2.62}$$

In case of quasi-monochromatic light the complex degree of coherence is related to the visibility $V(Q)$ of interference fringes:

$$\begin{aligned} V(Q) &= \frac{I_{\max} - I_{\min}}{I_{\max} + I_{\min}} && (2.63)\\ &= \frac{2\sqrt{I^{(1)}(Q)}\sqrt{I^{(2)}(Q)}}{I^{(1)}(Q) + I^{(2)}(Q)}\,|\gamma_{12}(\tau)| && (2.64)\\ &= |\gamma_{12}(\tau)|\ , \quad \text{if } I^{(1)}(Q) = I^{(2)}(Q). && (2.65) \end{aligned}$$

In addition, if the time τ is much smaller than the coherence time of the light the mutual coherence function can be approximated by $J_{12} := \Gamma_{12}(0) = \langle E_1(t) \cdot E_2^*(t)\rangle$, the so-called mutual intensity function. The degree of spatial coherence is defined in this case by $j_{12} = J_{12}/\left(\sqrt{I_1}\sqrt{I_2}\right)$.

One of the most important relations in the theory of partial coherence is the van Cittert-Zernike theorem [vC34, vC39, Zer38]. It states that in paraxial approximation and for quasi-monochromatic light, the degree of spatial coherence j_{12} in an observation plane is related with the intensity distribution of an incoherent source by a Fourier-transform:

$$j_{12}(x_1, y_1, x_2, y_2) = \frac{e^{i\psi} \iint\limits_{\sigma} I(\xi, \eta) \exp^{-i\bar{k}(p\xi+q\eta)} \, d\xi d\eta}{\iint\limits_{\sigma} I(\xi, \eta) d\xi d\eta}, \tag{2.66}$$

where ξ, η specify coordinates of the source plane σ, $p = (x_1 - x_2)/R$, $q = (y_1 - y_2)/R$, $x_{1,2}$ and $y_{1,2}$ are spatial coordinates in the plane of observation, and R is the distance from the source plane to the observation plane. The wave number $\bar{k} = 2\pi/\bar{\lambda}$ is related to the mean wavelength and $\psi = \bar{k}((x_1^2 + y_1^2) - (x_2^2 + y_2^2))/2R$ is a phase factor. The latter can be neglected if $R \gg \bar{k}((x_1^2 + y_1^2) - (x_2^2 + y_2^2))$.

The propagation of the mutual coherence function in free space from one plane to another plane far away shows similar properties as the propagation of a wave field in the Fraunhofer-regime. Though, the physical quantities involved are completely different.

The emission of synchrotron radiation is an approximately incoherent process and the radiators contribute independently to the radiated intensity. This means Eq. (2.66) is valid and can be used to calculate the degree of spatial coherence of the emitted radiation at some distance from the source. The intensity distribution $I(\xi, \eta)$ of a synchrotron source can be described mathematically by a gaussian intensity distribution

$$I(\xi, \eta) = \frac{1}{2\pi\sigma_\xi\sigma_\eta} \exp\left(-\frac{\xi^2}{2\sigma_\xi^2} - \frac{\eta^2}{2\sigma_\eta^2}\right). \tag{2.67}$$

Inserting Eq. (2.67) into Eq. (2.66) the degree of spatial coherence can be calculated

$$\begin{aligned} j_{12}(\Delta x, \Delta y) &= \exp\left(-\frac{1}{2}\left(\frac{2\pi\sigma_\xi}{\bar{\lambda}R}\right)^2 \Delta x^2 - \frac{1}{2}\left(\frac{2\pi\sigma_\eta}{\bar{\lambda}R}\right)^2 \Delta y^2\right) \\ &:= \exp\left(-\frac{\Delta x^2}{2\sigma_x^2} - \frac{\Delta y^2}{2\sigma_y^2}\right), \end{aligned} \tag{2.68}$$

where $\Delta x = x_1 - x_2$ and $\Delta y = y_1 - y_2$ and the observation plane is supposed to be far from the source, i.e., $\exp(i\psi) \approx 1$.
This means that the spatial degree of coherence is also gaussian with σ-values of $\sigma_x = \bar{\lambda}R/(2\pi\sigma_\xi)$ and $\sigma_y = \bar{\lambda}R/(2\pi\sigma_\eta)$. The coherence area A_c can be defined as [Goo85]

$$A_c = \iint_{-\infty}^{\infty} |j_{12}(\Delta x, \Delta y)|^2 d(\Delta x) d(\Delta y). \tag{2.69}$$

Insertion of Eq. (2.68) into Eq. (2.69) yields the lateral coherence area of a gaussian source:

$$A_c = \pi\sigma_x\sigma_y. \tag{2.70}$$

The lateral coherence lengths l_x and l_y in x- and y-direction can be deduced from Eq. (2.70) by setting $A_c = l_x l_y$. This yields

$$l_x = \frac{1}{2\sqrt{\pi}} \cdot \frac{\bar{\lambda} R}{\sigma_\xi}, \tag{2.71}$$

$$l_y = \frac{1}{2\sqrt{\pi}} \cdot \frac{\bar{\lambda} R}{\sigma_\eta}. \tag{2.72}$$

The undulators of ID10 (ESRF) are installed in a high beta-section of the storage ring (cf. Sec. 2.2) with a source size of $s_{h,\mathrm{FWHM}} = 928\,\mu\mathrm{m}$ and $s_{v,\mathrm{FWHM}} = 23\,\mu\mathrm{m}$ in horizontal (h) and vertical (v) direction. It corresponds to the following σ-values of the gaussian-source of $395\,(\mathrm{h}) \times 10\,(\mathrm{v})\,\mu\mathrm{m}^2$. Using these values the lateral coherence length at a distance of 60 m from the source and at a photon energy of 8 keV can be calculated from Eq. (2.71) and Eq. (2.72): $7\,(\mathrm{h}) \times 262\,(\mathrm{v})\,\mu\mathrm{m}^2$.
Beamline ID01 on the other hand has a low beta-source and, therefore, the source size is smaller compared to ID10. The specifications provided by the ESRF machine division are $\sigma_h = 57\,\mu\mathrm{m}$ and $\sigma_v = 10\,\mu\mathrm{m}$ in horizontal (h) and vertical (v) direction. Thus, the lateral coherence length at a distance of $R = 45\,\mathrm{m}$ downstream is given by $35\,(\mathrm{h}) \times 197\,(\mathrm{v})\,\mu\mathrm{m}^2$ at 8 keV photon energy.

In simulations performed in this work the influence of partial coherence is taken into account by a gaussian convolution of the diffraction pattern. The width of this gaussian defines the degree of smearing of the diffraction pattern which is directly related to an effective source size. In following considerations the relation between a certain gaussian smearing of the diffraction pattern and the corresponding lateral coherence length at the sample position is given.

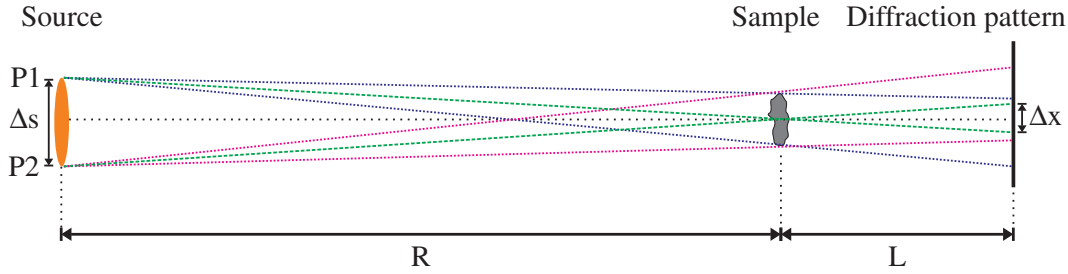

Figure 2.18: The convolution of the diffraction pattern due to partial coherence is related to the size of the source.

In Fig. 2.18 a simple schematic drawing illustrating the influence of an extended, mutually incoherent, source on the measured diffraction pattern is shown. Considering the two extreme points $P1$ and $P2$ as point sources then each of them would create a perfectly coherent diffraction pattern centered around the connecting line between $P1$ or $P2$ and the center of the object. In the plane of the Fraunhofer diffraction pattern these

intersection points are shifted to each other by a certain value Δx which results in the smearing, or convolution, of the diffraction pattern.
From this geometrical consideration the connection between the smearing of the diffraction pattern and the source size is given by

$$\Delta x = \frac{L}{R} \cdot \Delta s, \tag{2.73}$$

where R is the distance from the source to the sample, L is the distance from the sample to the detector, and Δx and Δs refer to the FWHM-values of the gaussian convolution in the diffraction plane and the source size, respectively.
Starting from Eq. (2.71) the lateral coherence length at the sample position l_t is given by

$$l_t = \sqrt{\frac{2\ln 2}{\pi}} \cdot \frac{\lambda R}{\Delta s}. \tag{2.74}$$

Inserting Eq. (2.73) into Eq. (2.74) yields

$$l_t = \sqrt{\frac{2\ln 2}{\pi}} \cdot \frac{\lambda L}{\Delta x} = 2\sqrt{2\pi \ln 2} \cdot \frac{1}{\Delta q}, \tag{2.75}$$

where $\Delta q = 2\pi/\lambda \cdot (\Delta x/L)$ has been introduced. Eq. (2.75) defines the relationship between a certain gaussian convolution of the diffraction pattern and the corresponding transverse coherence length at the sample position. For example, the lateral coherence length corresponding to a gaussian convolution of the diffraction pattern of one pixel with a size of $\Delta x = 20\,\mu\text{m}$, measured at a distance $L = 3.2\,\text{m}$ from the sample with a photon energy $E = 8\,\text{keV}$, is given by $l_t = 16.5\,\mu\text{m}$.

2.7 Phase Retrieval Methods

The reconstruction of the lost phases is an extremely challenging task in optimization which is due to the fact that the problem to be solved is nonlinear, large-scale, non-convex and non-smooth constraint [Mar07]. Nevertheless, during the last decades a number of different reconstruction algorithms were developed which are able to find the correct solution for a given amplitude measurement and state-of-the-art methods were even applied in three-dimensional structure determination as, e.g., on ceramic nanofoams [Bar07], test structures [Cha06b] or the mapping of a deformation field inside a nanocrystal [Pfe06].

Phase retrieval methods used to solve the described inverse problem were first introduced in astronomy and electron microscopy. The advantage of using electrons compared to x rays is the possibility to measure the amplitude of the electron wave field simultaneously in the image and diffraction plane [Ger72]. The first iterative reconstruction method was proposed by Gerchberg and Saxton with fixed amplitudes in both spaces (GS-algorithm). The GS-algorithm is based on the forward and inverse Fourier-transform cycling between real- and reciprocal space. The iteration process starts in real space where the amplitude of the complex field is set to the known values and the phase is chosen randomly. By application of the Fast-Fourier-Transform (FFT) the corresponding reciprocal space image is calculated and is used as a first guess for the diffraction pattern. Since also here the amplitude was measured it is replaced with the known values. The last step is the inverse Fourier transform which gives a new guess of the complex object function. This repetitive projection onto the measured amplitudes values drives the algorithm to find the correct phases that fulfill both the so-called real- and reciprocal space constraints. In Fig. 2.19 an illustration of the iterative procedure is shown.

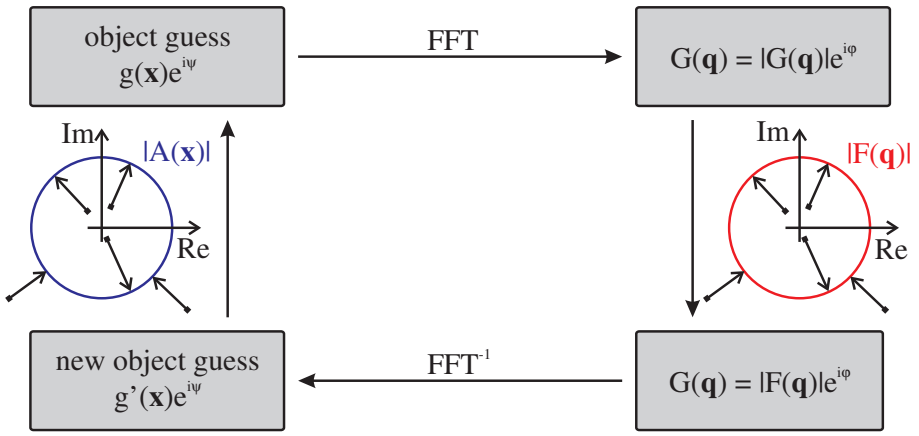

Figure 2.19: Gerchberg-Saxton algorithm. The phases of the complex wave field are iteratively refined by projecting the amplitude in real- as well as in reciprocal space onto the measured data $|A(\mathbf{x})|$ and $|F(\mathbf{q})|$, respectively.

The projection of complex numbers on the measured amplitudes are indicated by arrows

in the diagram pointing onto a circle with certain radius in the complex plane. This may illustrate the procedure to set the known amplitude while keeping the phase of the current guess of the object or diffraction pattern in each pixel of the image.

Later, this reconstruction method gained particular interest in the field of astronomy due to the fact that images from large telescopes suffer from atmospheric turbulences. Nevertheless, interferometric methods were available to measure the diffraction limited Fourier-transform of the object driving an increased interest to recover the corresponding image of the object. In 1978 Fienup proposed an extension to the GS-algorithm, the so-called error reduction algorithm, allowing for the reconstruction of the object only from the modulus of its Fourier-transform by relaxing the real-space constraints (cf. Fig. 2.20) [Fie78].

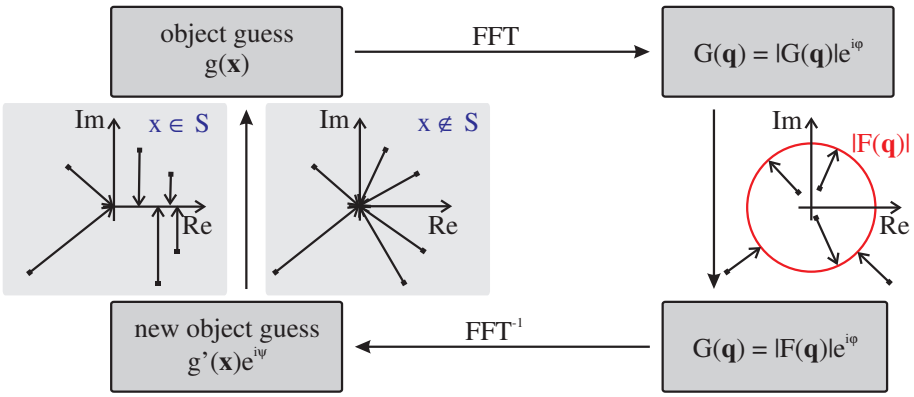

Figure 2.20: Error-reduction algorithm (ER). Since the amplitude in real space is not measurable, the constraints in real space reduce to positivity of the image and finite support. Inside the support which is indicated by $x \in S$ the imaginary part of the guessed image is set to zero. Outside the support, $x \notin S$, the electron density is set to zero in each iteration.

The real-space constraints of the error-reduction algorithm are the finite support and positivity of the object. The support refers to the area in real-space which is supposed to embed the object. In the context of x-ray diffraction on small and thin objects the first condition can be justified since the electron density must be positive. The finite support condition on the other hand is related to the oversampling described in Sec. 2.5. It demands that the size of the object is not larger than half of the model volume used for the reconstruction.

2.7.1 Uniqueness

Since a direct determination of the lost phase is not possible the question of the uniqueness of the retrieved image for a given measurement of its Fourier-amplitude arises. General properties of the Fourier-transform reveal already that three solutions may exist beside a certain complex solution in real space $f(x, y)$, namely: $f(x + x_0, y + y_0)$, $f^*(-x, -y)$ and $e^{i\varphi} f(x, y)$. A lateral displacement of the object, the inverted complex

conjugated function, the so-called twin-image, and the complex function multiplied with a constant phase factor have all the same modulus of the Fourier-transform and hence are all solutions of the inverse problem. Since these operations only involve the position and orientation of the object, but not its shape, a solution is called unique if only these trivial ambiguities exist. In the case when the same support condition is fulfilled for both the image $f(x, y)$ and its twin image $f^*(-x, -y)$ the probability that the reconstruction algorithm stagnates in a local minimum is enhanced. The latter often occurs for an object of certain symmetry. Methods to overcome the twin problem are discussed in [Fie86].

It is known from the theory of complex functions that in the one dimensional case the function can always be factorized and expressed by Hadamard's product [Bar84]. As will be shown in the following, the factorability of the function implies that the solution for the function is not unique and different, non-trivial, solutions of the inverse problem exist. Due to this knowledge it was originally surprising that the reconstruction of 2D-diffraction data did not seem to suffer from the multiple solution problem [Fie78]. The theoretical explanation for this was given by Barakat and Newsam [Bar84]. In this paper it was shown that the probability of multiple solutions is *pathologically rare* if the dimensionality of the problem is equal to or larger than two. Further explanations and computational examples in 2D are presented in [Bat82, Gar82, Fri82].

Nevertheless, non-unique solutions may always be found by looking for functions that are related by the convolution operation in real space. For example, two functions, $f_1(x, y)$ and $f_2(x, y)$, that can be represented in the following form

$$\begin{aligned} f_1(x, y) &= g(x, y) \otimes h(x, y) \\ f_2(x, y) &= g(x, y) \otimes h^*(-x, -y), \end{aligned} \tag{2.76}$$

have the same modulus of the Fourier-transform

$$|F_1(u, v)| = |F_2(u, v)| = |G(u, v)| \cdot |H(u, v)|. \tag{2.77}$$

However, as long as both $g(x, y)$ and $h(x, y)$ are not conjugate centro-symmetric, $f_1(x, y)$ and $f_2(x, y)$ are different objects.

In numerical investigations on low-dimensional systems Seldin showed in 1990 that these non-unique solutions are often related to local minima of the error metric [Sel90]. Especially if the non-unique solution is close to the global minimum, i.e., the error in the reciprocal space is small, the probability that iterative algorithms may be trapped in this local minimum is enhanced. Typically, one of the non-unique solutions is similar to the real solution whereas the other can be very different. These numerical investigations indicated that the probability to find a non-unique solution in iterative phase retrieval is the smaller the larger is the number of variables in the 2D-space. Similarly, the requirement of non-negativity is expected to facilitate a successful reconstruction.

In the following sections an overview of different iterative phase retrieval algorithms that were numerically implemented and applied during this work will be given.

2.7.2 Error Reduction Algorithm - Steepest Descent Method

The notation *error reduction-algorithm* is related to the fact that the error during the iterative procedure, defined by the quadratic error metric

$$\chi^2 = \frac{1}{N^2}\sum_q (|G(q)| - |F(q)|)^2, \tag{2.78}$$

diminishes or stays constant in each iteration step. In Eq. (2.78) $G(q) = \mathscr{F}(g(x))$ is the Fourier-transform of the electron density $g(x)$, and $|F(q)|$ is the square root of the measured intensity. In order to illustrate the close relationship between the ER-algorithm and a steepest-descent search method, the gradient of the error-metric at a certain point $g_k(x)$ of the N^2-dimensional parameter space will be explicitly derived below. It is closely following the derivation presented by Fienup in [Fie82].

The gradient of this N^2-dimensional parameter space using the error metric χ^2 of Eq. (2.78) is given by

$$\frac{\partial \chi^2}{\partial g(x)} = \frac{2}{N^2}\sum_q \left\{ (|G(q)| - |F(q)|) \cdot \frac{\partial |G(q)|}{\partial g(x)} \right\}. \tag{2.79}$$

The latter term can be transformed to

$$\begin{aligned} \frac{\partial |G(q)|}{\partial g(x)} &= \frac{\partial}{\partial g(x)} \left[(|G(q)|^2)^{1/2} \right] \\ &= \frac{1}{2|G(q)|} \cdot \frac{\partial |G(q)|^2}{\partial g(x)} \\ &= \frac{1}{2|G(q)|} \left[G(q) e^{\frac{i2\pi}{N} qx} + G^*(q) e^{\frac{-i2\pi}{N} qx} \right], \end{aligned} \tag{2.80}$$

where it was used that

$$\begin{aligned} \frac{\partial G(q)}{\partial g(x)} &= \frac{\partial}{\partial g(x)} \sum_y \left(g(y) e^{\frac{-i2\pi}{N} qy} \right) \\ &= e^{\frac{-i2\pi}{N} qx}. \end{aligned} \tag{2.81}$$

By introducing Eq. (2.80) in the expression for the gradient, Eq. (2.79), we find altogether

$$\frac{\partial\chi^2}{\partial g(x)} = \frac{1}{N^2}\sum_q \left\{ \left(G(q) - |F(q)| \cdot \frac{G(q)}{|G(q)|} \right) \cdot e^{\frac{i2\pi}{N}qx} \right\} + \frac{1}{N^2}\sum_q \left\{ \left(G^*(q) - |F(q)| \cdot \frac{G^*(q)}{|G(q)|} \right) \cdot e^{\frac{-i2\pi}{N}qx} \right\}. \quad (2.82)$$

Using the following simplification

$$G'(q) = |F(q)| \cdot \frac{G(q)}{|G(q)|} \quad (2.83)$$

and considering that Eq. (2.82) has the form of the inverse Fourier transform the expression reduces to

$$\frac{\partial\chi^2}{\partial g(x)} = 2\left(g(x) - g'(x)\right), \quad (2.84)$$

where $g'(x) = \mathscr{F}^{-1}\{G'(q)\}$ has been used. Notice that $g'(x)$ is identical to the image guess obtained in the error-reduction algorithm after replacing the amplitude $G(q)$ with the measured values $F(q)$ and the following inverse Fourier-transform.
The optimal step length to take along the gradient can be determined using the first order Taylor approximation of χ^2 around a certain point $g_k(x)$ in the parameter space, i.e.,

$$\chi^2 = \chi_k^2 + \sum_x \frac{\partial\chi_k^2}{\partial g(x)}(g(x) - g_k(x)). \quad (2.85)$$

The following ansatz for $g(x)$ reduces the error to exactly zero:

$$g_k''(x) = g_k(x) - \frac{\chi_k^2 \cdot \frac{\partial\chi_k^2}{\partial g(x)}}{\sum_y \left(\frac{\partial\chi_k^2}{\partial g(y)}\right)^2}, \quad (2.86)$$

which can be verified by inserting Eq. (2.86) into Eq. (2.85). Noting further that

$$\sum_y \left(\frac{\partial\chi_k^2}{\partial g(y)}\right)^2 = 4\sum_y \left(g_k(y) - g_k'(y)\right)^2 = 4\chi_k^2, \quad (2.87)$$

where Eq. (2.84) and Parseval's theorem has been used. The latter states that

$$\chi_k^2 = \frac{1}{N^2}\sum_q |G_k(q) - G_k'(q)|^2 \quad (2.88)$$

$$= \sum_x |g_k(x) - g_k'(x)|^2. \quad (2.89)$$

Therefore, the final result for the step length is given by

$$g_k''(x) - g_k(x) = -\frac{1}{4}\frac{\partial \chi_k^2}{\partial g(x)} = \frac{1}{2}(g_k'(x) - g_k(x)). \tag{2.90}$$

Since χ^2 is quadratic in $g(x)$ is turns out that this derivation predicts a step length half as long as the optimal value and, therefore, the step length to perform along the gradient should be

$$g_k''(x) = g_k'(x). \tag{2.91}$$

In case of a single intensity measurement the iterative procedure of the error-reduction algorithm can be identified to be equivalent to a steepest-descent method with a doubled step length [Fie82].

Nevertheless, it is known that steepest descent methods suffer often from so-called stagnation problems due to the steady step along the gradient without taking into account the surrounding curvature at a certain point in the N^2-parameter space. Usually, there is a strong tendency to be trapped in local minima. In the following different algorithms which show a better convergence are presented.

2.7.3 Hybrid-Input-Output Algorithm (HIO)

The error-reduction algorithm can be extended by introducing a memory from the previous iteration step. These algorithms are classified by so-called *input-output methods*. This time, the current guess of the object $g(x)$ is considered as the input for a certain non-linear operation driving the output $g'(x)$. The first three steps of the algorithm, i.e., Fourier transform of $g(x)$, application of the Fourier-modulus constraints and inverse Fourier transform (cf. right side of Fig. 2.21), are the same as in the case of the error-reduction algorithm.

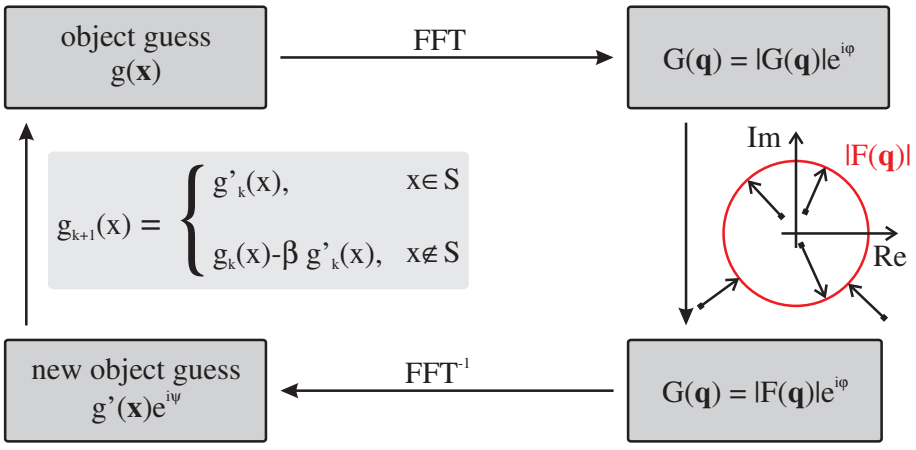

Figure 2.21: Hybrid Input-Output-algorithm (HIO)

Generally, it was found that a small change of the input $\Delta g(x)$ gives rise to a small change of the output: $\alpha \cdot \Delta g(x)$, where α is a constant parameter. Formulated inversely, if a change of $\Delta g(x)$ is desired in the output, the input needs to chosen as $\alpha^{-1}\Delta g(x) = \beta \Delta g(x)$. This is the origin of the constant parameter β as it is used in this algorithm. Its value is typically chosen between 0.5 and 1.0. Outside the support the values are progressively pushed to zero using the guess of the current and previous iteration. This is the main difference compared to the ER-algorithm where the output is set abruptly to zero outside the support. The basic input-output algorithm is defined as follows [Fie82]:

$$g_{k+1} = \begin{cases} g_k(x) & x \in \mathrm{S} \\ g_k(x) - \beta g'_k(x) & x \notin \mathrm{S}, \end{cases}$$

where S defines the area of the support. The choice of the output value drives the object guess outside the support continuously to zero as it is expected. Two further variants are conceivable.
The output-output algorithm is given by

$$g_{k+1} = \begin{cases} g'_k(x) & x \in \mathrm{S} \\ g'_k(x) - \beta g'_k(x) & x \notin \mathrm{S}, \end{cases}$$

and the Hybrid Input-Output constraints are

$$g_{k+1} = \begin{cases} g'_k(x) & x \in \mathrm{S} \\ g_k(x) - \beta g'_k(x) & x \notin \mathrm{S}. \end{cases}$$

The Hybrid Input-Output method (HIO-algorithm) is widely used in the field of phase recovery since it shows better convergence properties than the other algorithms. The notation *hybrid* is related to the definition of the constraints outside the support taking into account the input $g_k(x)$ as well as the output $g'_k(x)$.

The HIO-algorithm in combination with the error-reduction is a very convenient tool for phase retrieval. In certain circumstances of tight support or by using a low-resolution image it was shown that even complex valued objects, i.e., objects that are characterized by an amplitude as well as a phase shift, can successfully be reconstructed [Fie87, Fie90].

Note further that the Output-Output algorithm reduces to the error reduction algorithm for $\beta = 1$. Similar to the error reduction algorithm it suffers from stagnation problems [Wil05].

A generalization of the HIO-algorithm was proposed by R. Millane et al. [Mil97]. The idea is to relax the real-space constraints by introducing an iteratively refined constraint function $c_k(x)$. The algorithm works similar as the HIO-algorithm. Only the real-space constraint is altered to

$$g_{k+1} = \begin{cases} g'_k(x), & \text{if } |c_k(x) - g'_k(x)| \leq \epsilon \\ g_k(x) - \beta(g'_k(x) - c_k(x)), & \text{if } |c_k(x) - g'_k(x)| > \epsilon. \end{cases}$$

The parameter ϵ introduces a small tolerance in the application of the real space constraints instead of pushing them to the exact constraint values. The constraint function $c_k(x)$ can be the direct projection of the guessed image $g'_k(x)$ onto the usual real-space constraints and can be defined for example as follows [Var01]

$$c_k(x) = \begin{cases} c'_k(x) = \mathrm{Re}(g'_k(x)) & \text{if } x \in S \text{ and } \mathrm{Re}(g'_k(x)) > 0, \\ c'_k(x) = 0, & \text{if } x \notin S \text{ or } \mathrm{Re}(g'_k(x)) < 0. \end{cases}$$

In this way, the algorithm has more freedom to find a solution allowing for alternative search paths which might have been excluded otherwise.

It may be mentioned that the HIO-algorithm is a special implementation of a more general concept of iterated projections which was introduced by Elser in 2003. Since it is expected to provide similar results as the HIO-algorithm it has not been implemented and tested during this work. The interested reader may be referred to the specific literature [Els03, Els07, Wil05].

Modified HIO-algorithm

A further extension to the HIO-algorithm was proposed by Y. Nishino et al. [Nis03] handling difficulties in the reconstruction from incomplete diffraction data. If a certain amount of low frequency information is missing the HIO-reconstruction often suffers from stagnation and, due to the unconstrained central part of the diffraction pattern, a gaussian-shaped background typically appears in the reconstructed image.
The modification of the HIO-algorithm concerns the undefined central pixel. The problem of reconstruction lies in the fact that in this case the integrated electron density is unknown and needs to be restricted. The idea is to decrease the current guess for the total value of electron density if the mean deviation between measured amplitude $F(\mathbf{q})$ and calculated amplitude of the current guess $G(\mathbf{q})$ is larger than one and vice versa. This deviation is calculated by $\bar{m} = 1/N \sum_n (F(\mathbf{q}_n)/G(\mathbf{q}_n))$, where the sum extends over all pixels n inside the known part of the diffraction pattern. The amplitude of the central pixel is modified in each iteration in the following way:

$$G'(\mathbf{q} = 0) = m_{(0)} \cdot G(\mathbf{q} = 0), \tag{2.92}$$

where $m_{(0)}$ is related to $\bar{m}$ by

$$m_{(0)} = \alpha \left(\frac{1}{\bar{m}} - 1 \right) + 1. \tag{2.93}$$

The constant factor α is typically between 0.5 and 1.0. If $\bar{m}$ is larger than one, the object is supposed to contain sharper features which indicates that the current guess of the total value of electron density needs to be reduced, i.e., $m_{(0)}$ is smaller than unity. Inversely, the normalization factor $m_{(0)}$ is larger than unity if the object is broader than the current guess.

2.7.4 Shrink-Wrap-Method

The shrink-wrap-algorithm can be considered as an extension of the previously described methods. It was proposed by S. Marchesini et al. in 2003 [Mar03] and allows for image reconstruction without the need to provide a low resolution guess of the object. The idea of this method is the dynamical change of the support in certain intervals during the iterative reconstruction process. The numerical implementation is described below.

In the first iteration the autocorrelation image of the object is obtained by Fourier-transforming the measured diffraction pattern. The image obtained has always a center of inversion symmetry and the extension of the area with larger absolute values is roughly twice the size of the object. By introducing a threshold of about 4 % of the maximum amplitude the autocorrelation image can be used in order to define a first guess of the lateral extension of the object. Pixels of the object that have an amplitude larger than this threshold are expected to be part of the object whereas pixels with a lower value are supposed to lie outside the support. The support describes the area in real-space that is supposed to enclose the object. Obviously, the support defined in this way is much larger than the real object. It will be refined during the iterative reconstruction.

Typically, this initial support is used for the first 20 iterations of the reconstruction. Afterwards, the support is modified every 20 iterations. As a template for the new support serves an image of the current guess of the object that has been convolved with a gaussian-function. Now, this smeared image can be used to define a new guess of the support by setting a threshold to about 10 % to 20 % of the maximum absolute value of the image. Similarly as for the autocorrelation image, pixels with an absolute value larger than this threshold lie inside the support, all others outside.
During first iterations the convolution of the current guess of the object with the gaussian function is strong in order to guarantee that the shrinking of the support is not too fast. While the reconstruction proceeds the σ-value defining the width of the gaussian function is linearly decreased from 3 to 1.5 pixels. Therefore, the support becomes progressively more defined during the iterative process.

The shrinking of the support helps in some cases to constrain low-resolution diffraction data that could not be measured in the experiment.

2.7.5 Scanning Illumination Approach - Ptychography

In a contribution by R. Hegerl and W. Hoppe [Heg70] in the field of electron diffraction it is described that by appropriately choosing the illumination function of a thin crystal slab the usually sharp Bragg-peaks expand to a larger lateral size. Therefore, under certain experimental conditions the intensity of neighboring reflections can overlap giving rise to a defined interference pattern. The structure of this oscillating intensity distribution gives information about the relative phase shift between the two reflections and the knowledge of the phases for all reflections allows for the direct determination of the

crystal structure. Since the multiplication of the illumination function in object space corresponds in reciprocal space to a convolution of the Fourier-transforms of object- and illumination-function the nomenclature *ptychography* ($\pi\tau\nu\xi$ = fold) was chosen. The method is similar to holography where the phase is measured relative to a reference scatterer. See further [Hop69a, Hop69b].

Based on these ideas Rodenburg and Faulkner developed a reconstruction method for electron microscopy which can directly be addressed to x-ray microscopy as well [Rod04, Fau04]. The advantage of the method is that the object does not have to be compact and small in size, i.e., limited to a few micrometers, but instead the use of a pinhole, or well known aperture, defines the illuminated area on the sample that contributes to the measured signal. By shifting the illumination function, i.e., scanning the pinhole in front of the sample or alternatively scanning the sample in front of the fixed pinhole, a series of diffraction patterns are recorded, each encoding structural information with high spatial resolution. In case that the illuminated areas overlap, the phase problem can be solved and numerical simulations show that the reconstruction algorithm works very efficiently. The method was first successfully applied in scanning transmission electron microscopy (STEM) by Nellist et al. [Nel95, Nel97]. In the following an outline of the algorithm is presented [Rod04].

May $I(\mathbf{x})$ represent the illumination function on the sample and $g_k(\mathbf{x})$ a guess of the object at the k-th iteration. The iterative algorithm is then implemented as follows:

1. Multiply the object function with the illumination function giving $\psi_k(\mathbf{x}, \mathbf{X}_i) = g_k(\mathbf{x}) \cdot I(\mathbf{x}-\mathbf{X}_i)$, where the vector $\mathbf{X}_i$ describes the displacement of the illumination function.

2. Take the Fourier-transform $\tilde{\psi}_k(\mathbf{q}, \mathbf{X}_i) = \mathscr{F}[\psi_k(\mathbf{x}, \mathbf{X}_i)]$.

3. Replace the modulus of $\tilde{\psi}_k(\mathbf{q}, \mathbf{X}_i)$ with the measured values of the diffraction pattern at this position $\mathbf{X}_i$ of the illumination function, i.e.,
$\tilde{\psi}'_k(\mathbf{q}, \mathbf{X}_i) = |F(\mathbf{q}, \mathbf{X}_i)| \cdot e^{i\theta(\mathbf{q}, \mathbf{X}_i)}$. The phase θ of $\tilde{\psi}_k(\mathbf{q}, \mathbf{X}_i)$ remains unchanged.

4. Take the inverse Fourier-transform to calculate $g'_k(\mathbf{x}, \mathbf{X}_i) = \mathscr{F}^{-1}[\tilde{\psi}'_k(\mathbf{q}, \mathbf{X}_i)]$.

5. Update the object function giving a new guess of the object:

$$g_{k+1}(\mathbf{x}) = g_k(\mathbf{x}) + \frac{|I(\mathbf{x}-\mathbf{X}_i)|}{|I_{\max}(\mathbf{x}-\mathbf{X}_i)|} \cdot \frac{I^*(\mathbf{x}-\mathbf{X}_i)}{|I(\mathbf{x}-\mathbf{X}_i)|^2 + \alpha} \cdot \beta(g'_k(\mathbf{x}, \mathbf{X}_i) - g_k(\mathbf{x}, \mathbf{X}_i)). \tag{2.94}$$

The asterisk $*$ denotes the complex conjugate function. The term $\frac{|I(\mathbf{x}-\mathbf{X}_i)|}{|I_{\max}(\mathbf{x}-\mathbf{X}_i)|}$ can be considered as a weighting factor that takes into account that strongly illuminated regions have a larger contribution to the diffraction pattern than regions where only a small amount of photons hit the object. Not considering the additive constant α the second term $\frac{I^*(\mathbf{x}-\mathbf{X}_i)}{|I(\mathbf{x}-\mathbf{X}_i)|^2+\alpha}$ is identical to $1/I(\mathbf{x}-\mathbf{X}_i)$ and corresponds to a Wiener-filter. The constant α is used to prevent the division by zero if the amplitude of

the illumination function is zero. It is related to the effective deconvolution of the diffraction patterns which is taking place. The parameter β is a constant used in a similar way as in the HIO-algorithm driving the feedback of the algorithm. Depending on its value the importance of the previous or the current iterate is emphasized.

6. Proceed with the next position X_{i+1} of the illumination function $i+1$ where diffraction data were recorded.

Figure 2.22: Schematic drawing of the ptychography-method. A sample is illuminated with a homogeneous circular intensity distribution. If the diffraction pattern is known for every individual illumination function the phase problem can be solved by the described ptychographic phase retrieval method.

The main advantage of this method is that the shifting of the illumination function over the sample breaks geometrical symmetries of the object. In the case that only a single position is used the algorithm is a more general implementation of Fienup's algorithm, and it even reduces to the error reduction algorithm if the illumination function has a mask character and the following parameters $\beta = 1$ and $\alpha = 0$ are used in the reconstruction. The illumination function then acts as the compact support.
Even with complex-valued objects and in presence of a curved illumination function this method turns out to be a very convenient and fast converging tool for phase recovery. Further information, especially concerning the robustness of the algorithm in presence of noise, incoherence and inaccurate parameters, is given in [Fau05].

2.7.6 Genetic Algorithm

A very different algorithm based on the principles of evolution has been developed for the inversion of a diffraction pattern. This so-called genetic algorithm is a pure search algorithm and has a main advantage that further experimental parameters such as partial coherence or a special illumination function can be introduced a priori in the algorithm. In this way it is possible to formulate a model that is adapted to the specific experimental situation. Before presenting details of the numerical implementation it is worth to translate different terms used in genetics to phase retrieval from intensity data.

In biological terms the chromosome takes the role of the "blueprint" of an organism. In phase retrieval it is identified with a candidate solution, i.e., a guess of the object. Here, the candidate is a two-dimensional matrix that has in certain parts, which are enclosed by the support, a significant amount of electron density. The characteristic distribution of electron density in real space is related to a certain diffraction pattern in reciprocal space which is later used for the determination of the so-called fitness of the candidate solution. Furthermore, a gene of the chromosome can be identified with a single pixel and the so-called allele corresponds to the diversity of values, e.g. the thickness of the material, that one pixel stores as information content.

Obviously, evolution only works if a number of candidates with different capabilities are present that mix with each other. For the better ones the chance to pass their genes to following generations should be larger as for the others. Now, the idea is to create a so-called population of various candidates as expected solutions of a specific phase problem. In the beginning these candidates are randomly chosen from a certain parameter space. For each of them the corresponding diffraction pattern is calculated and the deviation from the measured data determines the fitness of the candidate. It is calculated by a χ^2-method. This means, the smaller the deviation between intensity data of the member and the measured data the better is the candidate adapted to the current situation. At this point the evolutionary process starts and successively two members are selected from the population to produce, by exchanging a certain number of genes, two children as new members of the population. The higher the fitness of the member the higher is also the probability that this member will be selected. Shortly after, their parents die so that the size of the population always remains constant.

From these explanations the phase retrieval algorithm can be summarized as follows. In a first step a population with e.g. 200 different members is created. For each of them the fitness is determined in the described way and based on that value the probability that the member is chosen for reproduction is calculated. Taking into account this probability two members of the population are selected that are going to exchange a certain number of pixels, this is the so-called crossover procedure. Usually, a fraction of about 30 % of the pixels was exchanged between the two members. Afterwards, a further procedure takes into account that a certain number of pixels may be randomly influenced by external processes, i.e., a certain number of pixels is given an arbitrary value of thickness. This

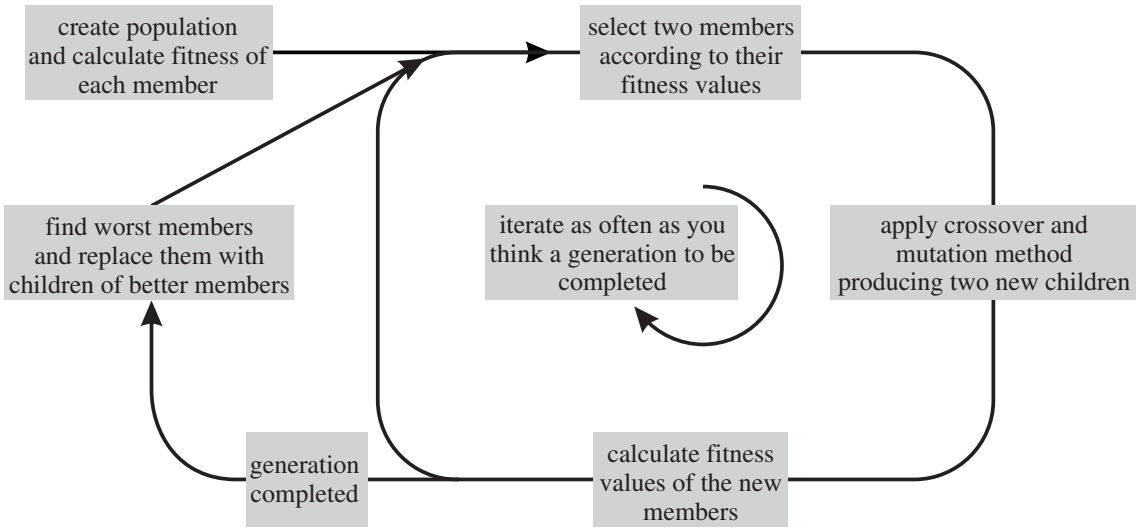

Figure 2.23: Iterative scheme of a genetic algorithm.

procedure corresponds in biology to mutation of the gene. The probability that a pixel changes its value arbitrarily is usually quite small ($\approx 0.001\,\%$). Now, there are two new children and their fitness is calculated for the next reproduction step. This procedure is repeated about 200 times for one generation to be completed. From one generation to the next a certain number of the worst members die and are replaced by children of better members.

The difference between the measured and the guessed diffraction pattern is the driving force of the algorithm. The hope is that the members that are closer to the solution finally win in the evolutionary process. The main advantage of the genetic algorithm is that only the forward Fourier-transform for propagation of the exit wave front from the sample to the detector is needed which can also be extended by introducing further the effect of partial coherence by a convolution operation applied onto the simulated diffraction pattern as well as the introduction of a certain illumination function if it is necessary. Nevertheless, since the genetic algorithm is a pure search algorithm the convergence – especially close to the solution – is very slow.
An introduction into the field of genetic algorithms was given by M. Mitchell [Mit98].

3 Experimental Setup for Coherent Diffraction Experiments

The lensless coherent diffraction method as described in Sec. 2.1 allows one to determine the structure of non-periodic objects with high spatial resolution. Nevertheless, the stability of the experimental setup and accurate sample positioning are important factors for the success of the CXDI-method. Various requirements as well as their technical implementation will be summarized and explained in this chapter.

3.1 Requirements

For photon energies of around 8 keV absorption by air has to be taken into account. For example, after a propagation distance of 1 m in air at atmospheric pressure 68 % of 8 keV-photons are absorbed (cf. Fig. 3.1). Therefore, in order to have the maximum signal possible and to reduce background scattering it was necessary to built a compact and portable vacuum chamber to house the experiments described herein.

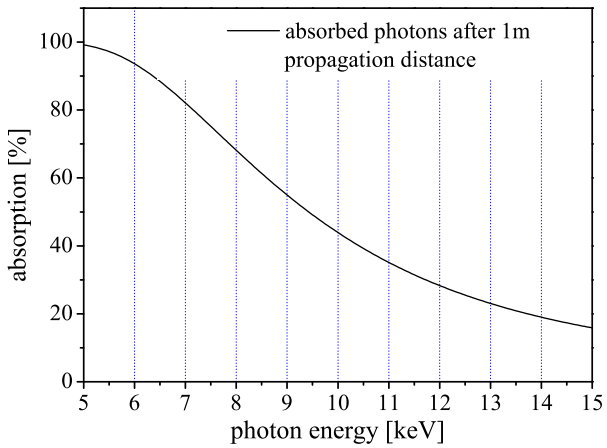

Figure 3.1: Percentage of absorbed photons after propagating a distance of 1 m in air at atmospheric pressure [BER].

In particular, the ptychographic-method of phase reconstruction (cf. Sec. 2.7.5) requires the very precise positioning of the sample in the x-ray beam. It could be shown in simulations that the scanning of the sample through the x-ray beam under condition of an overlapping illumination distribution has to be done very accurately. Effectively,

this accuracy must be of the same order of magnitude as the resolution obtained in the inverted image of a single diffraction pattern (cf. Sec. 5.5).
Furthermore, in order to decouple external vibrations from internal parts of the setup there should be no direct mechanical contact between the chamber and the technical equipment inside.

3.2 Setup for CXDI

Since the experiments described in this work have to be carried out at a third generation x-ray source the experimental setup is designed for high flexibility in transportation. For this reason, it is relatively small and compact.

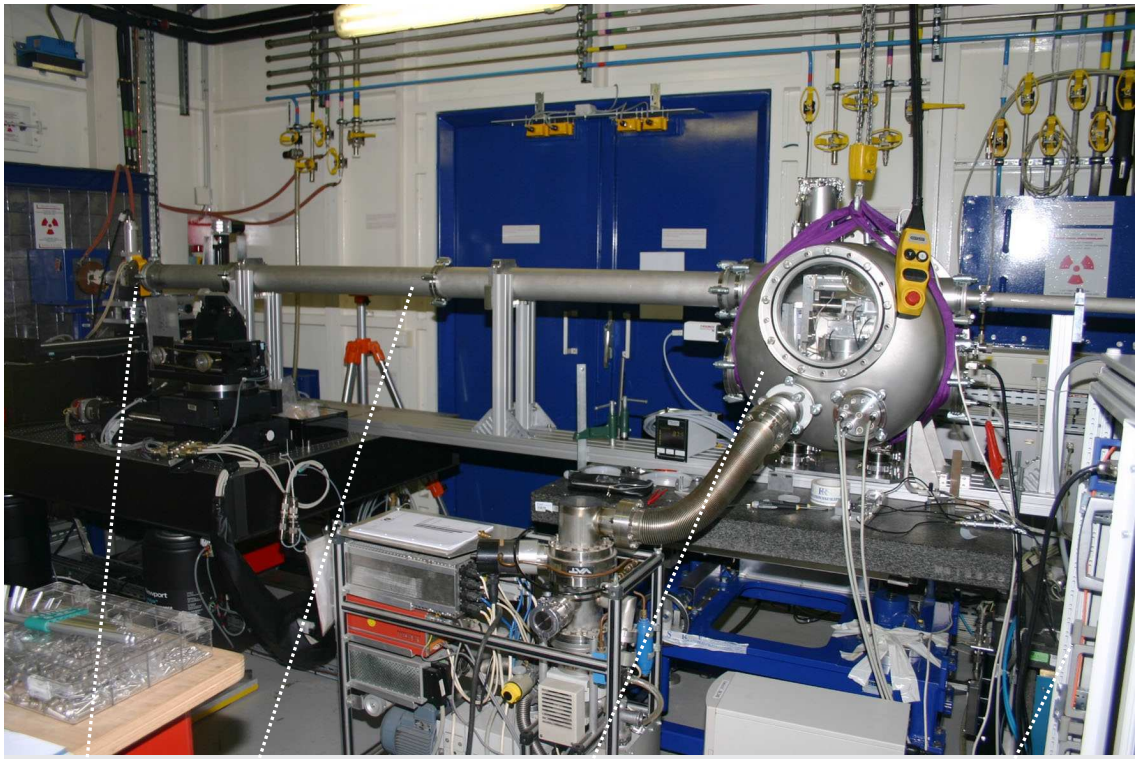

Figure 3.2: Experimental vacuum chamber installed at beamline ID10C.

The vacuum chamber can be installed on top of a standard optical table. Further components along the beam path, like vacuum tubes, beam-stop holder etc., are attached to a rail fixed on the same optical table. The vacuum chamber and the internal components are suitable for vacuum conditions down to about 10^{-6} mbar. In Fig. 3.2 a picture of the complete setup installed at beamline ID10C of the ESRF is shown. In this image, the x-ray beam enters the hutch from the right side through the smaller vacuum tube,

passes a series of slits and the vacuum chamber and leaves the chamber through the larger vacuum tube to the left. The Andor-CCD can be mounted on top of the chamber. In combination with suitable optics it is used to record high-resolution images of the incoming x-ray beam at the sample position (cf. Sec. 3.2.3).

In Fig. 3.3 a schematic drawing of the experimental setup is shown. The size of the beam is defined by a pair of slits which are about 1 m upstream of the sample. Behind that, a second or even third pair of slits, so-called guard slits, are used to reduce the scattering of the beam-defining slits (cf. Sec. 3.2.2). The x-ray beam, now with a size of approximately 10 µm in horizontal and vertical direction, illuminates the sample. Its Fraunhofer diffraction pattern is recorded at a distance of about $3-4$ m from the sample.

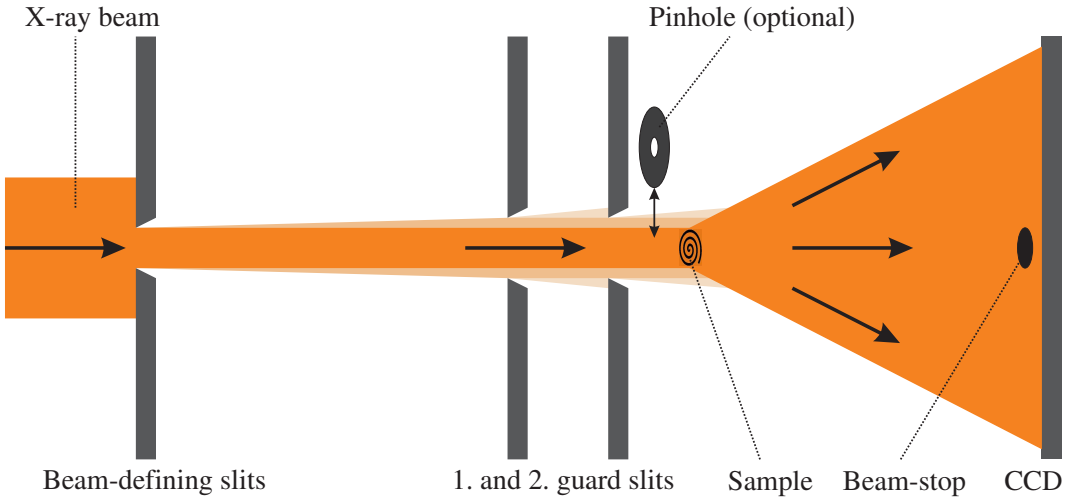

Figure 3.3: Schematic drawing of the setup.

In Fig. 3.4 a) various internal parts of the vacuum chamber are shown. In this image the x-ray beam is incident from the left hand side and leaves the chamber to the right. The first optical component shown in the picture is a slit-pair, the last guard slits, driven by linear piezo drives from Physikinstrumente (PI), followed by the xyz-stage of the pinholes and the sample-stage. The microscope objective images the fluorescence light of a scintillator screen which is positioned just after the sample. A piezo-motor enables to move the objective in a range of 400 µm in order to facilitate the positioning of the scintillator in the focal plane of the objective. The microscope optics can be moved out of the x-ray beam by remote control.
In Fig. 3.4 b) a view from the opposite side is shown. In this case a holder for Si-corners was mounted instead of the pinholes in order to investigate their refractive and absorptive properties at hard x-ray energies.

In the following sections the characteristics of different technical components will be successively summarized.

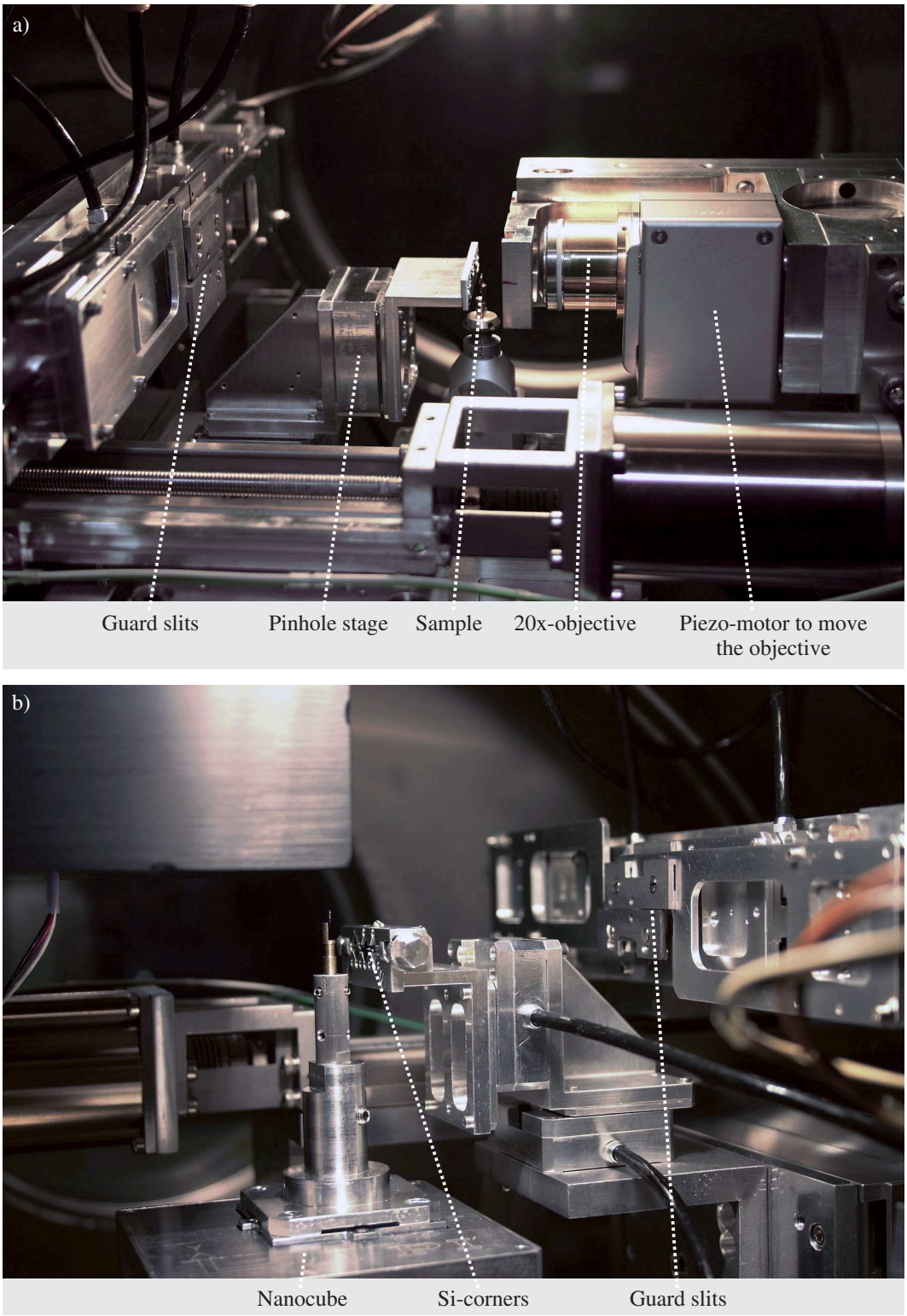

Figure 3.4: Arrangement of optical components inside the vacuum chamber. a) The x-ray beam is incident from the left side through the last guard slit. Optionally, pinholes or Si-corners can be positioned very close upstream the sample. A 20×-objective images the light of a scintillator screen closely after the sample position. The camera optics can be moved upwards opening a free pathway to the diffraction camera. b) Opposite view.

3.2.1 Sample Positioning

A combination of three translation stages (Huber, Micos) and a piezo-motor driven device (Physik Instrumente: Nanocube) allows for the positioning of the sample in all three dimensions with an accuracy on the nanometer-scale. These stages are located inside the vacuum chamber on an aluminum-plate that is attached to the optical table below the chamber but is not in direct contact with the chamber itself. In this way vibrations that are caused by the pumping system are decoupled from the measurement apparatus. Additionally, a rotation stage is foreseen for tomographic 3D-methods.
In Fig. 3.5 an overview of all motors used for the positioning of the sample and of the pinhole is shown.

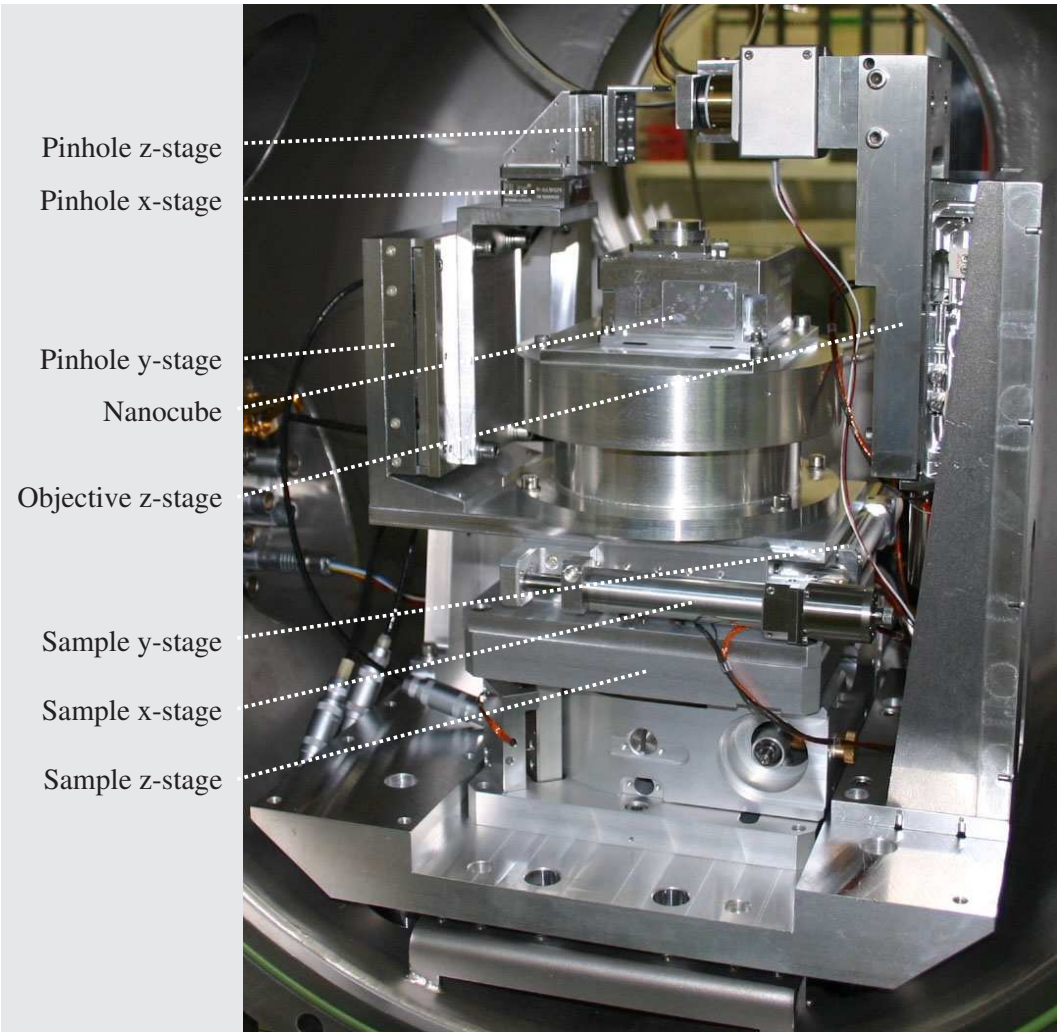

Figure 3.5: Overview of different motors for positioning of the sample, the pinhole and the objective.

All stepper motors of the experimental setup guarantee a repeatability in positioning of

about $1-2\,\mu$m. An overview of different parameters that are important for the controlling of the stepper motors is presented in App. B.

The piezo-motor device (Physik Instrumente, P-615K008) on top of the xyz-stage allows for the positioning of the sample with a resolution specified with 1 nm in all three dimensions [PIN]. The travel range of the device in closed-loop operation is $350\,\mu\text{m} \times 350\,\mu\text{m} \times 250\,\mu\text{m}$ in x, y and z-direction, respectively.

3.2.2 Slit Systems

The limited spatial coherence of the x-ray beam makes it necessary to select a coherent portion of the beam by introducing so-called beam-defining slits as a small aperture. Nevertheless, scattering at the edges of the slit blades gives rise to a strong signal on the detector and can spoil the measurement – especially in the low q-range. In order to reduce this scattering we are using a second or even third pair of slits with high quality blades. These so-called guard slits are positioned directly in front of the sample where they block a certain amount of the intensity scattered from the beam-defining slits. The slit blades are made of Tantalum. They are polished down to a surface roughness (RMS) of better than $0.013\,\mu$m (ADC USA, Inc. [ADC]). In Fig. 3.6 a very compact slit system used in the experiment is shown.

Figure 3.6: Slit system from ADC USA, Inc.

Inside the vacuum chamber the individual slit blades were positioned by ultrasonic linear piezo-motors with integrated linear encoder (Physik Instrumente: M-663). The advantage of these motors is the long travel range of 19 mm while keeping a high accuracy in positioning. The resolution is specified with 100 nm and the repeatability is around 300 nm. Additionally, theses motors are very compact and fast.

The positioning of the pinholes perpendicular to the x-ray beam was achieved with a similar linear stage but longer travel range of 50 mm (Physik Instrumente: M-665).

3.2.3 High-Resolution X-Ray Detector

A high resolution x-ray detector is used to visualize the intensity distribution of the incoming x-ray light at the sample position. It is an important tool to monitor the wave field which is highly sensitive to the positions of the individual slit blades or the settings of the monochromator. A slight offset of the experimental components on the micrometer scale can substantially change the intensity distribution at the sample position. A schematic drawing of the optical layout is shown in Fig. 3.7.

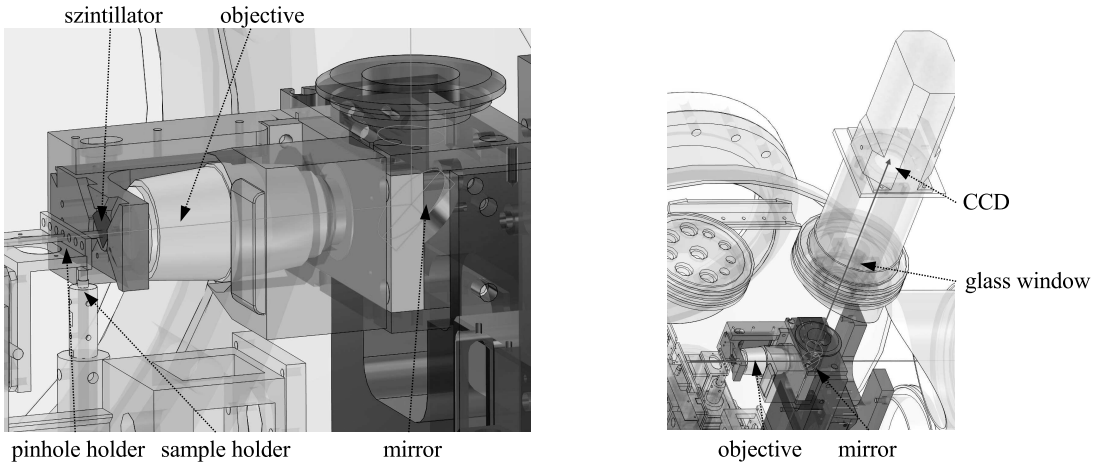

(a) Side view. **(b)** Top view.

Figure 3.7: Technical drawing of the high resolution x-ray detector illustrating the microscope optics.

The x-ray detector consists of a system of microscope optics and a charge coupled device (CCD). The working principle is based on imaging the light produced by a scintillator screen when illuminated with x-rays onto a CCD which is positioned outside the vacuum chamber.
The microscopic layout uses the principle of *Infinity Optics* meaning that the imaging is achieved by means of two lenses. The first lens converts the divergent fluorescence light coming from the scintillator into a parallel beam and the second lens focuses the light into the image plane. In our design a mirror is installed in the area of the parallel beam reflecting the light from the horizontal into the vertical direction. The first lens is a Nikon-objective (CFI60 Plan Fluor ELWD) with a long working distance of $7.0-8.1$ mm, numerical aperture of $NA = 0.45$, and $20\times$-magnification. The second lens is a so-called *tube lens* that focuses the parallel beam onto the CCD.
The optical resolving power R and the depth of focus DOF for this optical arrangement are given by

$$R = 0.61 \cdot \frac{\lambda}{NA} \approx 0.61 \cdot \frac{0.55\,\mu\text{m}}{0.45} \approx 0.75\,\mu\text{m}, \text{ and} \tag{3.1}$$

$$DOF = \frac{n\lambda}{2 \cdot (NA)^2} \approx \frac{0.55\,\mu\text{m}}{2 \cdot (0.45)^2} \approx 1.36\,\mu\text{m}. \tag{3.2}$$

Herein is $\lambda \approx 550\,\text{nm}$ the wavelength, NA is the numerical aperture, and $n \approx 1$ is the index of refraction of air. The wavelength of 550 nm was chosen since it is a typical value for fluorescence light emitted by the scintillator material used as will be shown in the following. The short depth of focus demands the accurate positioning of the scintillator perpendicular to the optical axis. It is achieved through a piezo-motor (piezosystem jena, MIPOS 500) with an encoded travel range of 400 µm enabling the positioning of the objective-lens with nanometer-precision.

Altogether, the optical system enables a magnification of the scintillator screen by a factor of twenty leading to a total field of view of $1024 \cdot 0.65\,\mu\text{m} = 665.6\,\mu\text{m}$ in both dimensions.

As scintillator material a Terbium doped Lutetium-Aluminum-garnet single crystal (LAG, $Lu_3Al_5O_{12}$) has been used. The advantage of this material compared to others, for example YAG (Yttrium-Aluminum garnet, Yttrium Z=39), is the higher stopping power of the material due to the larger atomic number of Lutetium (Z=71). Hence, the photons are absorbed in a relatively thin slab on the front side of the scintillator that is doped with Terbium acting as color centers. In our case, the thickness of the LAG-crystal is 170 µm, whereas the Te-doped top layer is only 20 µm thick. Due to the limited depth of focus of the objective lens a thin scintillator is preferable for high resolution imaging. However, the thinner the scintillator material of the active layer the smaller is the stopping power and less photons are detected and converted into visible light photons compromising the detective quantum efficiency (DQE) [Pat03].

The fluorescence light of the scintillator is imaged onto the CCD-detector where the visible light is converted into a measurable electronic signal. This is the last conversion step and the sensitivity of the CCD for a specific wavelength becomes important. The emission spectrum of Terbium shows a maximum at 550 nm with adjacent maxima between 350 nm and 500 nm. This wavelength falls into the sensitivity range of the chosen CCD (Andor DV434-BV) having its maximum quantum efficiency at 550 nm with a value of about 90 % (cf. Fig. 3.8).

The size of the CCD-chip is $(13.3 \times 13.3)\,\text{mm}^2$. It has 1024×1024 pixels with a pixel size of 13 µm and can be readout with a maximum clock frequency of 1 Mhz and a nominal analog to digital resolution of 16bits. In this conditions the readout time of a full frame is one second. The Andor-CCD is controlled via a PCI-card (CCI-010) and can be operated with a C++-software.

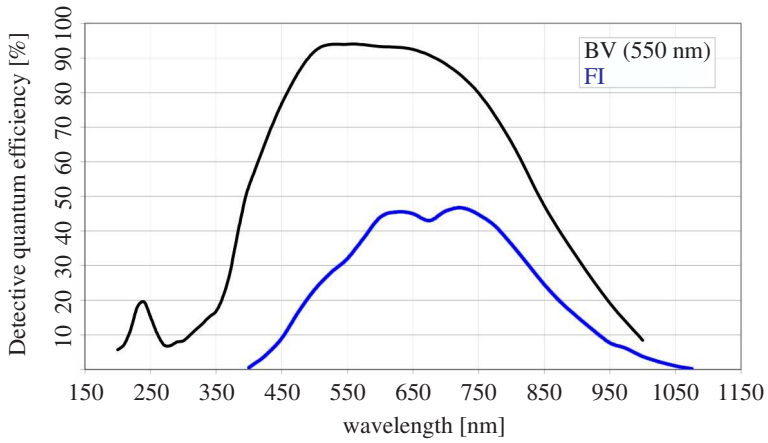

Figure 3.8: Detective quantum efficiency (DQE) of the back-illuminated Andor-CCD head (BV) which is optimized for the visible spectrum around 550 nm. The blue line shows the DQE of the front illuminated CCD-head (FI). Our detector contains the BV-CCD-head.

Alternatively a 4×-objective lens was used in a different design of the camera. The objective, a Nikon Plan Apochromat (CFI60-series) has a numerical aperture of $NA = 0.2$ and a working distance of 15.7 mm. In comparison to the 20×-objective the positioning of the scintillator is less demanding due to the larger depth of focus $DOF = 6.9\,\mu\text{m}$. The resolving power R can be calculated to $R = 1.7\,\mu\text{m}$ for this objective.
Further detailed information on the optics and the CCD-detector can be found in [Flü04].

Distortions and Flat-Field Correction

Flat-field correction describes the procedure to divide the image measured with the sample by a second image recorded under the same experimental conditions but without sample in the beam path. This second image contains all information on image imperfections related to the beam-profile or a spatially dependent sensitivity of the scintillator. The division by the flat-field image allows to extract the information on the absorbed intensity only due to the sample. It is related to the Lambert-Beer law $I_{\mathrm{meas}} = I_{\mathrm{flat}} \cdot \exp(-\mu d)$, where μ is the linear absorption coefficient and d the thickness of the material. Provided that the absorption coefficient for the given photon energy is known, the thickness of the material can be determined for each pixel: $d = -1/\mu \cdot \ln(I_{\mathrm{meas}}/I_{\mathrm{flat}})$. In Fig. 3.9(a) the raw image of a Ni-mesh with a periodicity of 300 lines/inch and in Fig. 3.9(b) the corresponding flat-field corrected image are shown.

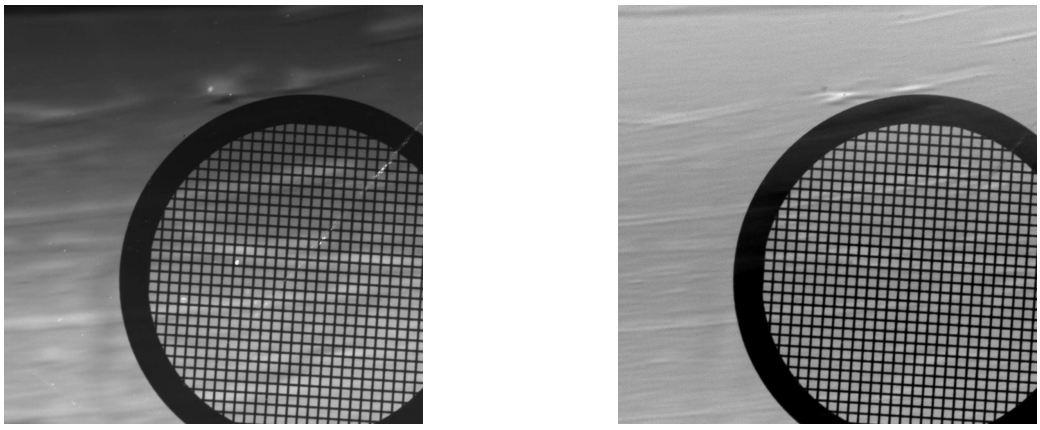

(a) Raw image **(b)** Flat-field corrected image

Figure 3.9: X-ray transmission images of a Ni-mesh with a periodicity of 300 lines/inch in raw format (a) and after flat field correction (b) as taken with the Andor-camera using the 4×-objective. The distance between lines is 85 µm.

The images of the high-resolution x-ray detector are free of distortions and aberrations as can be verified in Fig. 3.9. The lines of the Ni-mesh appear straight.

Spatial Resolution

The determination of the point-spread function of the detector with 4×-objective was performed using a GaAs-wafer with a sharp edge. This edge was mounted perpendicular to the beam and gave a step-like contrast in the measured x-ray image (cf. Fig. 3.10). A line profile over this edge at the best focal position of the objective lens reveals the point-spread function of the detector.
In order to fit the line profile the error function was used. Mathematically, it is defined as

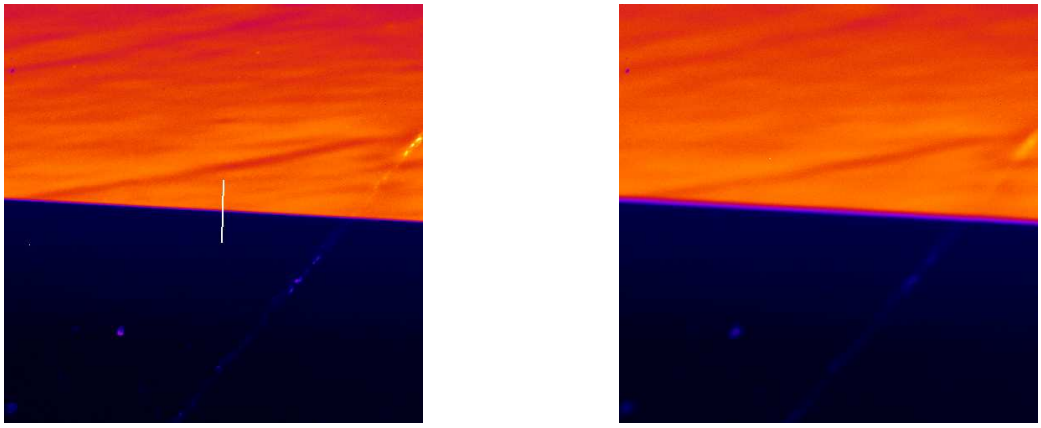

(a) Knife edge image at best focal position. **(b)** Focal position is 150µm offset.

Figure 3.10: Knife edge images taken with the high resolution camera with 4×-magnification at 10 keV photon energy. The image shows the flat x-ray beam. The lower part (black colored) is obscured by a GaAs-wafer piece. A line profile over the edge reveals the point spread function of the detector. The position of the line profile which was used for this analysis is indicated by a white line in image (a). A displacement of 150 µm in the positioning of the objective lens already leads to a substantial reduction in spatial resolution (cf. Fig. (b)).

$$\mathrm{erf}(x) = \frac{2}{\sqrt{\pi}} \int_0^x e^{-t^2} dt. \tag{3.3}$$

Therefore, the derivative of the error function is a Gaussian which can be identified as the point-spread function of the detector. The width and the offset in x of the Gaussian can be modeled by introduction of two parameters σ and x_0, respectively. The derivative is given by

$$\frac{d}{dx}\left(\mathrm{erf}\left(\frac{x-x_0}{\sqrt{2}\sigma}\right)\right) = \sqrt{\frac{2}{\pi\sigma^2}} \cdot \exp\left(-\frac{(x-x_0)^2}{2\sigma^2}\right). \tag{3.4}$$

The evaluation of the fit yields a value of $\sigma = 1.38$ pixels. From this value the FWHM of the point-spread function can be calculated to $\mathrm{FWHM} = 2\sqrt{2 \cdot \ln 2} \cdot \sigma \approx 2.355 \cdot \sigma \approx 10.6$ µm for an effective pixel size of 3.25 µm using the 4×-objective.

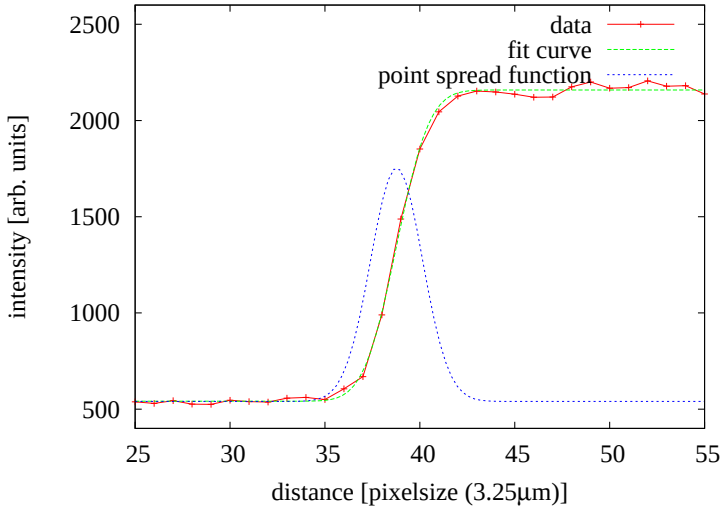

Figure 3.11: Line profile over the knife-edge. The FWHM of the point spread function is approximately 10.6 µm.

Linearity

The linearity of the detector was investigated by variation of the exposure time. A certain area of the flat image with a size of 357 × 220 pixels was cropped and the mean signal per pixel calculated. In Fig. 3.12 the result of dose versus exposure time is presented. The response of the detector is linear with increasing exposure time up to a signal of approximately 30 000 ADC-units.

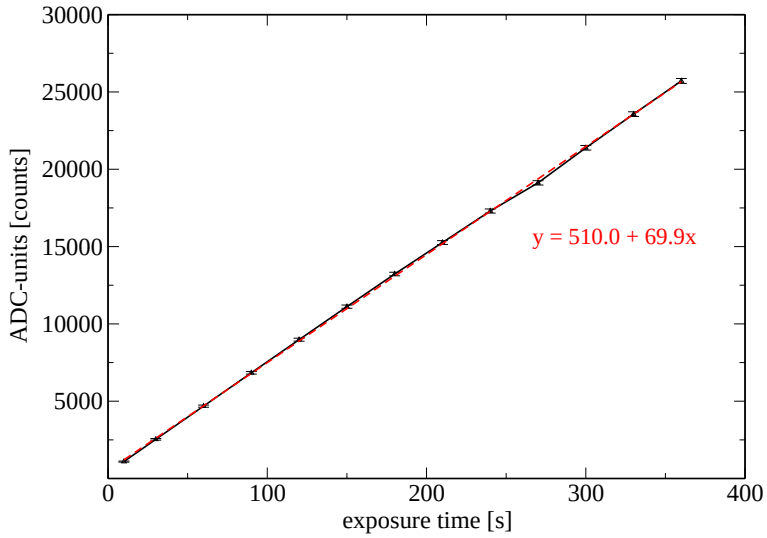

Figure 3.12: Linearity of detector response.

3.2.4 Beam-Stop

At the end of the flight tube two translation stages enable the positioning of a primary beam-stop directly in front of the direct-illuminated CCD which is used to record the diffraction pattern. The beam-stop holder allows for the mounting of three different beam-stops that can be aligned using two stepper-motors (cf. Fig. 3.13). The positioning in the horizontal direction is achieved by a vacuum-compatible translation stage whereas the vertical movement is performed with a z-stage outside the vacuum-tube (Huber). Since the position of the vacuum-tube is fixed the movement of the beam-stop in vertical direction is only possible due to two diaphragm bellows which are used to connect the z-stage to the vacuum-tube.

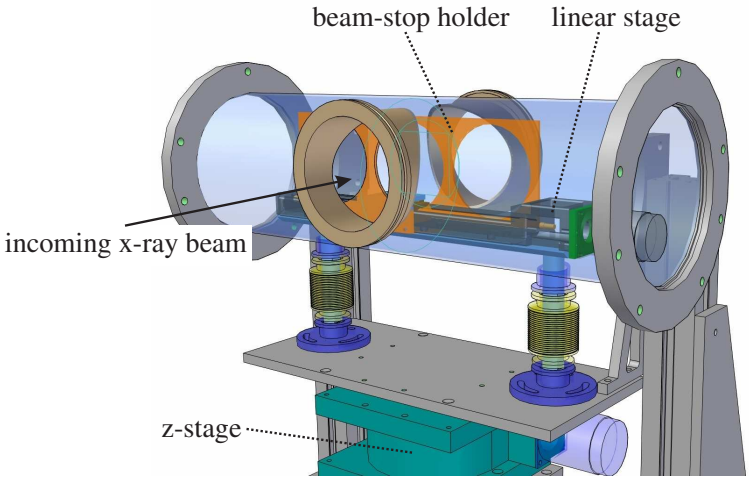

Figure 3.13: Technical drawing of the beam-stop-holder.

Typically, the beam-stop covers a certain amount of diffraction fringes of the sample which limits the maximum size of the object that can be imaged. In the present geometry of the setup, i.e. a distance of 4 m between sample and CCD and using a very small beam-stop with a size of 0.3 mm in diameter, the maximum sample size is approximately 6 µm at 8 keV photon energy.

3.3 Back-illuminated CCD-Detector

The diffraction patterns measured at the ESRF (ID01, ID10C) were recorded using a back-illuminated CCD from Princeton Instruments (*PI-SX 1300*). The dimensions of the detector are 1340 × 1300 pixels with a pixel size of 20 µm. The imaging area is therefore $(26.8 \times 26.0)\,\mathrm{mm}^2$. The A/D-converter works with nominal 16bit-digitization. The specification of its quantum efficiency is presented in Fig. 3.14.
At around 7 keV the detector has a detective quantum efficiency of about 20 %. This means that only every fifth photon is seen by the detector due to the relatively low probability of absorption in the depletion layer of the silicon chip. Nevertheless, if a

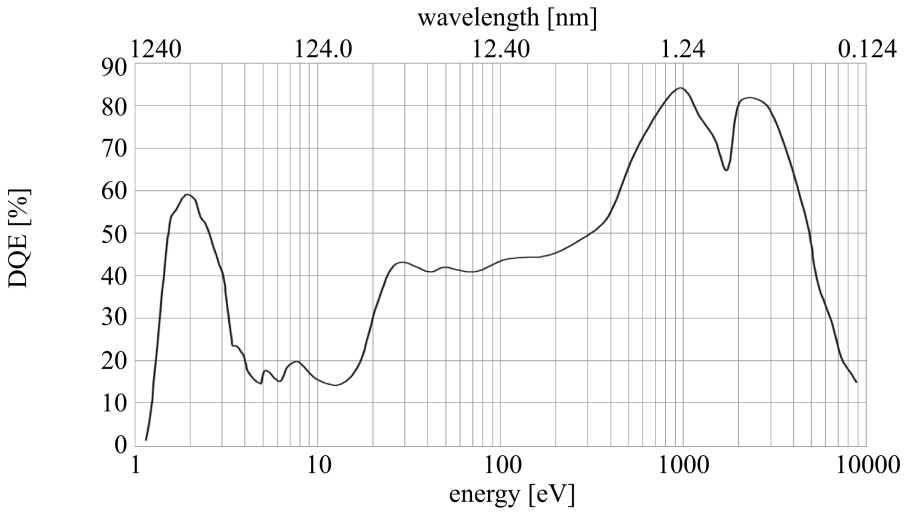

Figure 3.14: Detective quantum efficiency of the back-illuminated PI-SX1300 detector as specified by Princeton Instruments.

photon is absorbed in the sensitive layer the number of produced electrons is fairly large giving a signal of approximately 800 ADC-units per photon after digitization. Thus, this kind of detector is given the attribute of *single photon counting capability*. Whereas this property is desirable in the high q-range, because of low intensities, it becomes a limitation at lower q-values. In the latter case, the full well of a single pixel is filled in a very short time due to the high photon flux and the CCD has to be readout at frequent intervals. If the beam-stop is very small the accumulated readout time can even be much larger than the effective exposure time.

Therefore, in order to cover the dynamic range of the diffraction pattern with differences in counting rate of at least four orders of magnitude it is necessary to record multiple diffraction images and sum them up to get the final pattern. Nevertheless, the DQE of direct-illuminated CCD's is still higher than for most high resolution phosphor-based detectors. The latter have a quantum efficiency of about 1-2%.

3.4 Sample Preparation

Most of the samples used during this work were produced by electron-beam lithography. The preparation process requires a series of steps that will be described in the following.

In the beginning the substrate material is a 4-inch silicon-wafer with a thickness of 370 µm. Additionally, the top and bottom side of the wafer is coated with a Si_3N_4-layer with a thickness 200 nm. Typically, on one side there are already certain pre-structured areas present where the Si_3N_4-layer was removed from the wafer. These wafers are commercially available (e.g. Silson Ltd. [SIL]).

After cutting the wafer in pieces they are spin coated with a positive e-beam resist (PMMA 600K) by a Semitec CPS20 spin-coating system. The coating is achieved by spinning the wafer pieces at 6000 revolutions per minute for a time of 30 s. Then, the wafer pieces were baked on a hot plate at 165 °C for a total time of five minutes in order to remove the remaining solvent. This procedure was done twice in order to obtain a double coated wafer. This resist layer is the basis for the following processing.

Afterwards, the desired micro-structure is written into the resist layer by exposing certain areas to an electron beam (cf. Fig. 3.15 a)). The interaction with the electron beam induces the breaking of chains of the resist molecules (chain-scission) and as a result, the parts of the resist that were exposed to the electron beam are, compared to the non-exposed parts, easier to remove by submerging the wafer in a special solution (AR-P 600.55). The latter processing step is called development (cf. Fig. 3.15 b)). The result is a mask which serves as a negative template to create the desired two dimensional gold-structure.

The 150 nm thick gold layer is sputter-deposited on top of this mask (cf. 3.15 c)). A layer of 15 nm chromium below the gold layer ensures a sufficiently high adhesive strength between the gold-structure and the Si_3N_4-layer. Afterwards, the remaining resist is removed in an Aceton-bath (cf. 3.15d)). This processing step is called lift-off.

In a final step the silicon is etched from the backside by KOH-etching (50 %-solution). The KOH-solution with a temperature of 80°C attacks strongly the silicon but much less the Si_3N_4-layer. The etching rate for the silicon is approximately $30 - 40\,\mu m/h$ and after about $10 - 12$ h the silicon is completely removed through the whole thickness of the silicon-pieces. The final result is a window with a Si-frame and a free standing Si_3N_4-membrane which can be positioned perpendicular to the x-ray beam. On the top of the membrane is the Au-microstructure. The lateral size of the two dimensional gold samples was typically $3 - 10\,\mu m$ and the thickness of the gold-layer was 150 nm. Further detailed information concerning different methods of lithographic processing can be found in [Kur05].

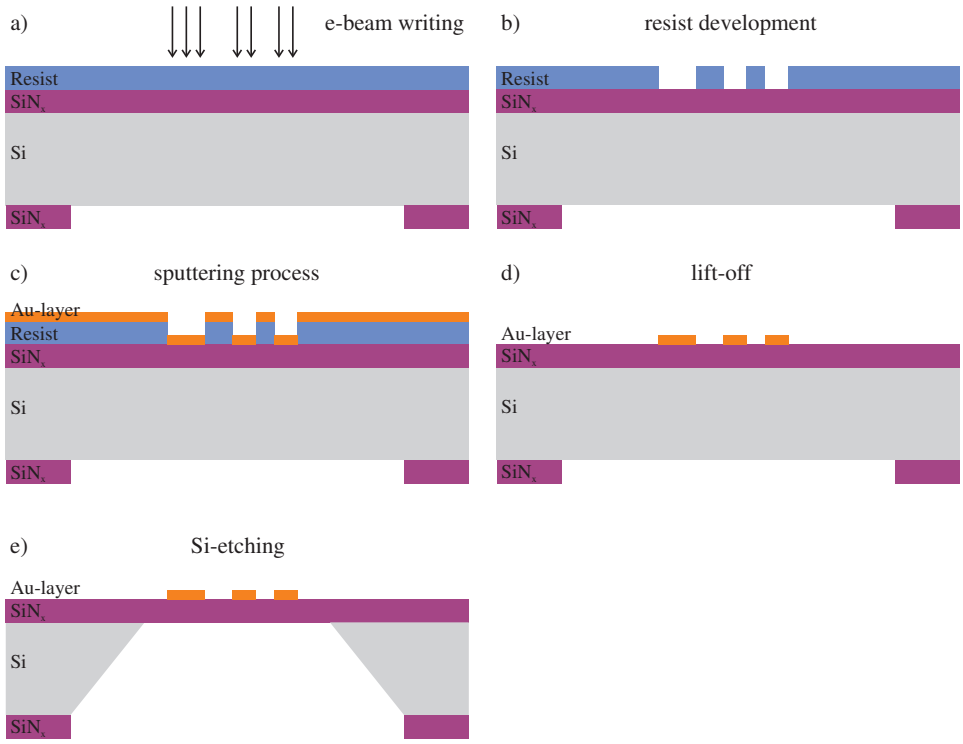

Figure 3.15: Schematic outline of the sample preparation procedure. a) An electron-beam writes the desired micro-structure into a layer of a positive resist. After the development, cf. b), the gold layer is sputter deposited on top of the nano-structured resist mask. The residual parts of the resist are removed in a "Lift-Off"-process and the gold-structure remains finally on top of the Si_3N_4-substrate, cf. d). In a final step the Si-substrate is etched from the backside in a KOH-etching procedure. The final result of this process is a free standing Si_3N_4-membrane with a gold-structure on the top side.

4 Experimental Results

In this chapter experimental results obtained in CXDI-experiments at the ESRF in Grenoble are presented. The measurements were carried out at beamlines ID01 and ID10C and different experimental parameters as well as a schematic layout of the last optical components that are important for these measurements will be introduced in the following sections. The photon energy in these experiments was varied from 7 keV to 10 keV giving a speckle size in the measured diffraction pattern of about 120 µm for our samples with a size of $(3-5)$ µm. The distance between sample and detector was about 3.2 m. The pixel size of the directly illuminated CCD was 20 µm allowing for a $(5-8)\times$-oversampling in each dimension.
The samples investigated were lithographically prepared two-dimensional gold structures (cf. Sec. 3.4), a piece of a photonic-crystal, as well as a cluster of gold spheres. The diffraction pattern of the gold-spheres will be further analyzed with regard to incoming photon flux and the resolution will be estimated in connection with simulations of Sec. 5.2.
The vacuum chamber introduced in Chap. 3 was only used in experiments at ID10C.

4.1 Measurements at ID01 (ESRF)

The first experiment was performed at beamline ID01 of the ESRF. The possibility to operate this beamline in a windowless mode makes it especially attractive for CXDI-experiments. As already mentioned in Sec. 2.6 this beamline is located on a low β-section of the storage ring with the rms source size of 56.9 µm in horizontal (H) and 10.2 µm in vertical (V) direction, as given by the ESRF machine division. Such a source size should provide a theoretical coherence length of about 36 µm (H) and 201 µm (V) at a distance of 47 m from the source for x-rays with an energy of 8 keV.

4.1.1 Slit Setup at ID01

In our experiment, the photon energy was adjusted to 7 and 10 keV. The double-crystal Si-111 monochromator was located at a distance of 34.0 m downstream from the source and the first pair of slits, used to define the beam size, at a distance of 38.3 m. In Fig. 4.1 a schematic drawing indicating the position of individual slit pairs and the sample is shown.
Additionally, two pairs of slits were used in front of the sample in order to define the coherence area and to clean the x-ray beam. The first of them was positioned 46 m from the source and was fixed to a size of 40(H) × 40(V) µm^2 and the second pair was positioned 80 cm further downstream acting as a guard slit in order to suppress the

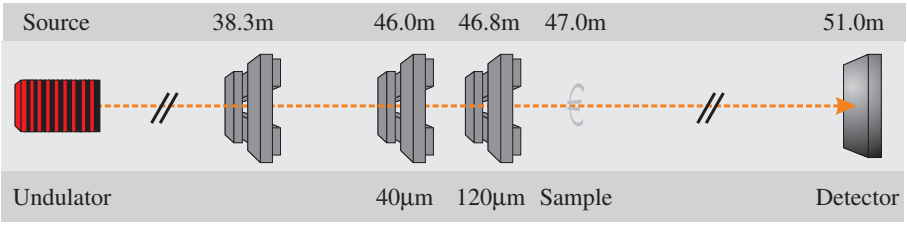

Figure 4.1: Arrangement of slits to define and clean the x-ray beam.

background scattering from the beam defining slits. The opening size was varied during the experiment between 100 µm and 120 µm in both directions.

4.1.2 Detectors

Typically, the intensity decrease is given by a power law dependency of at least $I \propto q^{-3}$ and, therefore, the dynamic range of the diffraction pattern is large. For example, in order to cover all length-scales from 30 nm to 3 µm, i.e., two orders of magnitude, the dynamic range of the corresponding diffraction pattern is at least 10^6 photons.

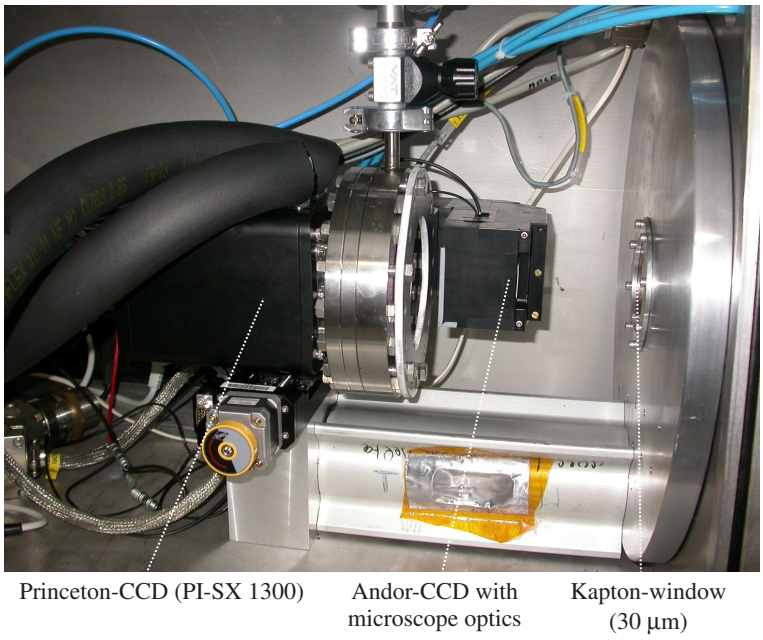

Figure 4.2: Princeton CCD-detector and Andor-camera mounted at the ESRF (ID01).

We explored the possibility of using two detectors with differing sensitivity in order to record the diffraction patterns. The main detector was a directly illuminated Princeton CCD with a pixel size of 20 µm (PI-SX 1300). The chip size is $26.0 \times 26.8\,\mathrm{mm}^2$ corresponding to a number of 1300×1340 pixels. The direct detection of x-ray photons

allows for the detection of single photons. At medium gain one photon of 10 keV is converted to about 800 ADC-units. The well of a single pixel is full if 80 photons hit the pixel. This detector is especially suited for the measurement of intensity at large q-values since there, the scattered photon flux is very low. Depending on the size of the beam-stop the exposure time was varied from about 10 milliseconds up to a few tens of seconds.

The second detector was the high-resolution camera (cf. Sec. 3.2.3). Due to its lower sensitivity this detector is especially suitable to measure the central part of the diffraction pattern using a small beam-stop with a diameter of 0.3 mm. Both detectors were mounted on the same stage allowing for the subsequent measurement of the inner and the outer part of the diffraction pattern.

In Fig. 4.2 the arrangement of detectors is shown. The detectors were positioned inside a cylindrical tube with atmospheric pressure which is itself located inside a larger vacuum vessel. The communication with the detectors is possible through a flexible feed-through. The inner chamber is movable in a range of approximately 3 m along the optical axis of the beamline. It enables to adjust the distance between sample and detector in a range of 1.5 m to 4.5 m.

4.1.3 Lithographically Prepared Au-Samples

Measurements were carried out on lithographically prepared samples with a gold layer of 150 nm thickness (cf. Sec. 3.4). The phase shift induced by the gold-layer is relatively small, i.e., $\Delta\varphi(10\,\mathrm{keV}) = -0.23\,\mathrm{rad}$, using $\delta(10\,\mathrm{keV}) = 3.02 \cdot 10^{-5}$ (cf. Eq. (2.32)). Thus, the object can be considered as real-valued producing a centro-symmetric Fraunhofer diffraction pattern. A fraction of 3.2 % of the incoming photons are absorbed by the 150 nm-gold layer at the photon energy of 10 keV.

In Fig. 4.3 the diffraction pattern of the Ettlinger Tor sample measured at 10 keV photon energy is shown. The shape and the size of the object is given in the inset of the image. The sample-detector distance was 3.37 m which gives a speckle size of approximately 84 µm for this sample with a lateral size of 5 µm. The diffraction pattern is the sum of 1000 images each recorded with an exposure time of 0.6 s. The total exposure time of the image including the readout time of the CCD is about half an hour. In order to prevent the fast saturation of the Princeton-CCD it was necessary to use a beam-stop with a diameter of 2 mm.

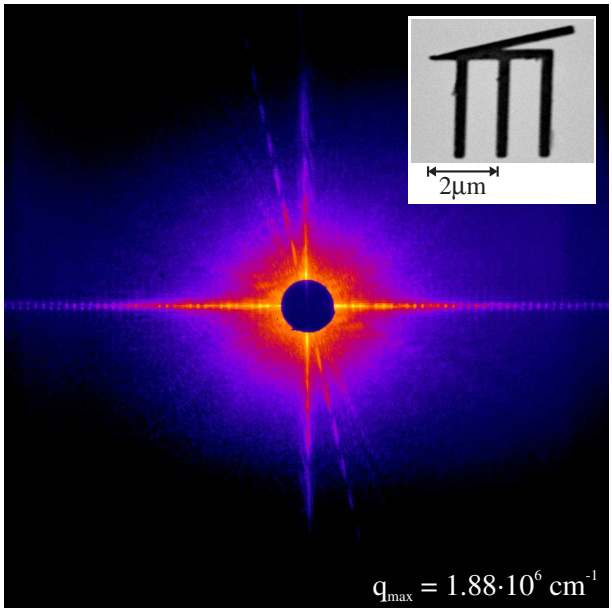

Figure 4.3: Diffraction pattern of a lithographically prepared gold sample measured at 10 keV photon energy. The shape of the sample is akin to the Ettlinger Tor in Karlsruhe. The maximum scattering vector is $1.88 \cdot 10^6\,\mathrm{cm}^{-1}$ along the horizontal and vertical direction.

The image in Fig. 4.3 is corrected for the background related to the readout characteristics of the detector. Nevertheless, especially in the central part of the diffraction pattern there is still a certain amount of a background signal present which is caused by slit scattering and a contribution of higher harmonic photons. In some cases, the

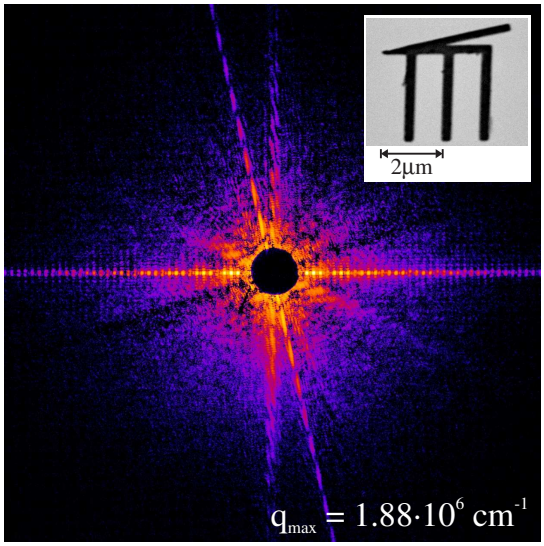

(a) Background-corrected diffraction pattern.

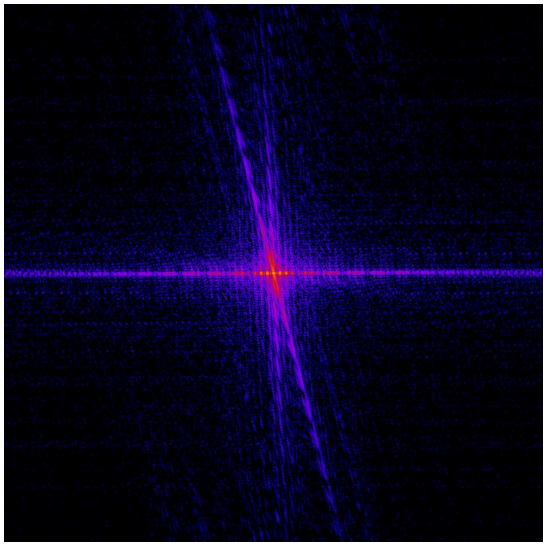

(b) Calculated diffraction pattern.

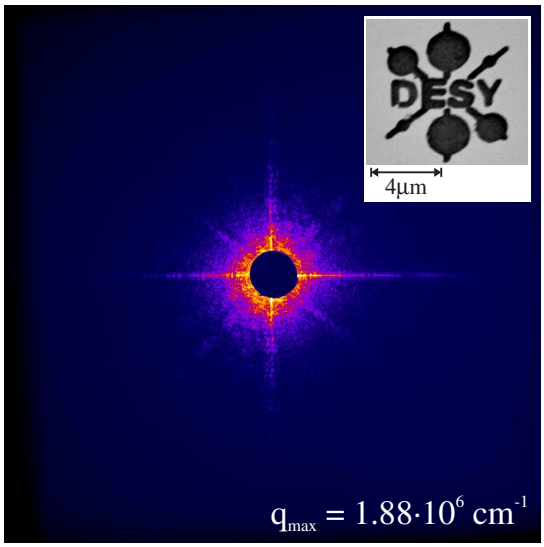

(c) Diffraction pattern of the DESY-logo sample.

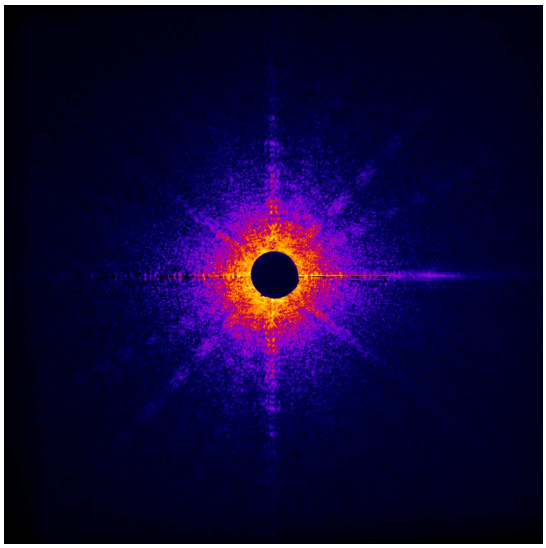

(d) Image (c) after background-correction.

Figure 4.4: (a) and (b): Comparison of the measured and calculated diffraction patterns for the Ettlinger-Tor sample with a size of 5 µm at 10 keV photon energy. The maximum scattering vector is given by $q_{\max} = 1.88 \cdot 10^6\,\mathrm{cm}^{-1}$.
(c) and (d): Diffraction pattern of a sample with the shape of the DESY-logo measured at 10 keV photon energy. Its size was 10 µm and the thickness of the gold layer was also 150 nm.

measured diffraction pattern can be approximately corrected for this background by subtracting a flat image of the x-ray beam. In order to measure this image the sample is removed and a diffraction pattern of only the empty beam with all slits included in the beam path is recorded. An example of a such a background corrected diffraction pattern is presented in Fig. 4.4(a).

It can be seen in the experimental diffraction pattern that we could measure a scattering signal up to the edge of the detector. In this geometry of sample-detector distance $L = 3.37\,\mathrm{m}$ the maximum scattering angle is given by $\vartheta_{\max} = 3.71 \cdot 10^{-3}\,\mathrm{rad}$. This corresponds to a maximum scattering vector of $q_{\max} = 1.88 \cdot 10^{6}\,\mathrm{cm}^{-1}$ or a resolution in real space $d_{\min} \approx 33\,\mathrm{nm}$ at 10 keV photon energy.

The beating of the scattering signal along the horizontal direction in Fig. 4.4 a) is related to the three vertical bars of the sample. While the shortest distance between two maxima of intensity is determined by the distance between outer bars of the sample there are two further characteristic frequencies present which are related to the distance between the individual bars as well as the width of a single bar. The combination of the horizontal and the slightly inclined bar of the sample gives rise to a more complicated interference pattern in the vertical direction.
A qualitative comparison between the simulated and measured diffraction pattern reveals that the total number of photons necessary to produce the measured diffraction pattern shown in Fig. 4.4(a) is approximately $10^{10}\,\mathrm{photons}/(10\,\mu\mathrm{m})^2$. Taking into account the total exposure time of 2000 s a photon flux of $5 \cdot 10^{6}\,\mathrm{photons/s}/(10\,\mu\mathrm{m})^2$ can be derived. This value is in good agreement with measured values of the photon flux.

In Fig. 4.4 c) the result of a measurement on another sample (DESY-logo) recorded under the same experimental conditions is shown. The sample had the shape of the DESY-logo and its size was approximately 10 µm. In Fig. 4.4 d) the background-corrected diffraction pattern is presented.

Since in these measurements too much low resolution data were not measurable these diffraction patterns could not be used for the reconstruction of the real space structure. However, they are a good illustration of coherent diffraction patterns showing the relation between spatial frequencies of an object and its Fourier-representation.

4.1.4 Measurements on Euro-Sample

At 10 keV photon energy the loss of low-frequency data due to the beam-stop was quite large. For example, the beam-stop with 1 mm in diameter covered about six diffraction orders. For this reason, further experiments were performed at the photon energy of 7 keV and at the largest possible sample-detector distance of 4.2 m. In this geometric configuration the speckle size is 149 µm corresponding to approximately 7.5 pixels on the Princeton-CCD. The third sample used for measurements at beamline ID01 had the shape of the Euro-symbol (cf. SEM-image shown in the inset of Fig. 4.6). The lateral size of the sample was about 5 µm and the thickness of the gold layer was 150 nm.

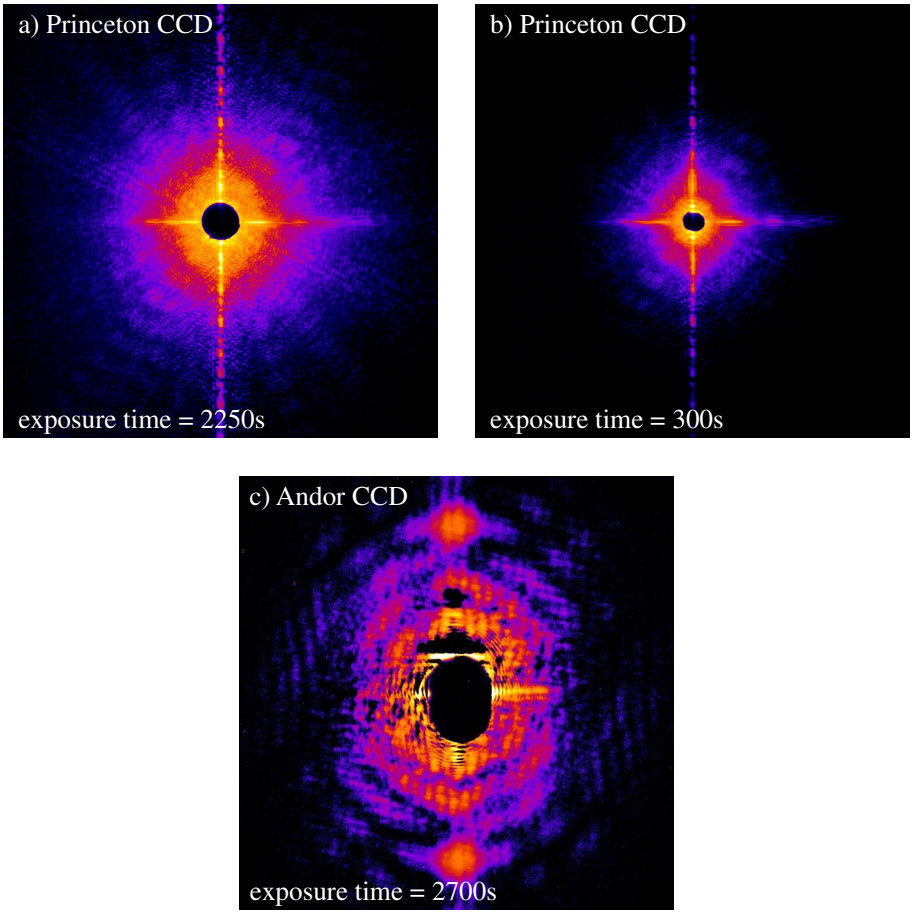

Figure 4.5: Background corrected diffraction patterns of the Euro-sample measured with different beam-stops at 7 keV photon energy. a) The beam-stop with a diameter of 2 mm allowed for longer exposures and a signal up to large q-values could be recorded. b) Diffraction pattern using the 1 mm beam-stop. The maximum q-value is $q_{\max} = 1.1 \cdot 10^6\,\mathrm{cm}^{-1}$ in image a) and b). c) The very inner part of the diffraction pattern was measured with the high-resolution detector. The size of the beam-stop was 0.3 mm. The diffraction pattern is background-corrected in order to enhance the visibility of fringes. The maximum scattering vector is $q_{\max} = 8.8 \cdot 10^4\,\mathrm{cm}^{-1}$.

In Fig. 4.5 an overview of diffraction patterns recorded from this sample is shown. The diffraction patterns were recorded using different beam-stops with diameters of 0.3 mm, 1 mm and 2 mm. For the larger beam-stops of 1 mm and 2 mm it was possible to use the Princeton CCD. A series of 1500 exposures was recorded for each of these beam-stops. The exposure time of a single image was 0.2 s and 1.5 s, respectively. In Fig. 4.5 a) and Fig. 4.5 b) the summed diffraction patterns are presented.

The central part of the diffraction pattern was recorded using the scintillator based high-resolution detector. In this experiment the objective with 4×-magnification was used. In Fig. 4.5 c) a background-corrected diffraction pattern is shown. The diffraction pattern is the sum of 30 individual images each recorded with an exposure time of 90 s. The effective pixel size of this detector is 3.25 µm and, therefore, one speckle spreads over approximately 50×50 pixels.
While the first diffraction order is contaminated by strong slit-scattering the second order is clearly visible. A certain modulation with finer frequency appears to be present on the speckle pattern indicating that most probably another object in form of a dust particle was located close to the sample. It can be noticed that around the beam-stop an even finer structure is imprinted on the diffraction pattern. It is the result of Fresnel-diffraction on the beam-stop which is positioned close to the detector.

These measurements clearly revealed that it is necessary to perform this kind of experiment with a directly illuminated CCD in order to be able to capture the low intensity signal at large q-values. Here, the Andor-CCD based on the imaging of the scintillator screen is not sensitive enough. However, it turned out to be very useful for the measurement of the central part of the diffraction pattern since it can withstand the direct x-ray beam.

In Fig. 4.6 the merged diffraction pattern is shown. The image of the Andor-CCD was binned in order to match the pixel size of the Princeton-CCD and individual diffraction patterns recorded with 0.3 mm- and 1 mm-beam-stop were multiplied with proper scaling factors in order to fit with the diffraction pattern with the 2 mm beam-stop.
The diffraction pattern is mainly characterized by the strong diffraction signal along the vertical direction which is related to the two horizontal bars and by circular shaped diffraction fringes due to the outer ring of the sample.

Another sample measured was a cluster of dielectric spheres used in the fabrication of photonic crystals. These nano-structures have a periodic dependence of the refractive index with a period adapted to the wavelength of visible light. This design gives rise to the creation of a band gap in the visible spectrum which is important for various technological applications like LED's or optical fibers. In Fig. 4.7 the diffraction pattern of a fragment of such a photonic crystal is shown. The dielectric spheres have a diameter of 670 nm.

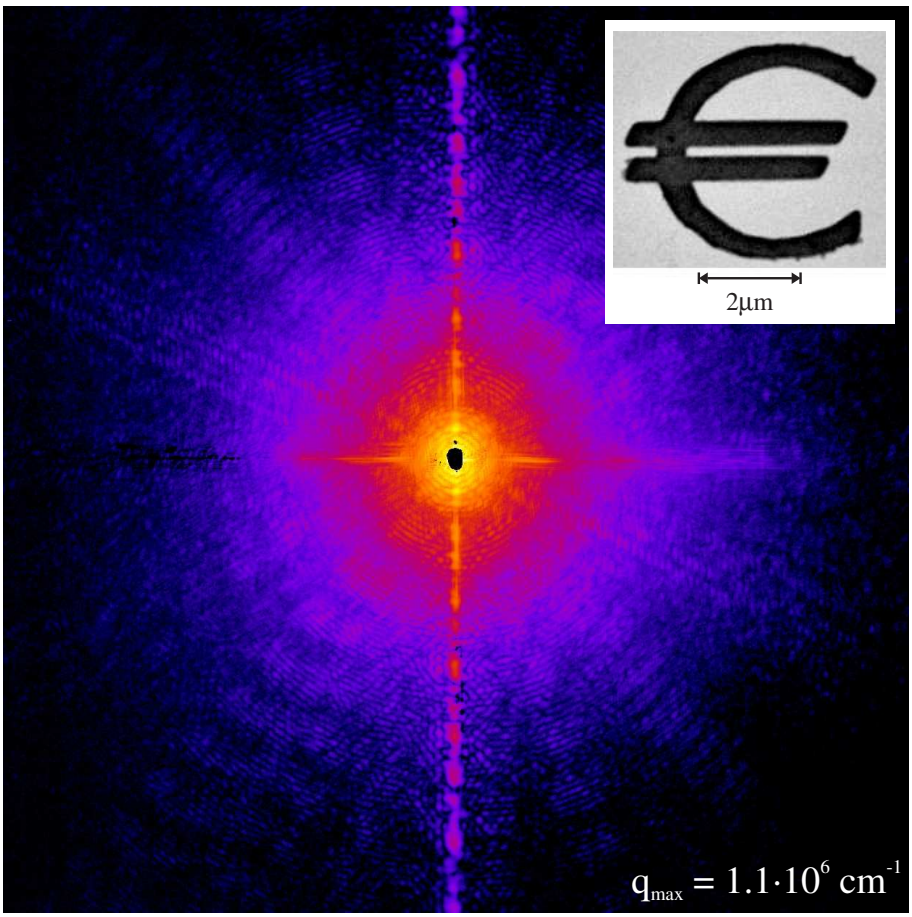

Figure 4.6: Diffraction pattern of the Euro-sample. The size of the sample is 5 µm and the thickness of the gold layer is 150 nm. In the inset the corresponding SEM-image is shown. The diffraction pattern is the result of a superposition of the diffraction patterns measured with the 0.3 mm-, 1 mm- and 2 mm-beam-stop.

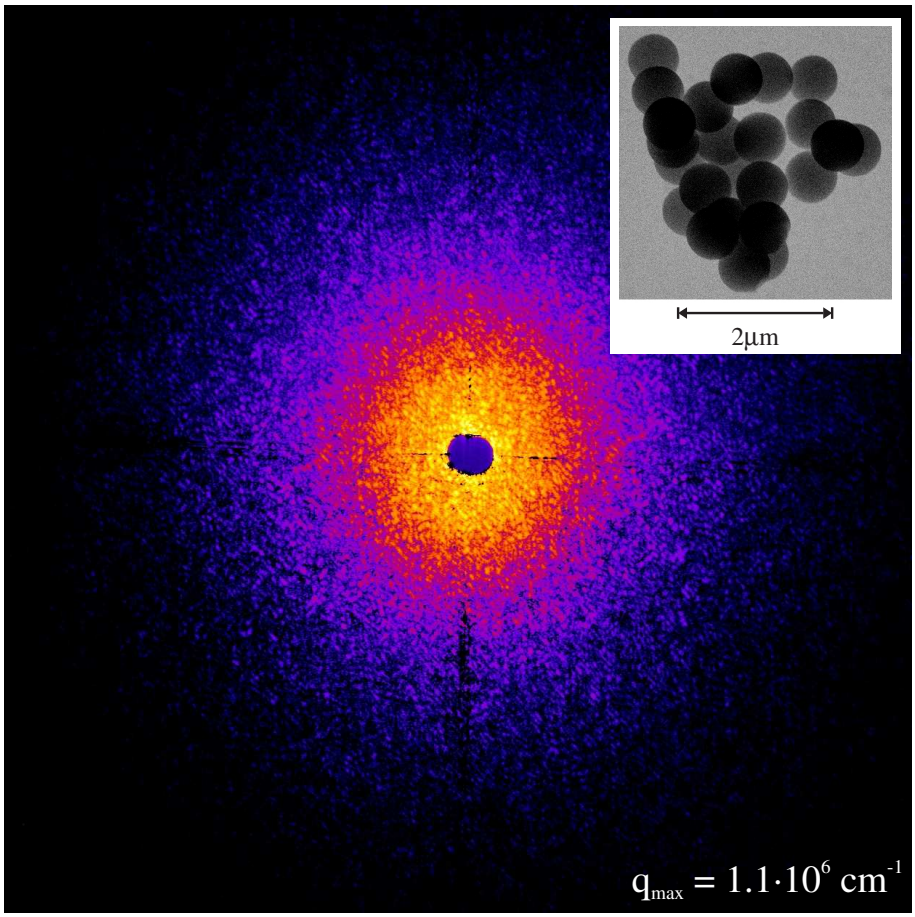

Figure 4.7: Diffraction pattern of a fragment of a photonic crystal.

The reconstruction of the exit wave field has only been possible for the measurements of the Euro-shaped sample. In this case the loss of low-resolution data was less severe. Nevertheless, a certain degree of smearing of the diffraction pattern can be observed which has to be corrected before the reconstruction. Some reconstruction results obtained from this diffraction pattern will be presented in Sec. 6.1.

In the following experimental results of another series of measurements carried out at beamline ID10C will be presented. The diffraction patterns were recorded with the same direct-illuminated CCD (PI-SX 1300). However, the high-resolution detector was not used to measure the central part of the diffraction pattern but was utilized for measurements of the incoming wave field at the sample position. In the experiment at ID10C our vacuum chamber (cf. Chap. 3) was used.

4.2 Measurements at ID10C, Troïka III (ESRF)

Since ID10 is a high-beta source the transverse coherence length in horizontal direction is not sufficiently large for CXDI-experiments. Nevertheless, a secondary source can be created by closing a pair of slits almost 18 m in front of the sample to an opening size of $50 \times 50\,\mu m^2$. This produces a lateral coherence length of 17 µm at the sample position for a photon energy of 8 keV. In Fig. 4.8 a schematic drawing of the beamline layout including the last optical components at ID10C is presented.

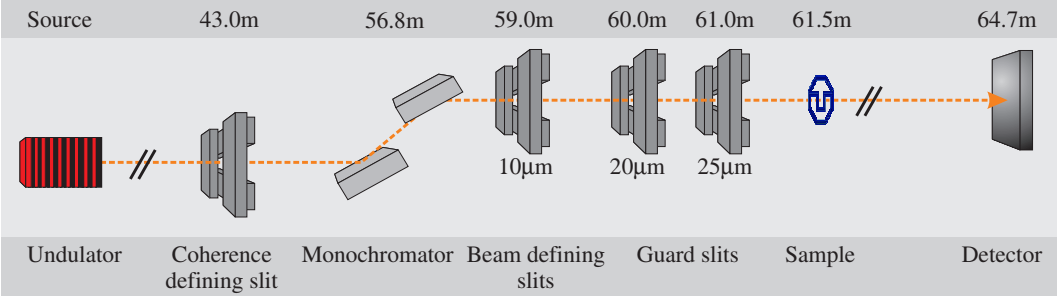

Figure 4.8: ID10C (Troïka III), arrangement of the last optical components.

The samples were positioned 2.5 m after the beam-defining slit and the distance between sample and detector was 3.16 m. Three pairs of slits were introduced after the monochromator to define a $(10 \times 10)\,\mu m^2$ x-ray beam. Two guard slits with especially polished Tantalum-blades were used to clean the beam from the scattering of the beam-defining slits.

4.2.1 Measurements on Lithographically Prepared Gold-Samples

Similarly to the experiment at ID01 first measurements were carried out on different lithographically prepared gold-structures. They were sputter-deposited on a Si_3N_4-membrane and their size was approximately 3 µm with a thickness of the gold-layer of 150 nm. Our setup allowed for the use of three different beam-stops with a diameter of 0.5 mm, 1.0 mm, and 2.0 mm.
At the photon energy of 7.98 keV the speckle size is given by $\Delta x_s = \lambda L/D = 163\,\mu m$, where following parameters of distance between sample and detector $L = 3.16\,m$, the size of the sample $D = 3\,\mu m$ and $\lambda = 1.55\,Å$ were used. That means that our smallest beam-stop covered about two speckles in the center of the diffraction pattern.

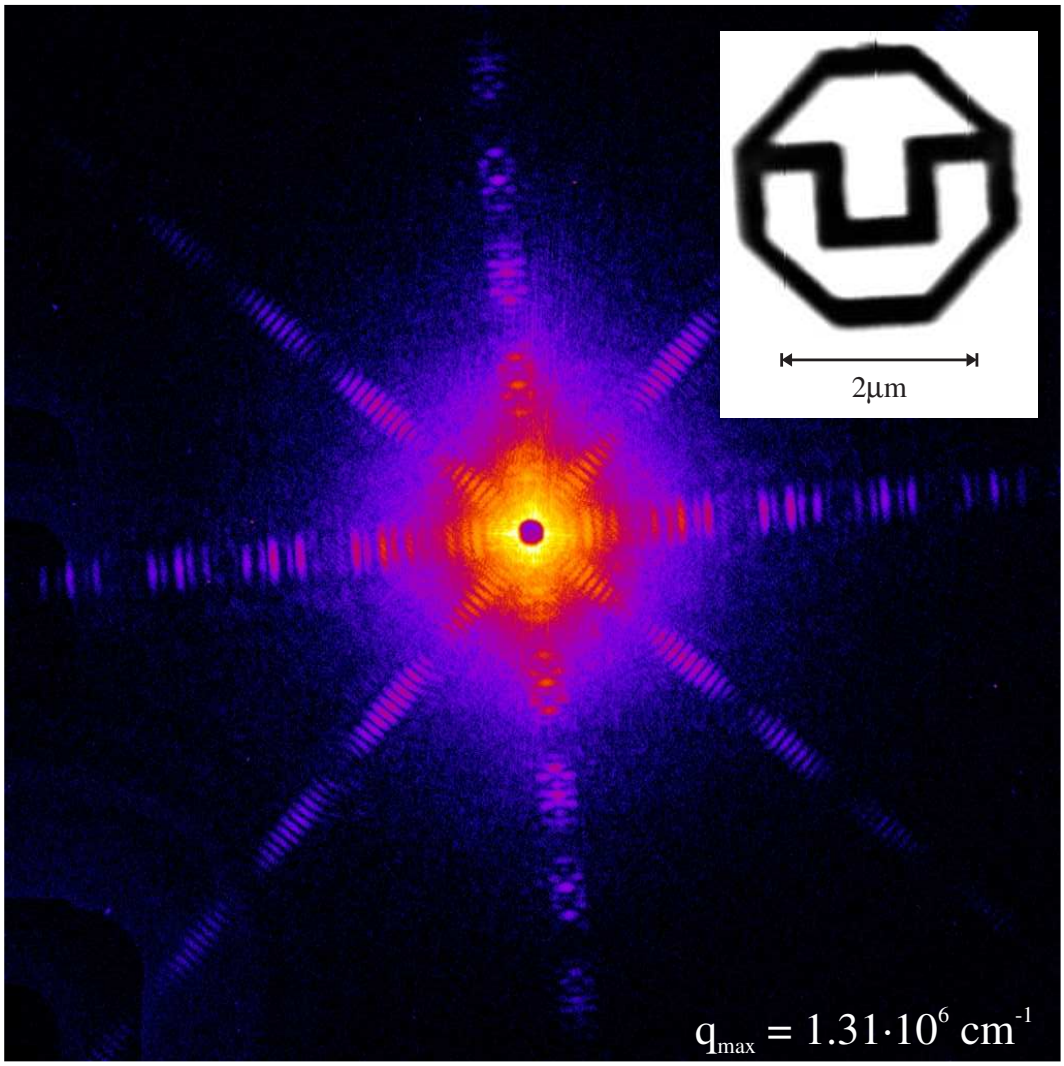

Figure 4.9: Diffraction pattern of the TU-Dresden-logo-sample.

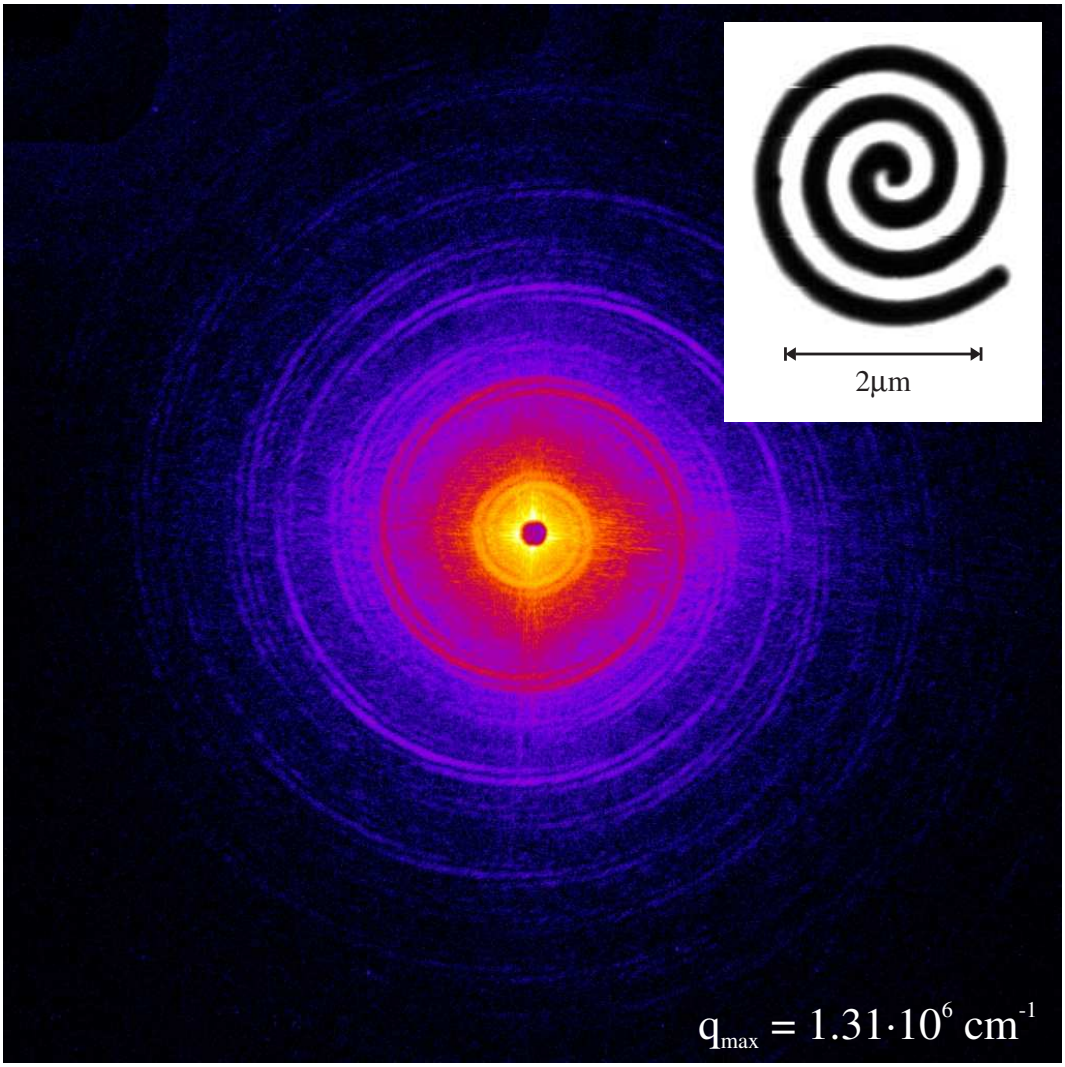

Figure 4.10: Diffraction pattern of a spiral-shaped sample.

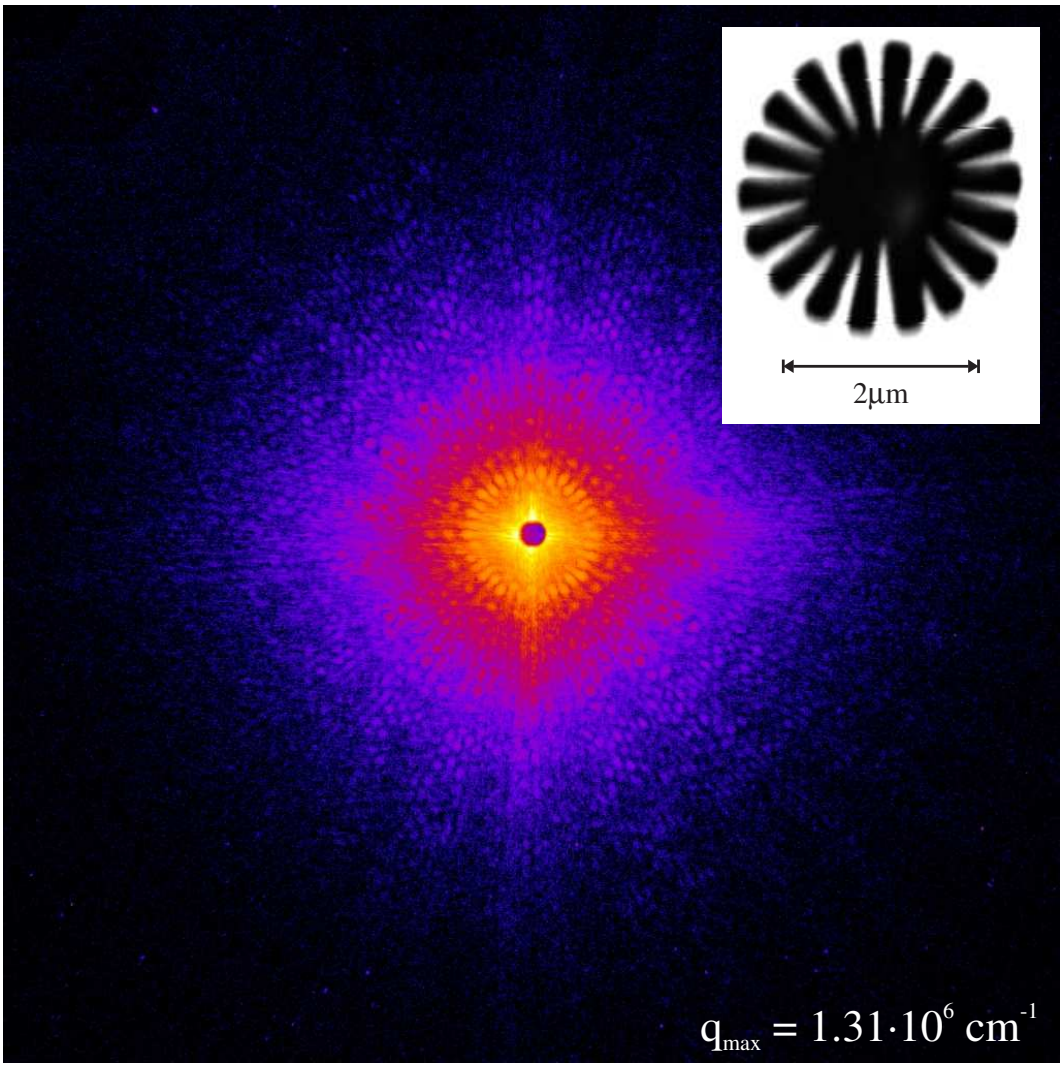

Figure 4.11: Diffraction pattern of the Siemens-star-sample.

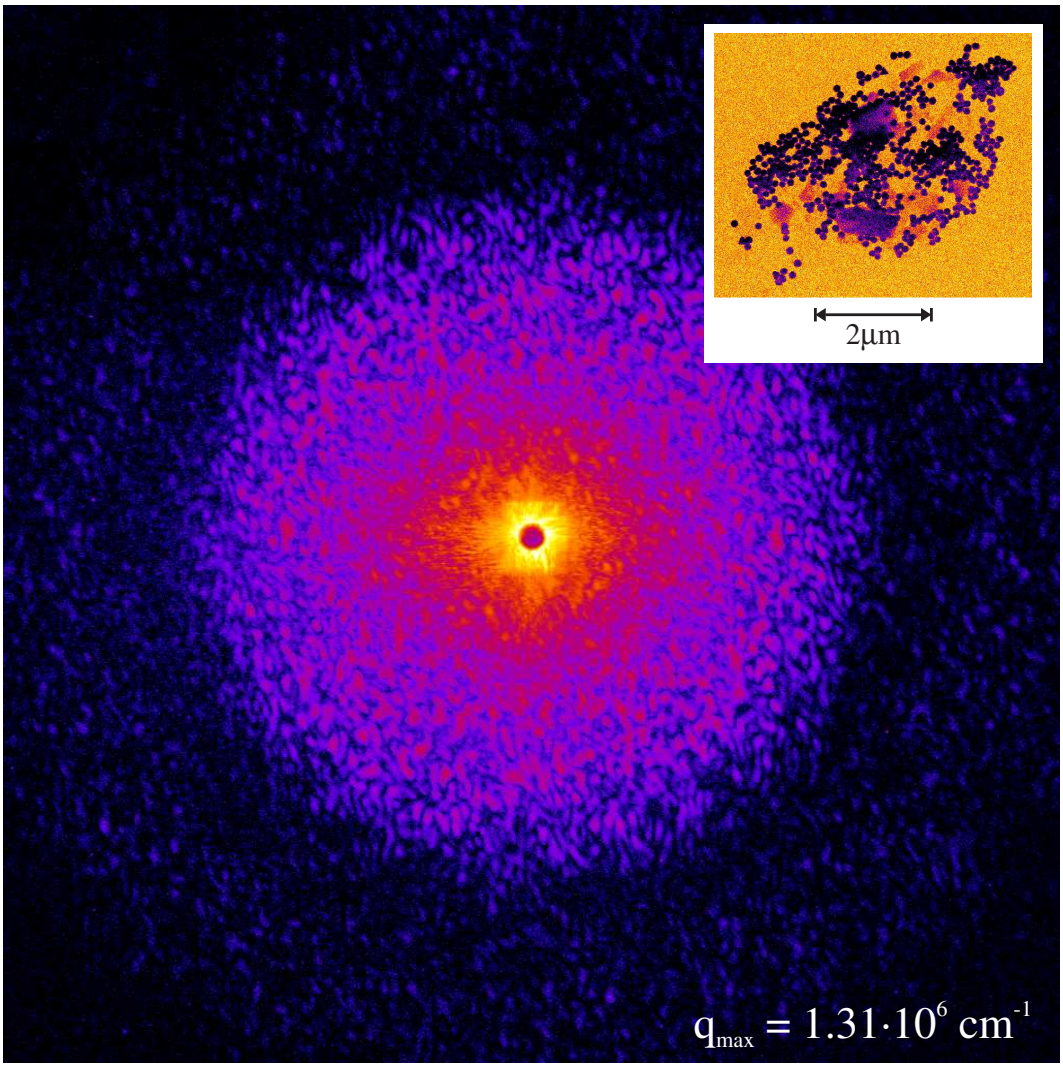

Figure 4.12: Diffraction pattern of the sample with cluster of gold spheres.

In Figs. 4.9, 4.10 and 4.11 the diffraction patterns of three different samples are shown. The first sample resembles the TU-Dresden logo. Due to its parallel bars photons are preferentially scattered in four directions. The diffraction patterns of the other samples like the spiral and the Siemens-star (Fig. 4.10 and Fig. 4.11) have less pronounced features at large q-values due to their round shape. In these cases, the scattered intensity is spread over the whole solid angle of 2π. The decrease in intensity towards large q-values is especially large in the diffraction pattern of the Siemens-star since the object has less fine structures.

The diffraction pattern presented in Fig. 4.9 is the sum of a series of exposures using the different beam-stops available. In detail, 100 images with 25 s exposure time using the 2 mm beam-stop, 1000 images of 3.5 s exposure time with the 1 mm beam-stop and further 1000 images of 0.5 s exposure time for the 0.5 mm beam-stop were recorded and summed up. Not counting the readout time of the CCD, the total exposure time is about 1 hour for each diffraction pattern shown. A similar measuring procedure with slightly different exposure times was applied in the measurement of the other samples.
Especially at low q-values a certain amount of background signal related to scattering at the slits and background scattering from the Si_3N_4-membrane is present (cf. Fig. 4.13). As will be shown in Chap. 6 the smearing and partial loss of low frequency information makes the reconstruction of the object more difficult.

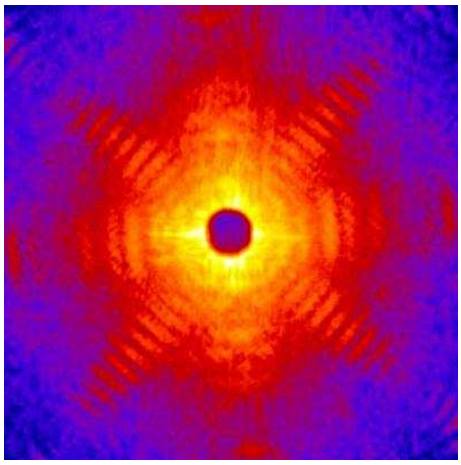

Figure 4.13: Detail of the central part of the diffraction pattern shown in Fig. 4.9. The background signal is related to scattering on optical components upstream and to scattering from the Si_3N_4-membrane.

In order to characterize the coherence properties of the x-ray beam the measured data are compared to simulated data. In Fig. 4.14(b) line profiles which are extracted from the measured diffraction pattern (Fig. 4.9) and simulated data (Fig. 4.14(a)) are shown. The position of the line profile that was used for this analysis is indicated by a white dotted line in Fig. 4.14(a). In this area of the diffraction pattern the visibility of the

interference fringes is high and only a small reduction of contrast can be noticed. A qualitative comparison reveals that the reduction of visibility is best reproduced if the simulated diffraction pattern is convolved with a gaussian with full width at half maximum (FWHM) of 2 pixels (compare the blue dotted line in Fig. 4.14(b)). The smearing of the diffraction pattern can be interpreted in terms of a larger effective source size and a short calculation provides a transverse coherence length of 8.1 µm at the sample position. The reduced transverse coherence length is related to different optical components upstream the sample.
The contrast in visibility decreases towards the central part of the diffraction due to the enhanced background signal in that area.

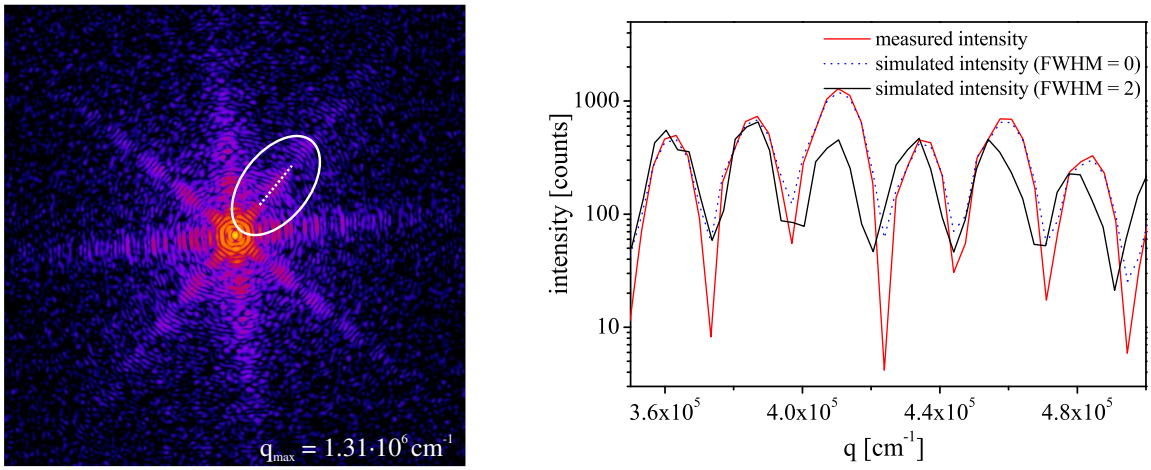

(a) Simulated diffraction pattern **(b)** Line profiles

Figure 4.14: The comparison between simulated and measured data for the TU-Dresden logo reveals a reduction in fringe visibility that corresponds to a convolution of the simulated diffraction pattern (a) with a Gaussian of 2 pixels FWHM. The position of the extracted line profile is indicated in Fig. 4.14(a).

The next sample measured at the beamline ID10C was a cluster of gold spheres with a lateral extension of about 3.5 µm. The preparation of the sample was performed by putting a drop of a solvent containing the gold-spheres on the Si_3N_4-membrane and let it evaporate. The gold spheres tend to create clusters on the Si_3N_4-membrane and a suitable one is selected with the help of a scanning electron microscope. In Fig. 4.12 the result of the measurement is shown. The form-factor of the gold spheres can well be recognized. The first minimum of the Airy-pattern is given by $\sin\vartheta/\lambda = 1.2/d$, if ϑ is the scattering angle and d is the size of the gold spheres [Spe03]. The value of the scattering angle can be deduced from the diffraction pattern and is given by $\vartheta \approx 2.4 \cdot 10^{-4}$ rad, i.e., the medium size of the gold spheres is approximately 78 nm.
Since the sample is coherently illuminated the smooth incoherent diffraction pattern, typical for small angle x-ray scattering on disordered systems, is broken up into speckles due to interference between different Au-spheres lying on the Si_3N_4-membrane. This

means that the position of an individual sphere is encoded in the particular speckle pattern.

4.3 Resolution Limits

The diffraction pattern of the gold-spheres presented in Fig. 4.12 was analyzed in detail with regard to photon flux. The maximum resolution in real space can be estimated from the number of photons per speckle at a certain q-shell.

Since a single photon creates a signal of approximately 800 ADC-units on the CCD the diffraction pattern was divided by this factor in order to have a quantitative measure of photons per pixel. In Fig. 4.15 the mean intensity as function of scattering vector $q = |\mathbf{q}|$ is shown in a double logarithmic plot. Typically, the intensity decrease is given by a power law behavior $I \propto q^{-\alpha}$ and the constant exponent α can be approximately determined by comparison with the experimental data. For the diffraction pattern analyzed here the power-spectrum does not appear straight due to the form-factor of the gold-spheres. Nevertheless, the linear regression is suitable to define the general tendency of the intensity decrease towards larger q-values.

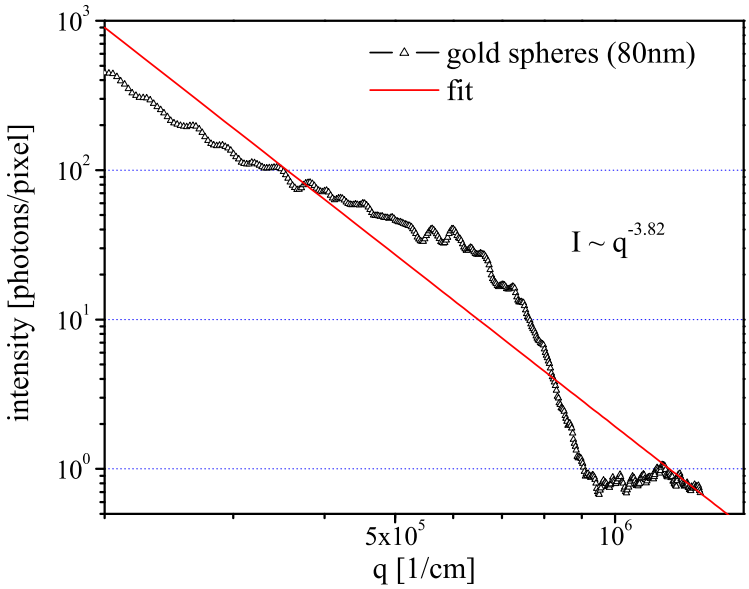

Figure 4.15: Mean intensity as function of q.

At this special oversampling ratio of 8 in each dimension the resolution limit can defined by the q-value where the intensity decrease reaches the value of about 0.1 photons per pixel which corresponds to approximately to 10 photons per speckle. From Fig. 4.15 it can be deduced that this condition is fulfilled up to the largest q-value shown which corresponds to a resolution in real space of $d_{\mathrm{res}} = 48\,\mathrm{nm}$ ($q_{\mathrm{max}} \approx 1.3 \cdot 10^6\,\mathrm{cm}^{-1}$). The

extrapolation using the found power law behavior reveals that the value of 0.1 photon per pixel is reached at about $q = 2.4 \cdot 10^6\,1/\text{cm}$. This means the maximum resolution in this measurement is approximately 25 nm

At ID10C the estimated photon flux was $(6 \pm 1.8) \cdot 10^{10}\,\text{photons/s/mm}^2$ and taking into account the total exposure time of 7500 s the whole diffraction pattern is the result of $(4.5 \pm 1.4) \cdot 10^{14}\,\text{incoming photons/mm}^2$.
Using this value the number of photons required to get a higher resolution of for example 5 Å can be estimated by another extrapolation of the power-law scaling. The experimental data reveal a constant exponent of $\alpha = -3.82 \pm 0.05$ and, therefore, an improvement in resolution to 5 Å would require about $10^{6.5}$ times more photons compared to this measurement. Hence, for this kind of sample a total number of approximately $1.5 \cdot 10^{21}\,\text{photons/mm}^2$ would be necessary to measure accurately diffraction data up to a resolution of 5 Å. It corresponds to $1.5 \cdot 10^{16}$ photons on the sample with a size of $3 \times 3\,\mu\text{m}^2$. This is a significant number that even upcoming sources like the XFEL can not deliver in a single pulse. In the case of the XFEL the number of photons per pulse is specified with approximately 10^{12} photons. The decrease of the atomic form factor towards larger q-values is still not considered in this estimation.
The connection between photon flux and achievable resolution will be investigated further in Sec. 5.2.

The power law behavior of diffracted intensity is discussed for different kinds of samples in a paper of Q. Shen et al. [She04].

4.4 Discussion

This chapter provides detailed information on the experimental conditions under which coherent diffraction experiments were carried out at beamlines ID01 and ID10C at the ESRF. One of the main experimental challenges was the correct measurement of the diffraction pattern covering a very large dynamic range of more than 1 million photons. The requirements on the detector can be summarized by small pixel size in order to fulfill the oversampling condition and single photon counting capability. For this reason it was necessary to use a directly illuminated CCD. Unfortunately, other detectors that are more adapted to the requirements of this measurement are currently not available. Our CCD had a pixel size of 20 µm and one photon is converted into a signal of about 800 ADC-units. Obviously, the disadvantage is that the directly illuminated CCD is saturated after a very short exposure time in case that the central part of the diffraction pattern is measured. Therefore, it is necessary to collect a series of single exposures and sum up the individual images to get the final diffraction pattern.

Another difficulty is the correct measurement of the central region of the diffraction pattern in the forward scattering geometry. Here, a substantial amount of background scattering due to slits, a contribution of third harmonic photons or scattering from the

support of the sample degrade the quality of the data. At beamline ID01 the very inner part of the diffraction pattern could be measured with a scintillator based high-resolution detector.

Different diffraction patterns were recorded from two-dimensional, lithographically prepared Au-samples with a lateral size ranging from 3 µm to 5 µm and a thickness of the gold layer of 150 nm. Gold ($Z = 79$) is a strong scatterer which turned out to be very convenient for these experiments using hard x rays. For certain samples it was possible to measure a scattering signal up to the edge of the detector which corresponds to a resolution of approximately 35 nm. The diffraction patterns of Sec. 4.2 were slightly cropped for illustration reasons.
The quantitative analysis concerning the scattered intensity from the cluster sample with Au-spheres revealed that for very high-resolution imaging a large incoming photon flux is necessary. The estimated number of $1.5 \cdot 10^{16}$ photons required to get a resolution of 5 Å for a two-dimensional Au-sample with a size of $3 \times 3\,\mu m^2$ is large and even upcoming x-ray sources can not provide this amount of photons per x-ray pulse.

5 Numerical Simulation of Coherent Diffraction and Reconstruction

Various questions and problems concerning the experimental setup and possible results were addressed in theoretical investigations by simulating the wave propagation of x rays including all optical components along the beam-path.
Two topics were of main interest for theoretical simulations. A first one was the simulation of wave propagation through different slit systems. This was related to the experimental observation that slit scattering contributes substantially to the measured diffraction pattern at low q-values. The aim was to find a geometrical arrangement of the slits that reduces slit scattering as much as possible.
A second part is focused on the resolution limit due to the limited number of diffracted photons and the influence of partial coherence, i.e., a reduced visibility of diffraction fringes, on the result of reconstructions.
Furthermore, some reconstruction results on simulated diffraction data using the genetic algorithm (cf. Sec. 2.7.6) are presented. Since it is a very different approach of phase retrieval these simulations were carried out with the goal to investigate the performance of the algorithm. In the last section the applicability of the ptychographic-method (cf. Sec. 2.7.5) is investigated in the case that the position of the illumination function is not perfectly known. It turns out that the performance of the algorithm depends strongly on the exact knowledge of the illumination function.

5.1 Slit scattering

One of the main difficulties in coherent x-ray diffraction imaging in the forward direction geometry is scattering from slits upstream. These slits are used to select a coherent portion of a partially coherent x-ray beam from a storage ring. In our experiments the typical size of the beam-defining slits is about $10 \times 10\,\mu\text{m}^2$ and they create under coherent illumination a defined diffraction pattern along the beam path. It is desirable that the sample will be positioned in the central cone, i.e., the zeroth order, of the diffraction pattern (cf. Fig. 5.2 a)) and ideally the sample should be sufficiently small that the curvature of the wavefront can be neglected over its size. Nevertheless, the scattering of the beam-defining slits gives a parasitic contribution to the diffraction pattern of the sample.
A commonly used method to suppress the scattered intensity of the first slits is the installation of a second pair of slits just in front of the sample. Albeit these blades block the diffracted intensity to larger scattering angles a certain amount of photons are scat-

tered on the blades of the guard slits producing a second source of parasitic scattering. Though, in this case the scattered intensity is significantly lower than without guard slits.
Nevertheless, even with this cleaning method the parasitic scattering due to slit scattering is still too large compared to the signal of the object – especially at low q-values. For this reason, a careful theoretical investigation was carried out with the aim to find the best positioning of the slit blades to define a small and clean x-ray beam. By using the mathematical basis described in Sec. 2.4 the numerical simulation of wave propagation along the beam-path through a series of slit pairs was implemented.

The following parameters were used in this simulation. A point source was generated at a distance of 42 m upstream the beam-defining slits. It is supposed to be monochromatic with a photon energy of 8 keV ($\lambda \approx 1.55$ Å) and defines the incoming wavefront at the position of the beam-defining slits. According to the properties of these slits the wave field is modified and propagated to the guard-slits at a certain distance downstream. In Fig. 5.2 a) the wave field at a position of 1 m after the beam-defining slits is shown. This was a typical distance between the beam-defining slits and the guard-slits used in experiments. The opening size of the slits was set to $10 \times 10\,\mu m^2$.

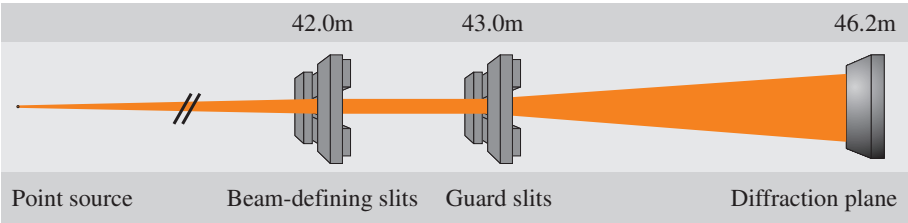

Figure 5.1: Schematic drawing of the setup used in simulations of wave propagation through a series of slit systems. The opening size of the guard-slits was varied in order to find the best geometrical configuration which is appropriate to reduce the contribution of slit-scattering as much as possible.

The slits were defined by the blade material, the size of the slit opening and a certain variation in sharpness of the blade edges. In this concrete case, the pair of slits was simulated by 10 mm thick Tungsten blades with an edge precision of 100 nm and a slit opening of 10 µm in each dimension. The wave field after the slits is propagated by a distance of 1 m to the position of the guard slits. These slits, which are used as cleaning slits to remove the scattered intensity of the first slits, block outer areas of the diffracted intensity. Afterwards, the truncated wave field is propagated by 3.2 m to the far-field. From that image an intensity profile along the horizontal is extracted. Depending on the opening size of the guard slits the scattered intensity changes considerably. The opening size of the guard slits was varied in this simulation between 32.5 µm and 98.3 µm.

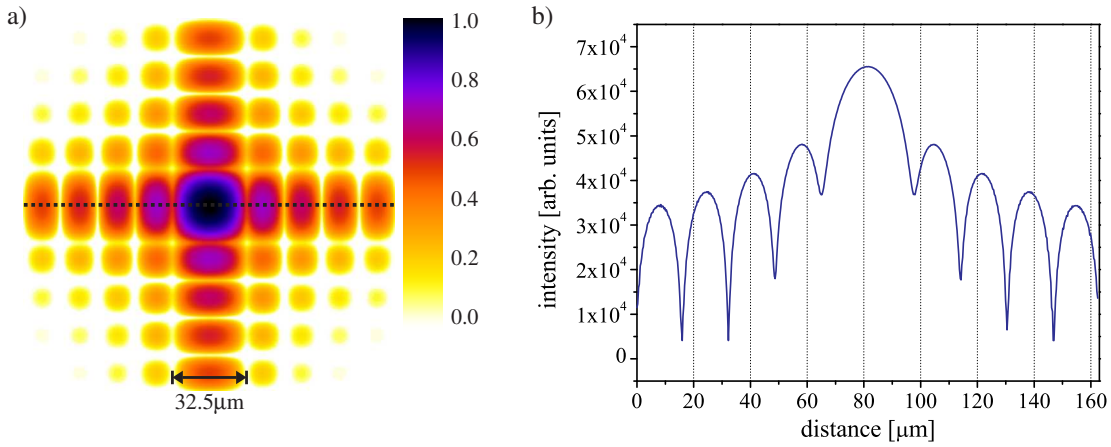

Figure 5.2: a) Wave field after a slit-pair with an opening size of $10 \times 10\,\mu\text{m}^2$ at a distance of 1 m and using a photon energy of $E = 8\,\text{keV}$. Logarithmic intensity color scale.
b) Logarithmic intensity profile along the dotted horizontal line indicated in image a).

Due to the relatively large opening of the guard slits of 46.5 µm the periodicity of intensity variations in the diffraction plane is small (cf. Fig. 5.3 a)). In this case the edges of the guard-slit blades intersect with the first maximum of the diffraction pattern (cf. Fig. 5.2 a)). In order to get a quantitative measure of the diffracted intensity related to the slit scattering of the guard slits the line profiles similar to the one presented in Fig. 5.3 a) were fitted with a function of the form $a \cdot q^{-b}$ for different opening sizes of the guard slits.

In Fig. 5.3 b) an overview of fit curves obtained from the diffraction patterns related to different sizes of the guard slits is presented. It clearly shows that the blades need to be positioned in a way that they cut in the minima of the diffraction pattern of the beam-defining aperture. Nevertheless, the first minimum beside the central peak is not the best position since the propagation distance of 1 m from the beam-defining aperture to the guard slit is still at the limit to the Fraunhofer-regime, i.e., $d_F = 2D^2/\lambda = 2 \cdot (10^{-5}\,\text{m})^2/1.55 \cdot 10^{-10}\,\text{m} \approx 1.3\,\text{m}$. Therefore, the intensity is still relatively large in the first minimum (cf. Fig. 5.2 b)).

The diagram presented in Fig. 5.3 a) corresponds to the red curve in Fig. 5.3 b) showing the highest scattered intensity. In comparison, the positioning of the slit-blades into the second minima, i.e., a slit opening of 65.2 µm, reduces the amount of slit scattering by more than one order of magnitude. Compare the green curve in Fig. 5.3 b).

These theoretical results were confirmed in the experiment at ID10C (ESRF). In Fig. 5.4 the measured Fresnel diffraction pattern from the beam defining slits at the sample position, i.e., about 1 m downstream of the beam-defining slits, is shown.

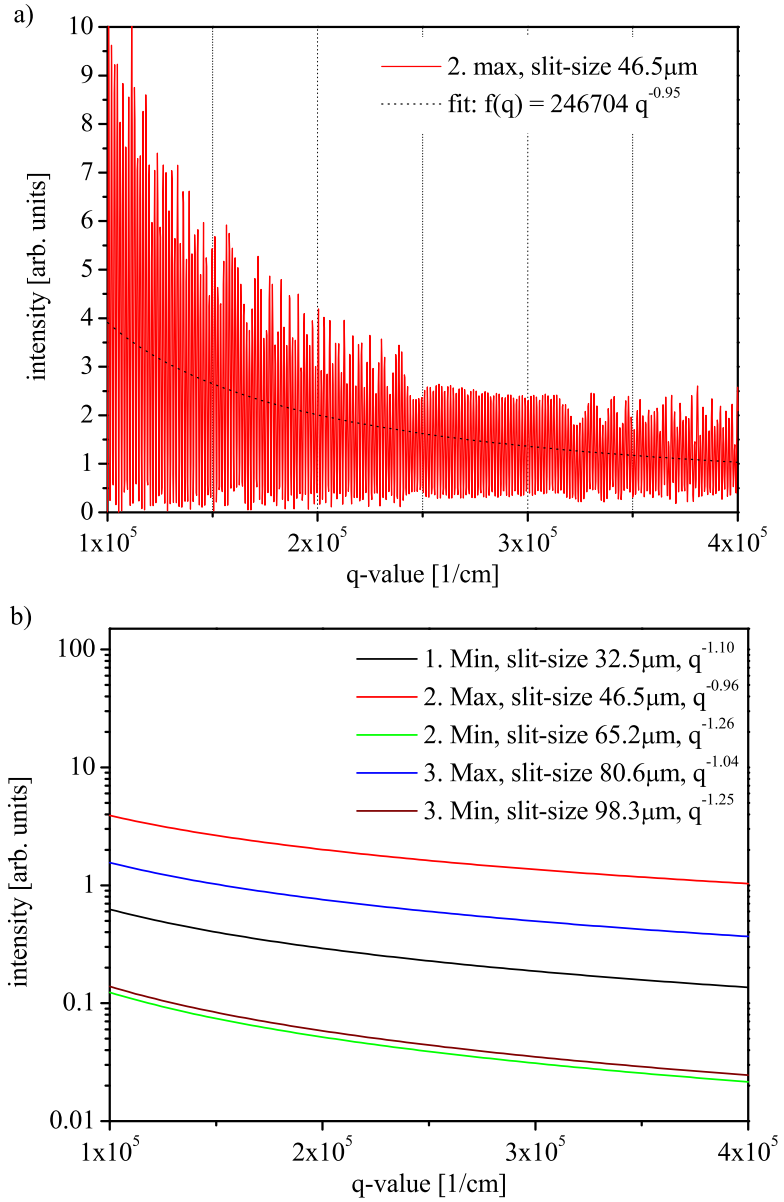

Figure 5.3: a) Line scan along the horizontal direction of the diffraction pattern related to the guard slits at a distance of 3.2 m downstream. b) Line profiles along the horizontal direction showing the dependency of slit scattering for different openings of the guard slit. The positioning of the blades turned out to be very sensitive during experiments. The simulation proves that in this geometry it is convenient to position the edges of the slit blades into the minima of the diffraction pattern from the beam-defining slit – especially the second or third minimum.

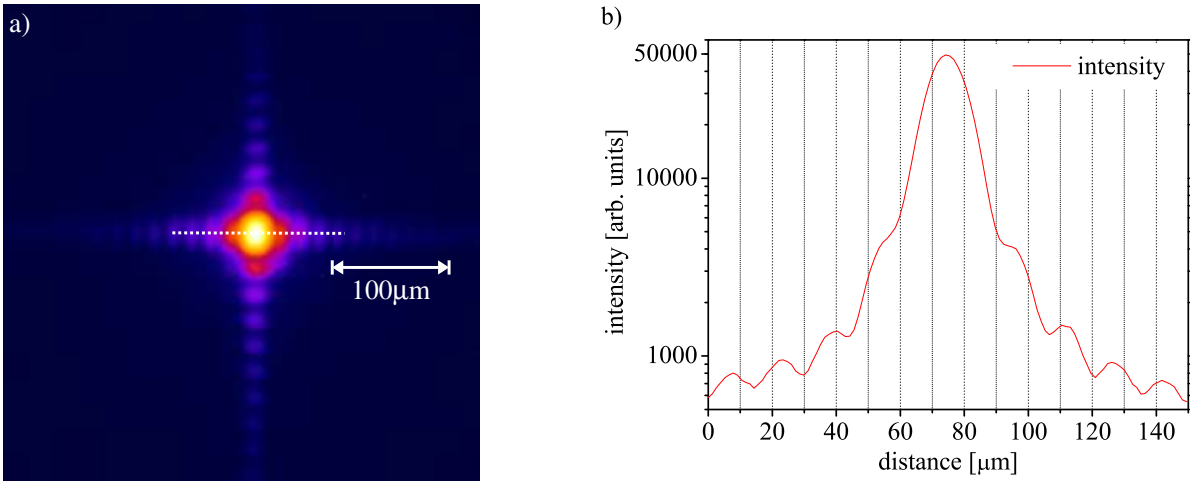

Figure 5.4: a) Diffraction pattern of the beam-defining slits at a distance of approximately 1 m downstream measured at the beamline ID10C with the high-resolution camera close to the sample position. b) Line profile along the dotted white line in Fig. a).

The diffraction fringes are clearly visible showing a lateral period of approximately 16 µm like in the simulation. However, the visibility of diffraction fringes is quite reduced compared to the simulated pattern shown in Fig. 5.2. The high-resolution x-ray detector described in Sec. 3.2.3 is a very convenient tool to observe changes of the illumination at the sample position and can be used to control the position of the guard slit-blades. In this way, it is possible to set the slit blades into the minima of the diffraction pattern with micrometer-accuracy.

5.1.1 Silicon-Corners As Guard-Apertures

The use of silicon-corners to block the scattering of the beam-defining aperture has been mentioned in a number of publications [Mia03a, Mia03b, Mia05, Mia06]. The idea is to position a Si-window with beveled edges perpendicular to the x-ray beam just in front of the sample. The distance between the beam defining aperture and the corner is referred to be about 0.5 m. Photons that are scattered at the beam-defining aperture are substantially absorbed by the Si-corner, while a lower amount of photons are scattered once again on the corner blade. The inclination of the wedge creates a certain gradient in phase shift of the transmitted wave field and, similarly to the working principle of a lens, the photons are refracted from their direction of propagation. Due to the fact that the refractive index of the material is smaller than unity for x rays the deflection of the x-ray beam is away from the wedge (cf. Fig. 5.5).

It is mentioned in these publications that 3/4 of the diffraction pattern can be cleaned from the scattering of the beam-defining aperture whereas 1/4 needs to be covered by an extended beam-stop. This seems to be valid for energies lower than 5 keV if the sample

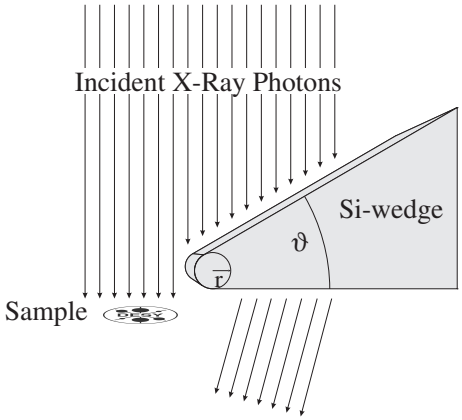

Figure 5.5: Schematic drawing of a Si-wedge used to block the scattered intensity of the beam-defining slit. It is included in the simulation as an optical element and is defined by its material properties, the inclination ϑ and a value of a radius r corresponding to a certain rounding of the edge.

is positioned in the corner of a Si-window.
This idea was pursued also during this work, but for the higher photon energy of 8 keV. Therefore, beside experimental testing different numerical calculations were carried out in order to explore the applicability of this method at higher photon energies.

The numerical implementation of the Si-wedge is done by calculating the transmission function of the wedge knowing the thickness of the material in a certain pixel. A rounded edge can be included by defining a value for the radius r. For further distances from the edge the thickness of the material is linearly increasing with a gradient defined by the angle ϑ. A sharp wedge can be introduced by setting the radius r to zero. In Fig. 5.5 a sectional drawing of the corner blade is shown. In the following the properties of such a wedge with regard to refraction and absorption will be discussed.

5.1.2 Refractive Power of a Si-Wedge

The strength of refraction has been studied theoretically by illuminating the wedge with an x-ray beam of 8 keV photon energy. The propagation of the wave field is implemented as follows. The point source at a distance of 60 m illuminates directly the Si-wedge. Afterwards, at a distance of 1 mm a test-sample (Euro-symbol) with a size of 5 µm and a thickness of 300 nm is introduced. From the transmission function of the object (cf. Fig. 5.6 (a), (c), (e)) the diffraction pattern is calculated at a distance of 3.2 m (cf. Fig. 5.6 (b), (d), (f)).

As the inclination of the wedge increases the phase gradient due to the Si-wedge becomes larger which leads to an enhancement of refraction. In Fig. 5.6 the results of the simulations with different ϑ-values of 75°, 85° and 89° are shown. Further parameters

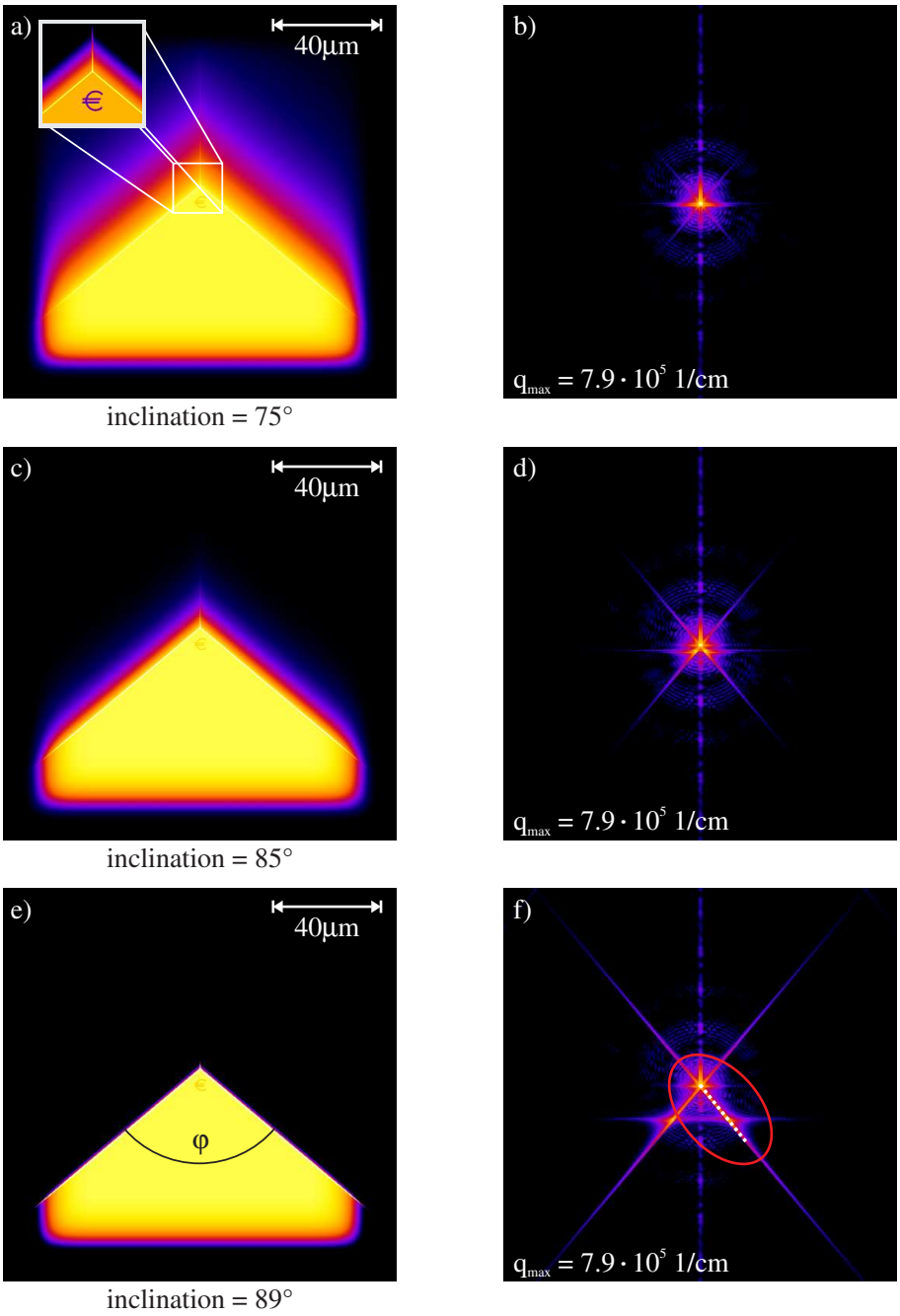

Figure 5.6: In Figs. (a), (c), (e) the intensity of the wave field after the sample at a distance of 1 mm behind the corner is shown. The total thickness of the corner is 0.4 mm and the opening angle $\varphi = 100°$. The inclination of the wedge is indicated below each image. The diffraction patterns are calculated for a distance of 3.2 m after the sample (cf. Figs. (b), (d) and (f)) showing an increasing refraction effect as the inclination angle ϑ of the wedge becomes larger.

were the thickness of the Si-wafer $t = 0.4\,\mathrm{mm}$, $r = 0.\,\mathrm{mm}$ (sharp wedge), and the opening angle of the wedge of $\varphi = 100°$ (indicated in Fig. 5.6 (e)).

At 8 keV photon energy and with an inclination of 75° refraction effects due to the Si-wedge are very low as can be recognized in Fig. 5.6 b). The scattered intensity is distributed along a line perpendicular to the wedge and a slight refraction effect can only be noticed in the very central part of the diffraction pattern. However, the diffraction pattern changes considerably in case of an inclination of 89°. Interestingly, the photons are not only scattered towards one direction but, as it is assumed for a sharp edge, in both directions. Nevertheless, depending on the angle of inclination there exists a preferred scattering direction.

In Fig. 5.7 a diagram illustrating the effect of refraction is shown. Line profiles are taken along the dotted white line that is highlighted in Fig. 5.6 (f) by a red ellipse for each of the diffraction patterns presented in Figs. 5.6 (b), (d), (f). By increasing the slope of the wedge the edge becomes sharper and the overall scattering signal increases strongly. Additionally, a second maximum of intensity is formed at a defined q-value due to refraction. The q-position of this maximum depends on the gradient of the phase shift.

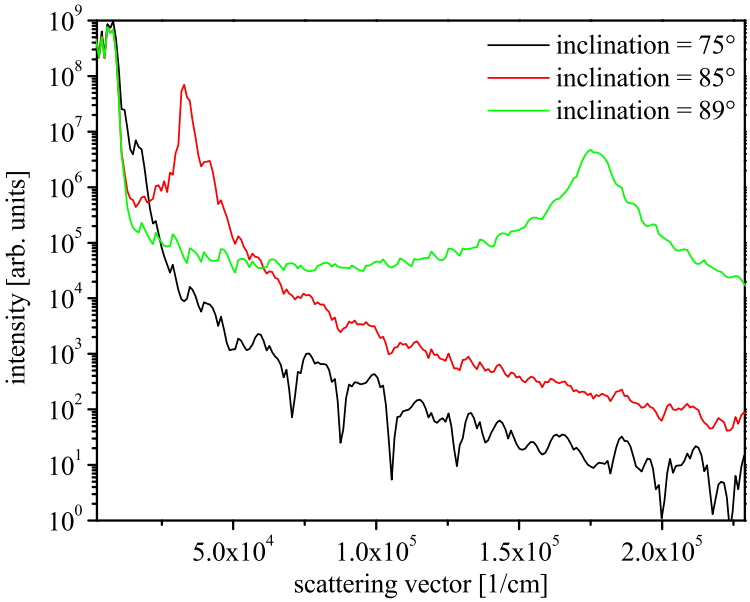

Figure 5.7: Line profiles along the white dotted line indicated in Fig. 5.6 (f) for different inclination angles of 75°, 85° and 89° are shown. With increasing inclination angle ϑ a second maximum arises due to an enhanced refraction effect from the Si-wedge.

This refraction effect can easily be reproduced by using Snellius-law:

$$n_1 \cdot \sin\alpha_1 = n_2 \cdot \sin\alpha_2, \tag{5.1}$$

where n_1 is the refractive index of medium 1, α_1 is the incident angle, measured from the normal of the surface, n_2 the index of refraction of medium 2 and α_2 the angle of refraction (cf. Fig. 5.8).

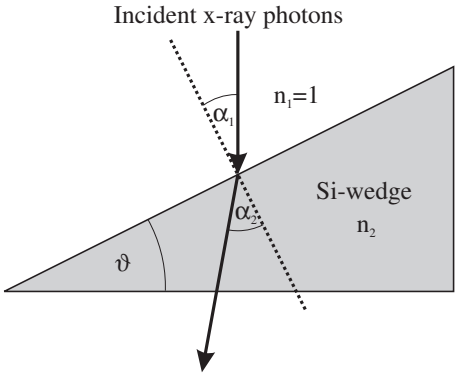

Figure 5.8: Schematic drawing of refraction on wedge.

Since the deviation of the angle of refraction α_2 from the angle of incidence α_1 is small for x rays the term $\sin\alpha_2$ can be approximated using the Taylor expansion:

$$\sin\alpha_2 = \sin\alpha_1 + \cos\alpha_1 \cdot \Delta\alpha + \ldots . \tag{5.2}$$

By inserting Eq. (5.2) into Eq. (5.1) and specifying the values of $n_1 = 1$ for vacuum and $n_2 = 1 - \delta$ the angular deviation due to refraction is given by

$$\Delta\alpha \approx \delta \cdot \tan\alpha_1. \tag{5.3}$$

For comparison the refraction angle obtained from the simulation and the calculation is summarized in Tab. 5.1, where $\delta_{\mathrm{Si}}(8\,\mathrm{keV}) = 7.67 \cdot 10^{-6}$ was introduced in the calculation of $\Delta\alpha$ using Snellius law. The simple calculation proves that the second maximum in the simulated diffraction patterns of Fig. 5.6 can be attributed to refraction at the Si-wedge.

angle of incidence	$\Delta\alpha$, simulation [rad]	$\Delta\alpha$, calculation (Snellius) [rad]
75°	$2.21 \cdot 10^{-5}$	$2.86 \cdot 10^{-5}$
85°	$8.77 \cdot 10^{-5}$	$8.09 \cdot 10^{-5}$
89°	$4.32 \cdot 10^{-4}$	$4.39 \cdot 10^{-4}$

Table 5.1: Comparison of refraction angles $\Delta\alpha$ as determined in the simulation and the calculation using Snellius-law.

Absorption effects on Silicon are also quite low at 8 keV photon energy. For example, a 10 µm thick Si-slab absorbs only 14 % of the photons, whereas at 5 keV the absorption is about 42 %.

Therefore, the success of the Si-wedge in experiments at 5 keV photon energy has to be attributed to the stronger absorption and refraction at lower photon energies. At 8 keV photon energy the effect of refraction as well as absorption on a Si-wedge are small and, therefore, such an edge is not suitable to clean the x-ray beam from slit-scattering. The effect of refraction becomes important not until the wedge is steep. But in this case, the usual scattering perpendicular to the edge strongly increases which is also undesired in the experiment. In the hard x-ray regime further technical developments are necessary to properly clean the x-ray beam in forward direction.

5.2 Photon Flux and Noise

Photon flux is a crucial factor for the method of lensless coherent diffractive imaging since, together with the scattering power of the sample, it finally limits the largest diffraction angle where a significant intensity can be recorded.
In this section the influence of incident photon flux on the result of a reconstruction is investigated using an "euro-shaped"-pattern with similar properties as the sample that was used in the experiment at beamline ID01 (cf. Sec. 4.1.4). The object has been assumed to be a thin gold layer with a thickness of 150 nm and a size of approximately 5 µm. Additionally, certain parts of the theoretical object were artificially modified in thickness with the aim to illustrate the influence of scattering power on the result of the reconstructed image. The photon energy was set in this simulation to 8 keV. In Fig. 5.9 the transmitted intensity after the sample is shown.

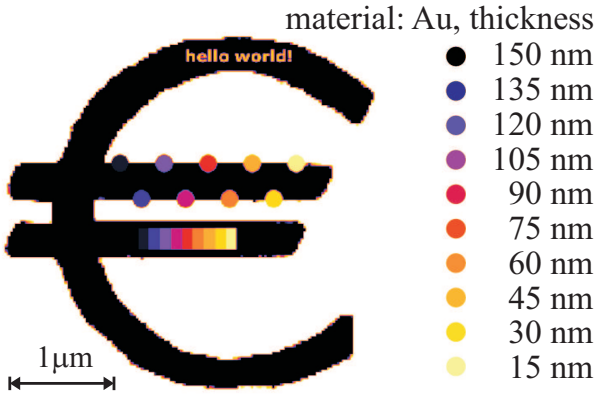

Figure 5.9: Transmitted intensity after the Au-sample with a size of 5 µm. The black color corresponds to strong absorption and a material thickness of 150 nm, whereas lighter colors indicate a gradually decreasing thickness of the material in steps of 10 %.

The transmission function of the object was calculated as described in Sec. 2.3.3. The maximum thickness of 150 nm that is associated with the black color produces a phase shift of $\Delta\varphi = -0.29$ rad. The maximum absorption is 6 %. Lighter colors ranging from blue over red to yellow illustrate a decreasing thickness of the material in steps of 10 %. This complex transmission function was used to calculate the diffraction pattern for different levels of incoming photon flux, cf. left images in Fig. 5.10. Photon flux is considered by multiplication of the transmission function with a real factor given by $A = \sqrt{I}$, where I is the intensity per pixel. In this case the pixel size in real space was assumed to be 15 nm. After propagation of the transmitted wave field to the Fraunhofer-regime a numerical Poisson-routine was used in order to take into account the statistical arrival of photons. Thus, the intensities of the field can only take integer values, i.e., for values very below unity the probability to measure a photon is small and, therefore, the intensity is most probably zero in these cases.

In the reconstruction attempts from these data the central part of the pattern was masked by a theoretical beam-stop with a diameter of 12 pixels. This part is recovered easily in the reconstruction with the shrink-wrap algorithm. The total incoming dose was varied between 10^{11} to 10^{15} photons/mm^2. In the left column of Fig. 5.10 three different diffraction patterns calculated for a total photon flux ranging from 10^{11} to 10^{13} photons/mm^2 are shown. These give about $3.6 \cdot 10^4$ to $3.6 \cdot 10^6$ diffracted photons outside the beam-stop area in Fig. 5.10 a) and Fig. 5.10 e), respectively.

The images on the right side of Fig. 5.10 are successful reconstructions using the noisy diffraction pattern on the left as input data. As expected, if the number of diffracted photons is small, i.e., only about 36 000 (cf. Fig. 5.10 a)), then the reconstructed image shows a very limited resolution. This is simply due to the fact that the amount of photons scattered to larger diffraction angles, i.e., the ones that are supplying information about the fine structure, is too small to adequately sample the fringes of the outer regions of the diffraction pattern. Therefore, only the global shape of the object can be recovered by the algorithm whereas all other internal structural information is blurred. Increasing the total number of photons by a factor of 10 (cf. Fig. 5.10 c)) essentially improves the quality of the reconstruction and the fine structure present in the initial image starts to become visible. But still, a certain degree of blurring is present in that image.

Increasing the dose further to 10^{13} photons/mm^2 shows clearly that now the fine structure of the sample becomes visible – essentially the "hello world"-letters as well as different thickness values of the material are well represented in the reconstruction. However, the contrast in the lower bar which should show a step-like behavior concerning the thickness of the material is not well recovered yet. The 10 %-contrast between different thickness-steps is only visible for dose-values equal to or larger than 10^{15} photons/mm^2 as will be shown in the following discussion concerning the resolution of the inverted images.

However, these reconstructions from simulated data prove that the influence of Poisson-noise only concerns the achievable resolution of the inverted image but does not introduce other artifacts in the reconstructed image.

Since for this sample the scattered intensity is not homogeneously distributed in all directions the evaluation of the resolution corresponding to a certain photon flux is not easily done. The analysis of the reconstructed image presented in Fig. 5.10 d) shows that the resolution deduced from a line profile may vary depending on the position where the line profile is taken. For illustration two different line profiles are chosen in Fig. 5.11 which should both exhibit a step-like behavior in contrast. The first one, named profile 1, is oriented in vertical direction overlapping the upper bar of the Euro-symbol. The second, profile 2, extends over the edge of the object along a diagonal direction (cf. Fig. 5.11).
In Fig. 5.12 the corresponding line profiles are shown. Due to the enhanced diffraction of the two bars of the Euro-sample along the vertical direction (cf. Fig. 5.10 c)), the edge of the bars (profile 1) appears sharper in the reconstruction result compared to the edge

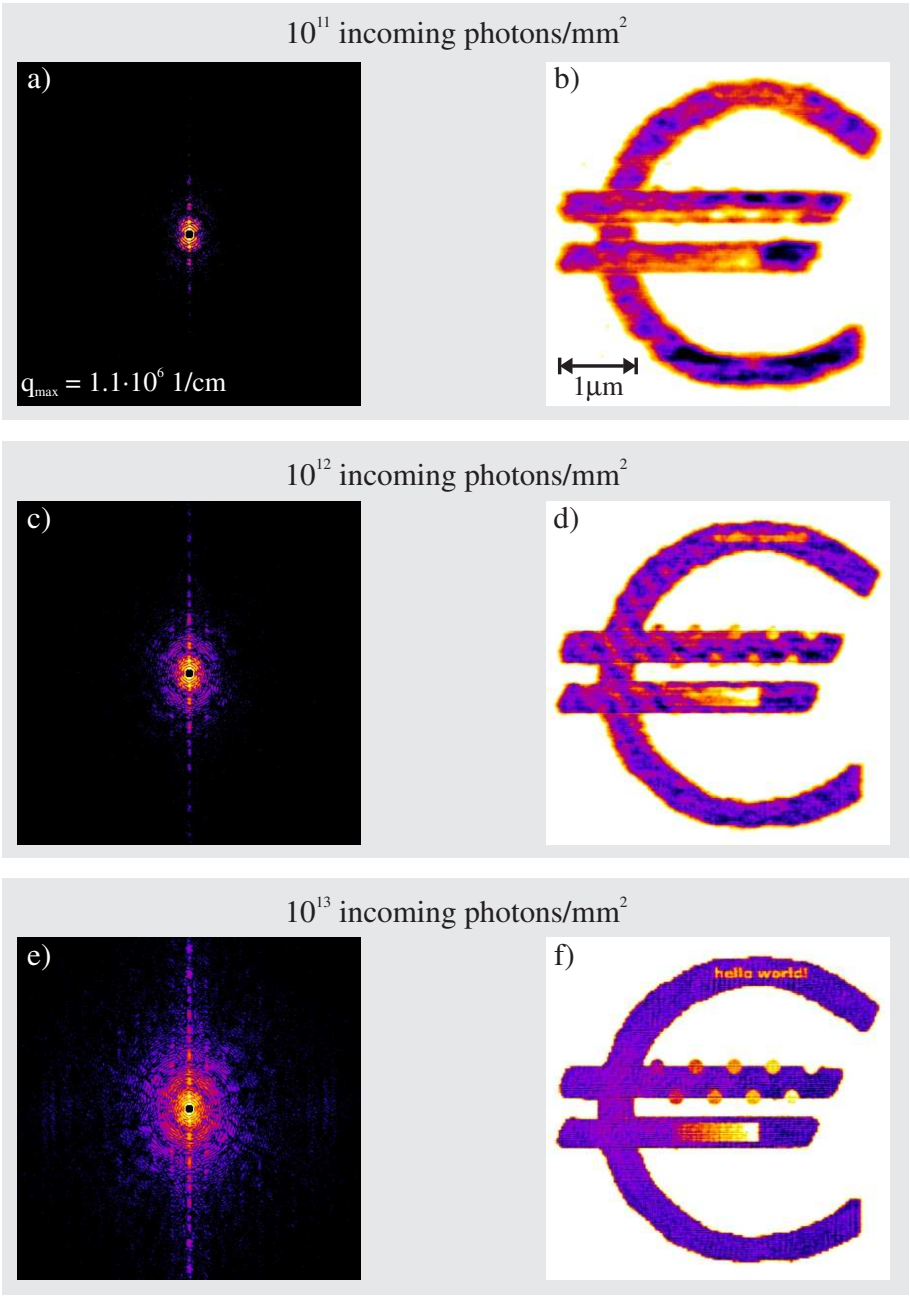

Figure 5.10: The figures on the right side, i.e., b), d), f), are the result of successful reconstruction from the diffraction pattern presented on the left side. The quality of the reconstruction considerably improves with increasing dose. The diffraction patterns to the left were produced using a numerical Poisson-routine taking into account the expected photon flux in each pixel of the diffraction pattern. The dose is indicated in each panel. For illustration reasons the total field of the diffraction pattern has been cropped to half the size of the original image in each dimension. The reconstruction was performed using the shrink-wrap algorithm (cf. Sec. 2.7.4).

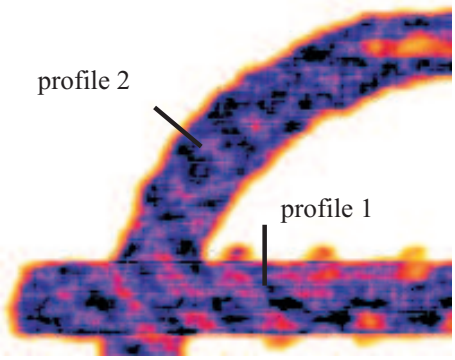

Figure 5.11: Section of the reconstructed image given in Fig. 5.10 d) for a dose of 10^{12} photons/mm^2. Line profiles were taken at the indicated positions in order to determine the resolution of the reconstructed image.

of the outer curved region of the sample (profile 2).

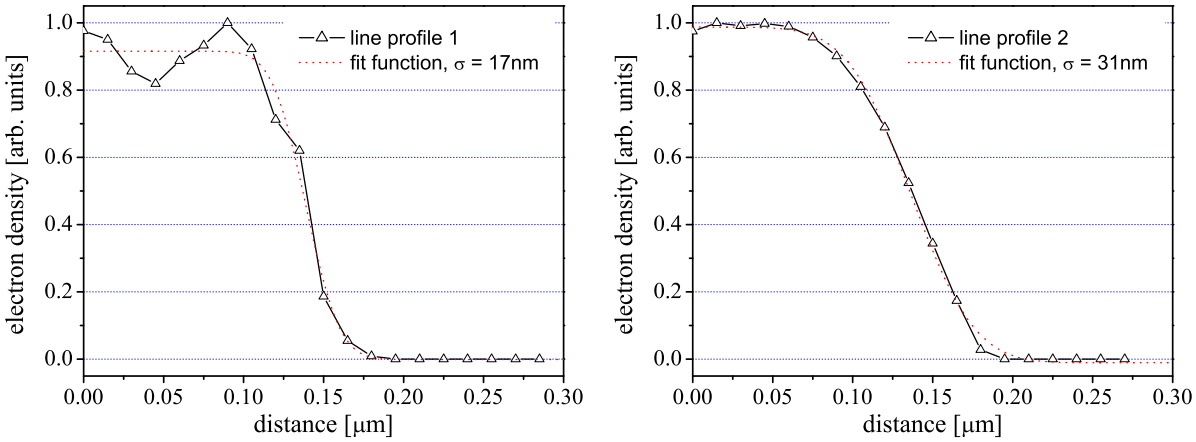

(a) profile 1 **(b)** profile 2

Figure 5.12: Density profiles along the lines indicated in Fig. 5.11.

The line profiles are presented in Fig. 5.12 a) and b) including the corresponding fitting curve $f(x) \propto \mathrm{erf}(-(x - x_0)/(\sqrt{2}\sigma))$. From the fitted σ-value the FWHM can be determined to 40 nm for profile 1 and 73 nm for profile 2, respectively. This difference is understandable since the diffraction signal in the vertical direction is much stronger than in any other one (cf. Fig. 5.10 c) which is due to the parallelism of the horizontal bars. For this reason the edge of these bars appears sharper in the reconstructed image as compared to the outer ring of the object.

The lower bar of the simulated Euro-shaped-object contains a rectangular region where the thickness of the material decreases in steps of 10% of the maximum thickness of 150 nm (cf. Fig. 5.9). By extracting lines profiles from the reconstructed images along

this horizontal gradient information on the resolution of internal features of the object can be deduced. The line profiles are plotted in Fig. 5.13. In order to enhance the visibility of the profiles an artificial offset of 0.2 and 0.1 was subtracted from the profiles corresponding to 10^{12} photons/mm^2 and 10^{14} photons/mm^2, respectively.

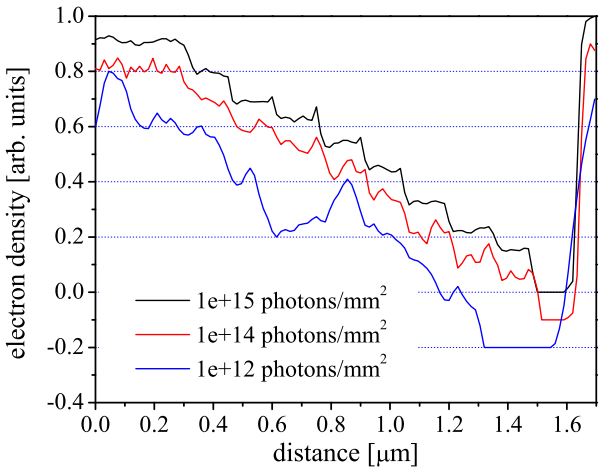

Figure 5.13: Line profiles along a horizontal line in the lower bar of the test sample were extracted from reconstructions based on different values of photon flux.

The reconstructed images do not reveal the step-like behavior of the thickness for a dose lower than 10^{15} photons/mm^2. Instead, for these dose values only a gradually decreasing electron density can be deduced from the reconstruction. The contrast of 10% between neighboring regions is smeared due to the noise in the diffraction patterns. The width of a single plateau with constant thickness is approximately 120 nm showing that the maximum spatial resolution of 30 nm is only achieved for a photon flux larger than 10^{15} photons/mm^2.

The photon flux in the experiment at ID10C was determined to be about $8 \cdot 10^6$ photons/(10μm^2)/s. Thus, to achieve a resolution of 30 nm would afford an exposure time of at least 3.5 h for a Au-sample of 5 μm size and a thickness of 150 nm.

A different approach to characterize the resolution of a reconstructed image uses the reconstructed phases of a series of independent reconstruction attempts. The method was first proposed by D. Shapiro [Sha05]. Further detailed information is given in [Cha06b].

The idea is to average the retrieved complex amplitudes in reciprocal space, $A(q_x, q_y)$, that were obtained in a number of reconstruction trials starting each from a different set of random phases, i.e., $\bar{A}(q_x, q_y) = 1/N \cdot \sum_{n=1}^{N} A_n(q_x, q_y)$, where N is the number of reconstruction trials. In case that the phases were retrieved consistently at a certain (q_x, q_y)-value the complex amplitudes add constructively and its absolute value should be comparable to the square root of the measured intensity, i.e., $|\bar{A}(q_x, q_y)|/\sqrt{I(q_x, q_y)} \approx 1$.

On the other hand, if the retrieved phases are differing the absolute value of the average tends towards zero in the limit of random phases. The values $|\bar{A}(q_x, q_y)|/\sqrt{I(q_x, q_y)}$ are then averaged over a shell of constant scattering vector $q = \sqrt{q_x^2 + q_y^2}$. Plotting these averaged values as function of q, respectively the resolution $d(q) = 2\pi/q$, defines a certain transfer function for the phase retrieval method, so-called phase retrieval transfer function (PRTF). It is a measure for the confidence in the reconstructed phases at a certain value of scattering vector q.

Notice that, due to the application of the shrink-wrap-method, the position of the reconstructed object inside the 2D-array is arbitrary which results in an arbitrary phase gradient between different retrieved phase sets. Without a correction of this phase gradient for every individual diffraction pattern the summation over all retrieved complex diffraction patterns would give an incorrect result. Let $\tilde{A}_1(q_x, q_y)$ and $\tilde{A}_2(q_x, q_y)$ be the complex amplitude of two individual diffraction patterns retrieved by using the described reconstruction method which main difference is the previously mentioned gradient in phase, i.e., $\tilde{A}_2(q_x, q_y) \approx \tilde{A}_1(q_x, q_y) \cdot e^{i\mathbf{k}\mathbf{r}_o}$, then follows that the expression $G(x, y) = \mathscr{F}^{-1}(\tilde{A}_1(q_x, q_y) \cdot \tilde{A}_2^*(q_x, q_y))$ defines the autocorrelation function of the object which is shifted in real space by a certain vector $\mathbf{r}_0$ relative to the center of the image. The value of $\mathbf{r}_0$ can easily be determined by finding the maximum of the autocorrelation function $G(x, y)$. The procedure to correct for the phase gradient is implemented as follows. The first complex amplitude $\tilde{A}_1(q_x, q_y)$ of the reconstructed diffraction patterns is read and stored in memory. Then, another reconstructed complex field $\tilde{A}_i(q_x, q_y)$ is read and multiplied with $\tilde{A}_1(q_x, q_y)$. By an inverse Fourier-transform the autocorrelation of the object is calculated and by finding the maximum of the autocorrelation image the value of $\mathbf{r}_0$ can be extracted. The complex amplitude of the latter diffraction pattern is then multiplied with the inverse phase gradient, i.e. $\tilde{A'}_i(q_x, q_y) = \tilde{A}_i(q_x, q_y) \cdot e^{-i\mathbf{k}\mathbf{r}_0}$. This step corresponds in real space to a shifting of the reconstructed image corresponding to $\tilde{A}_i(q_x, q_y)$ onto the position of the sample as it was found in the reconstruction corresponding to the diffraction data $\tilde{A}_1(q_x, q_y)$. $\tilde{A'}_i(q_x, q_y)$ is then added to a mean field $\bar{A}(q_x, q_y)$ which is used to determine the phase retrieval transfer function. The procedure is repeated for every further reconstructed diffraction pattern. In this way, the reconstructed diffraction amplitudes can be summed without degrading the phase retrieval transfer function.

This method to define the resolution was also applied to the reconstructed images of this section. In Fig. 5.14 the final result of the PRTF for different values of total photon flux is shown. Each of these curves was obtained from 30 individual reconstructed images. The comparison between the phase retrieval transfer function and the line profiles shown previously suggests that the resolution limit is well defined by the value where the transfer function decreases to about 10%. For example, the resolution for a photon flux of 10^{14} is then given by approximately $50 - 60\,\mathrm{nm}$ which is in good agreement with the result presented in Fig. 5.13.

Notice further that the power spectrum of the original diffraction patterns with Poisson-

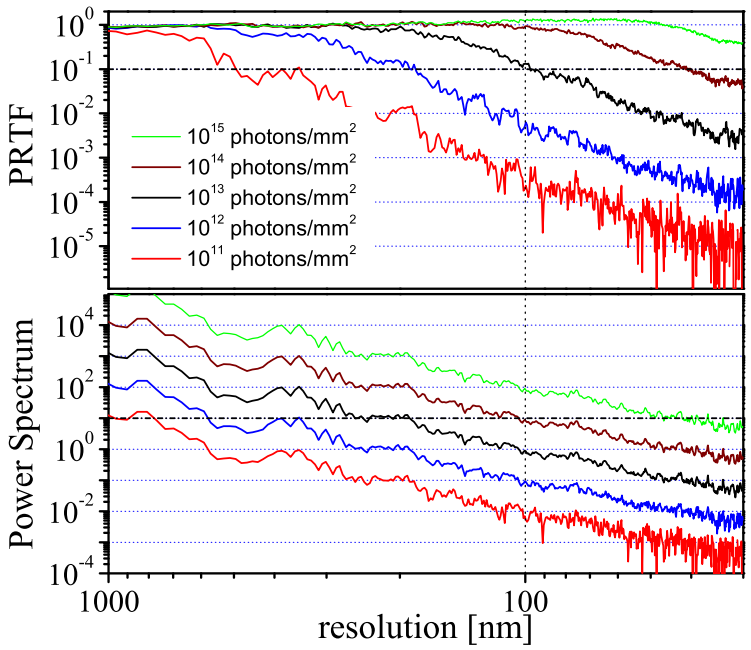

Figure 5.14: Phase retrieval transfer function (PRTF) resulting from 30 individual reconstruction attempts with different starting phases. For comparison the power spectra for different values of photon flux determined from the noisy diffraction patterns are shown. The latter is a measure of mean number of photons at a certain resolution shell $|q|$.

noise is characterized by a steep decrease of intensity (cf. the lower diagram in Fig. 5.14). For example, in case of an incident photon flux of 10^{14} photons/mm^2 the mean number of photons scattered to an angle corresponding to 50 nm-resolution is only a single photon. This is not a statistically significant number. Nevertheless, due to the oversampling of the diffraction pattern approximately 10 pixels could be integrated to one pixel without losing structural information. This means, the important quantity in order to define the resolution is the number of photons per speckle. This number has to be in agreement with the usual resolution limit of $I/\sqrt{I} \approx 3$.

5.3 Partial Coherence

The size of the x-ray source defines the reduction of the spatial coherence length at the sample position (cf. Sec. 2.6). Nevertheless, in the experiment this quantity is also influenced by optical components upstream the sample giving rise to a distorted incoming wave front and the stability of the setup during the measurement. Therefore, the spatial coherence is usually not as perfect as predicted by the theory. A degraded coherence length of the x-ray beam is related to a convolution of the diffraction pattern.
This smearing of the diffraction pattern is not considered by the Hybrid-Input-Output-algorithm (HIO) and leads to artifacts in the inverted image. This is due to the fact

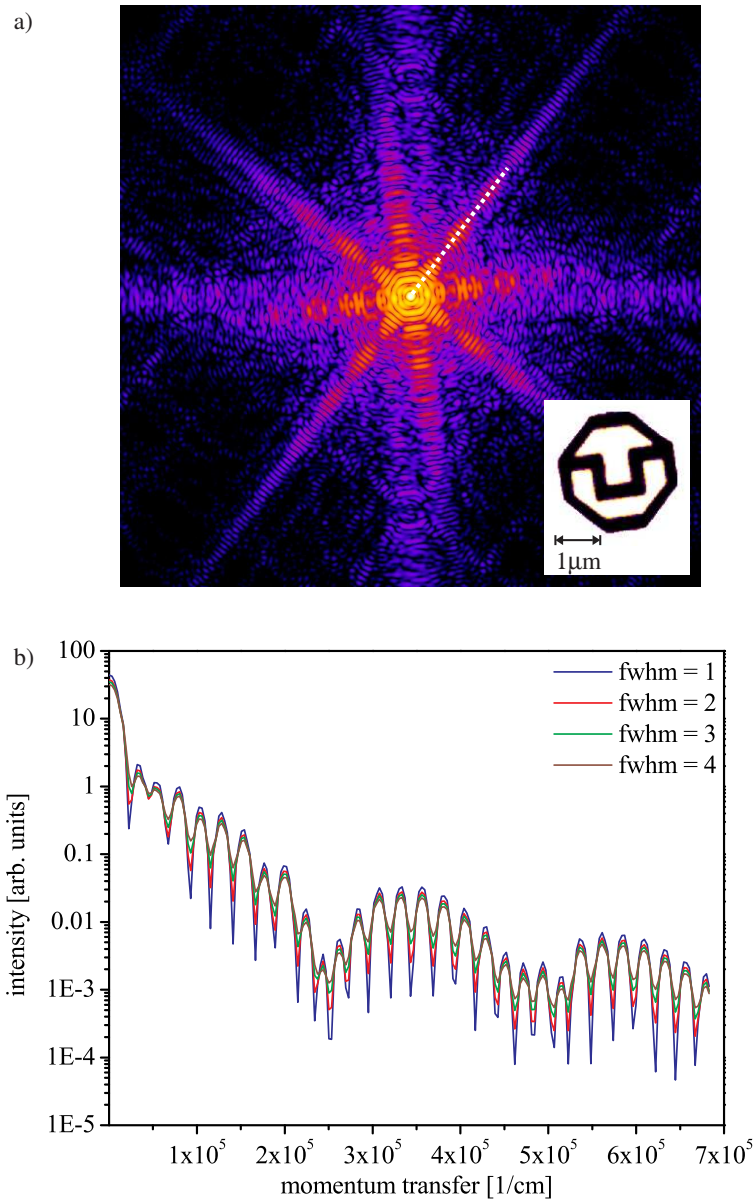

Figure 5.15: a) Diffraction pattern of a simulated gold structure with a size of 3 µm and a thickness of 150 nm. The shape of the sample, akin to the logo of the Technische Universität Dresden, is shown in the inset. In order to simulate the effect of partial coherence the diffraction pattern shown in a) was convolved with a gaussian of different FWHM values (1 to 4 pixels) and the resulting patterns were used as input data for the HIO-algorithm. b) Line profiles are taken along the dotted line indicated in Fig. a) for different degrees of gaussian convolution.

that the algorithm uses the forward- and inverse Fourier-transform to propagate between real- and reciprocal-space which assumes a perfect spatial coherence of the x-ray light. In the following the influence of partially coherent illumination on the reconstruction result will be studied.

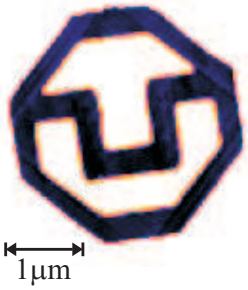

(a) Gaussian FWHM = 1, $l_t = 16.5\,\mu m$

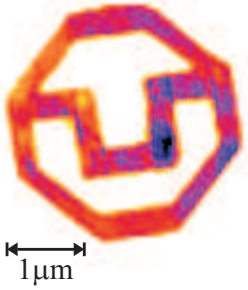

(b) Gaussian FWHM = 2, $l_t = 8.2\,\mu m$

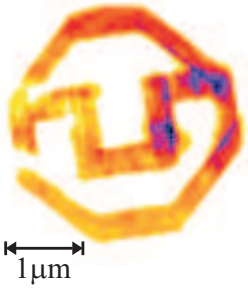

(c) Gaussian FWHM = 3, $l_t = 5.3\,\mu m$

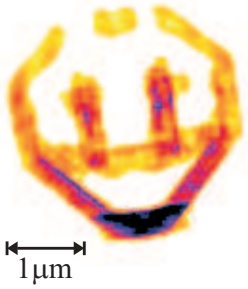

(d) Gaussian FWHM = 4, $l_t = 4.1\,\mu m$

Figure 5.16: Reconstruction results from the data set presented in Fig. 5.15 a). In order to simulate partial coherence effects the diffraction pattern was convolved with a gaussian of certain FWHM. In Figs. (a)-(d) different HIO-reconstruction results are shown. The degree of convolution applied to the initial diffraction pattern as well as the corresponding transverse coherence length at the sample position are indicated in each panel.

As a test sample served a two-dimensional gold structure with the shape of the TU-Dresden logo having a size of 3 µm and a thickness of the Au-layer of 150 nm (cf. 5.15 a)). The oversampling ratio is approximately 8 in each dimension. The parameters of this simulation are very similar to experimental parameters during the measurements at ID10C (cf. Sec. 4.2).
The corresponding diffraction pattern was then convolved with a gaussian function of different FWHM-values ranging from 1 to 4 pixels in order to simulate the effect of partial coherence. The convolution with 1 pixel is related to a lateral coherence length of approximately $l_t = 16.5\,\mu m$ for a photon energy of $E = 8\,keV$, sample-detector distance $L = 3.2\,m$ and a pixel size of the detector $p = 20\,\mu m$ (cf. Eq. (2.75)). A gaussian convolution of 2, 3, and 4 pixels FWHM corresponds to a lateral coherence length of 8.2 µm,

5.3 µm, and 4.1 µm, respectively. In Fig. 5.15 b) line profiles along the dotted line, which is indicated in Fig. 5.15 a), are plotted versus the scattering vector. It illustrates the loss in visibility of diffraction fringes due to the convolution of the diffraction pattern. The smeared data were used as the input data for the reconstruction with the shrink-wrap algorithm. The result of these reconstructions is summarized in Fig. 5.16.

In the case of a convolution with a gaussian of one pixel FWHM the reconstruction result is quantitatively still representative while already in case of a 2 pixels FWHM gaussian convolution the reconstructed electron density inside the object is not constant but fluctuates during the iterative procedure. Bright and dark regions appear at arbitrary positions in the region of the sample indicating the stagnation of the algorithm. This case is very similar to measurements at ID10C showing that the effective transverse coherence length in this measurement series was about 8 µm (cf. Sec. 4.2.1). For a stronger convolution, cf. Fig. 5.16(c) and Fig. 5.16(d), severe artifacts appear in the inverted image. Although the lateral coherence length at the sample position is still about 4 µm even the shape of the object can not be recovered by the algorithm and a strong variation of density is visible in the reconstructed image.

This simulation series proves that the transverse coherence length must be much larger than the size of the sample in order to allow for a quantitative reconstruction of the object. In the case of a flat illumination and a lateral coherence length similar to the size of the object important long range correlation is already lost and can not be recovered by the reconstruction algorithm.

In the following first tests of a genetic algorithm are presented. Since this algorithm does only use the forward Fourier-transform it is possible to insert the effect of partial coherence and the influence of the illumination wave field into the reconstruction model.

5.4 Reconstructions with a Genetic Algorithm

In order to test the performance of the genetic algorithm described in Sec. 2.7.6 different reconstructions were carried out on simulated diffraction data.
In Fig. 5.17 the reconstruction result of a simulated Euro-shaped structure is summarized. It was assumed that the object is real-valued and can take values of 0 and 1, i.e., it is a binary object. The size of the reconstruction array was 256×256 pixels and the object itself is about 80×80 pixels large. In Fig. 5.17 a) and Fig. 5.17 b) the transmitted intensity after the object and the corresponding diffraction pattern are shown. The following parameters were used in this simulation. The population had 200 members and a single generation was completed after 200 reproduction steps. The probability of crossover and mutation was given with 35 % and 0.005 %, respectively. The central pixel of the diffraction pattern was not considered in this simulation. In Fig. 5.17 c) the evolution of the best member is presented. The indicated number refers to the current generation. The final result after 20 000 iterations is highlighted by a frame.
The convergence of the algorithm is relatively fast in the beginning of the iterative process and main features of the object are already visible after 1 200 generations. However afterwards, the convergence of the algorithm is slower and fine details of the object are much harder to recover. After generation 10 000 improvements of the members are mainly due to mutation and, therefore, since crossover is less important the genetic algorithm is less efficient.

In another simulation the object under investigation was the Linux-penguin shown in Fig. 5.18. In this case the simulation was more adapted to the real experiment. It was assumed that it is an Au-object with a maximum thickness of the Au-layer of 150 nm. Maximum absorption corresponds to the black color in Fig. 5.18 a) whereas grey values indicate an intermediate thickness of the material. The total size of the array was 256×256 pixels and the object occupied about 80×100 pixels in horizontal and vertical direction, respectively. The complex exit wave field after the sample was calculated for a photon energy of 7 keV giving a maximum phase shift of $\Delta\varphi_{\mathrm{Au}}(7\,\mathrm{keV}) = -0.34\,\mathrm{rad}$ and maximum absorption of 7.6 %. The corresponding diffraction pattern (Fig. 5.18 b)) was calculated from the complex exit wave field after the sample. The central part of the diffraction pattern of about 3×3 pixels was not used for the reconstruction.

The main difference compared to the previous simulation is that the varied parameter is the thickness of the material which could have arbitrary values between 0 nm and 150 nm. This implies that the searched parameter space is much larger and, therefore, it should be more difficult for the genetic algorithm to find the true solution. A member has to be considered now as a complex array with 256×256 pixels. In the crossover-routine the stored complex values are simply exchanged between two members whereas in the mutation-routine the complex values of the exit wave field in a certain pixel are calculated based on an arbitrary thickness value of the material ranging from 0 nm to 150 nm.

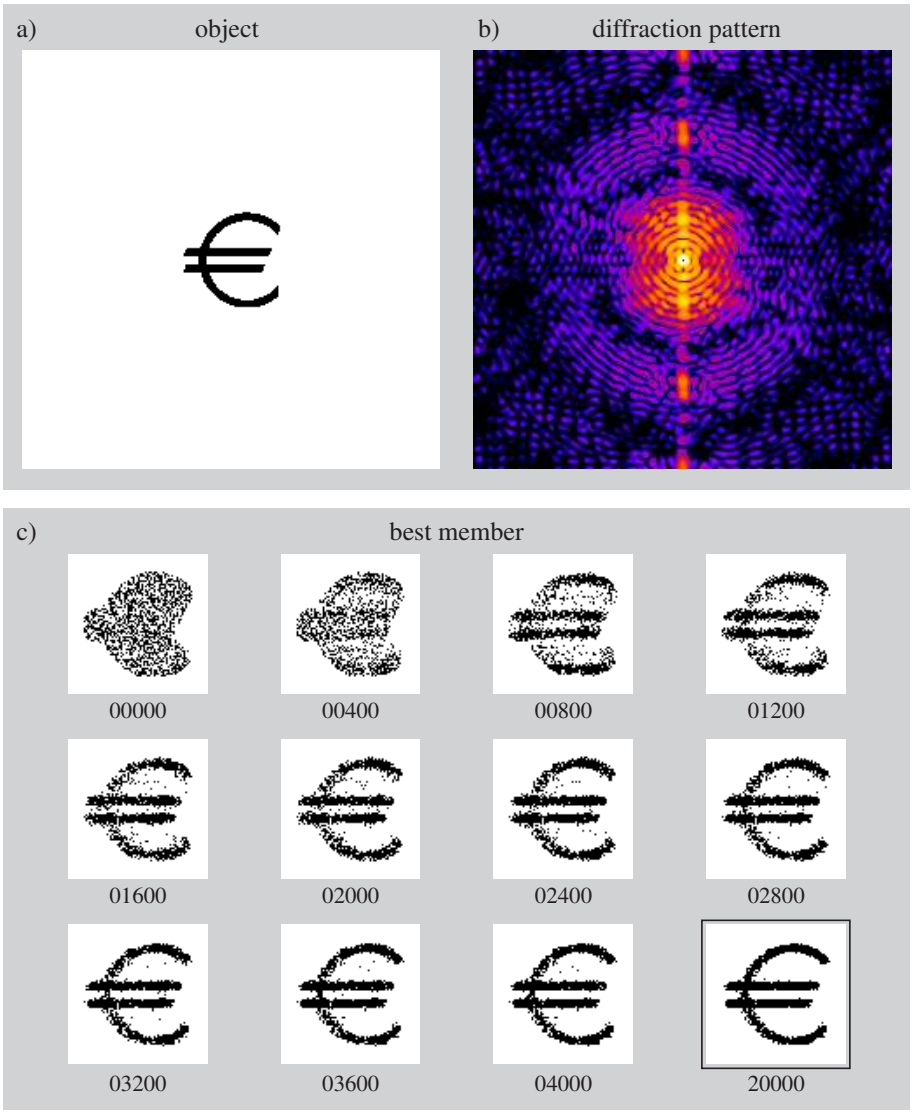

Figure 5.17: a) Simulated binary object. The size of the matrix is 256×256 pixels and the object could have values of 0 and 1. The object occupies an area of about 80×80 pixels. b) Corresponding diffraction pattern. c) Evolution of the best member. The number below the images refers to the generation number.

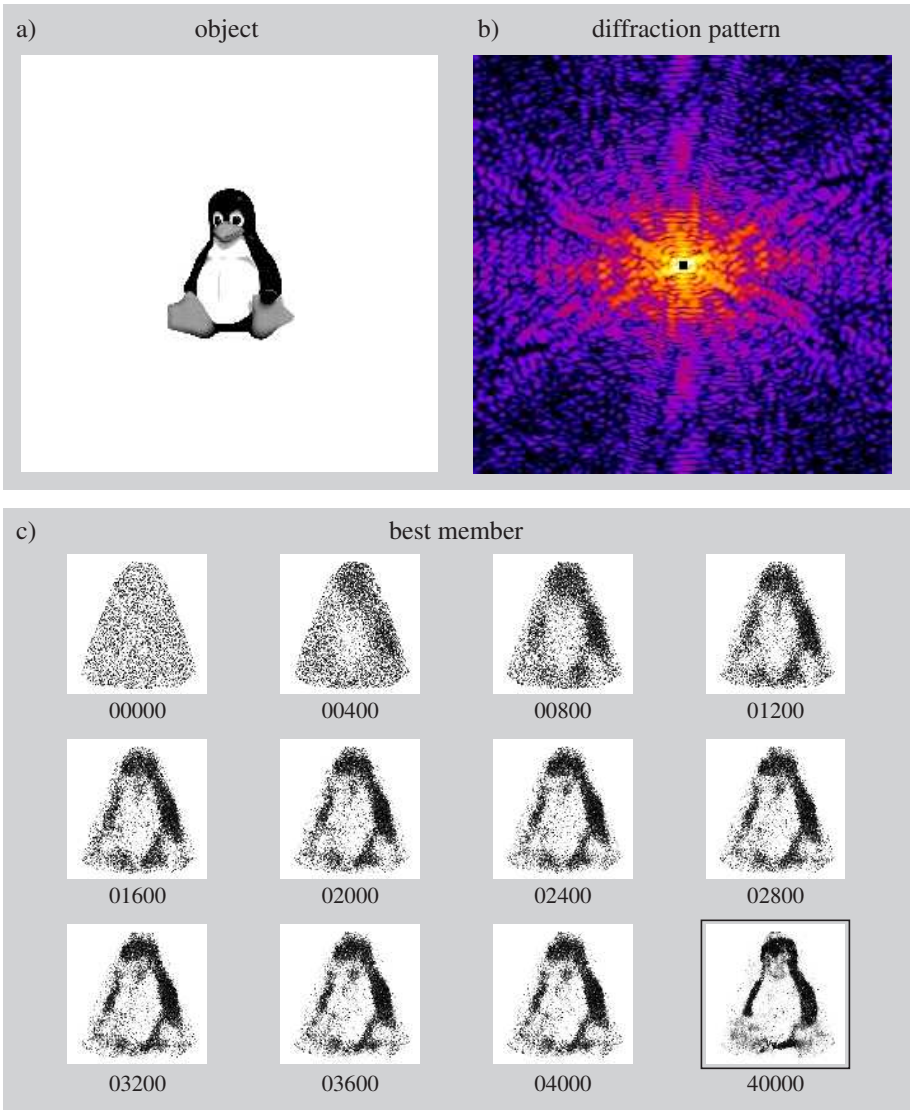

Figure 5.18: a) Transmitted intensity after the object. The object is a two-dimensional Au-sample with maximum thickness of 150 nm. The black color indicates strongest absorption. b) Corresponding diffraction pattern. c) Evolution of the best member. The number refers to the generation number. The best member in generation 40 000 is highlighted by a frame.

From the complex exit wave field the diffraction pattern is calculated and compared to the given intensity data. The deviation is defined by the usual χ^2-value and the fitness of a certain member is given by the reciprocal value of χ^2. The details of this simulation were as follows. The size of the population was 400 and the number of iterations per generation was also 400. Similar as in the previous simulation the probability of crossover and mutation was 35 % and 0.005 %, respectively.

In Fig. 5.19 the χ^2-error of the best and worst member of the population is illustrated. In the beginning the error of the members strongly decreases. However, after generation 4 000 the convergence is very slow and the fine structure of the object is very hard to reconstruct for the genetic algorithm.

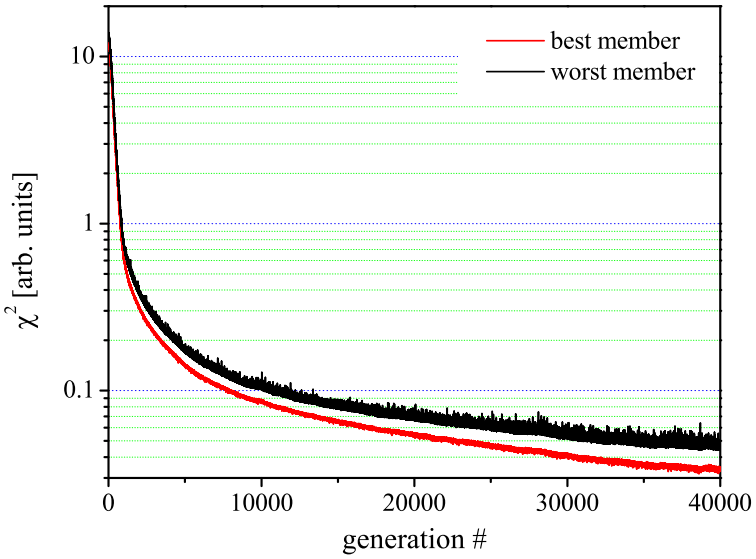

Figure 5.19: Fitness of the best and the worst member of the simulation presented in Fig. 5.18.

In Fig. 5.18 c) the final result of the reconstruction of the penguin is shown. Certain features of the object such as the feet with lower contrast, nose and eyes become visible in generation 40 000 only.
In comparison to the HIO-algorithm the convergence of the genetic algorithm is much slower and the time necessary to carry out this reconstruction is unequally longer. The HIO-algorithm would recover the electron density in less than a quarter of an hour whereas the genetic algorithm needs days to find an approximate solution. Nevertheless, the genetic algorithm is still attractive for phase reconstruction since other experimental conditions such as partial coherence can be implemented in the calculation of the fitness. The genetic algorithm does not need the inverse Fourier-transform which causes trouble in HIO-reconstructions if the diffraction pattern is partially smeared (cf. Sec. 5.3). Additionally, it is conceivable that the genetic algorithm is a good alternative in phase retrieval for problems having a lower dimensionality.

5.5 Ptychographic Reconstruction

The ptychographic reconstruction method introduced in Sec. 2.7.5 is one of the most promising methods for phase retrieval from diffraction patterns of non-translational periodic objects. The main strength of this phase retrieval method is the possibility to image extended objects by scanning a well defined incident wave front over the sample and by recording at each position the corresponding diffraction pattern. This coherent illumination wave field is very important for the method since it defines the area of the sample that contributes to a certain diffraction pattern. The scanning of the sample under the condition that the illuminated areas overlap facilitates extraordinarily the reconstruction of the complex exit wave field. The overlap between these illuminated areas usually breaks immediately internal symmetries and, therefore, the reconstruction does not suffer from the twin image problem like the HIO-method. Nevertheless, the method requires that the illumination function as well as the position of the illumination is accurately known. In order to test the sensitivity of the ptychographic reconstruction method on the knowledge of the position of the illumination function a series of simulations was carried out which intentionally assumed that the position of the illumination is offset from the accurate position by a small distance, i.e., from 1 to 5 pixels.

In Fig. 5.20 an overview of the following simulation is given. The object is assumed to be a 2D-gold structure with the shape of the DESY-logo and with a thickness of 150 nm. In Fig. 5.20 a) the transmitted intensity is shown. The photon energy is 8 keV. The black color indicates maximum absorption. This sample with a lateral size of 15 µm is now illuminated with a sharp, circular illumination function having a diameter of 5 µm (cf. Fig. 5.20 b)) which acts like a pinhole. The illumination was shifted to nine different positions on the object giving also nine distinct diffraction patterns. Each of the illuminated areas is indicated by a circle in Fig. 5.20 a). The distance between these regions was 2.5 µm and, therefore, the overlap between these regions is sufficiently large. Obviously, since the multiplication of illumination function and object function in real space corresponds in reciprocal space to a convolution of the individual Fourier-transforms the diffraction pattern is strongly determined by the illumination function. In Fig. 5.20 c) a single diffraction pattern is shown. The corresponding illuminated area is highlighted by a blue circle in Fig. 5.20 a).
Provided that the position and the shape of the illumination is precisely known the reconstruction of the complex exit wave field is very fast (Fig. 5.21 a)). The phase retrieval needs only about 300 iterations. However, in further simulations a lateral offset of the illumination was intentionally introduced simulating the effect that it may not be accurately known in the experiment. This means that the diffraction patterns were not changed but the position of the illumination function was set to a wrong value in the ptychographic reconstruction. The offset concerned the outer illumination regions that were shifted by a certain distance from the central region. The exact offset introduced was between 20 nm and 100 nm which corresponds to approximately 1 to 5 pixels. The size of a pixel was 24 nm. In Fig. 5.21 b) the reconstruction result for different offset values is shown.

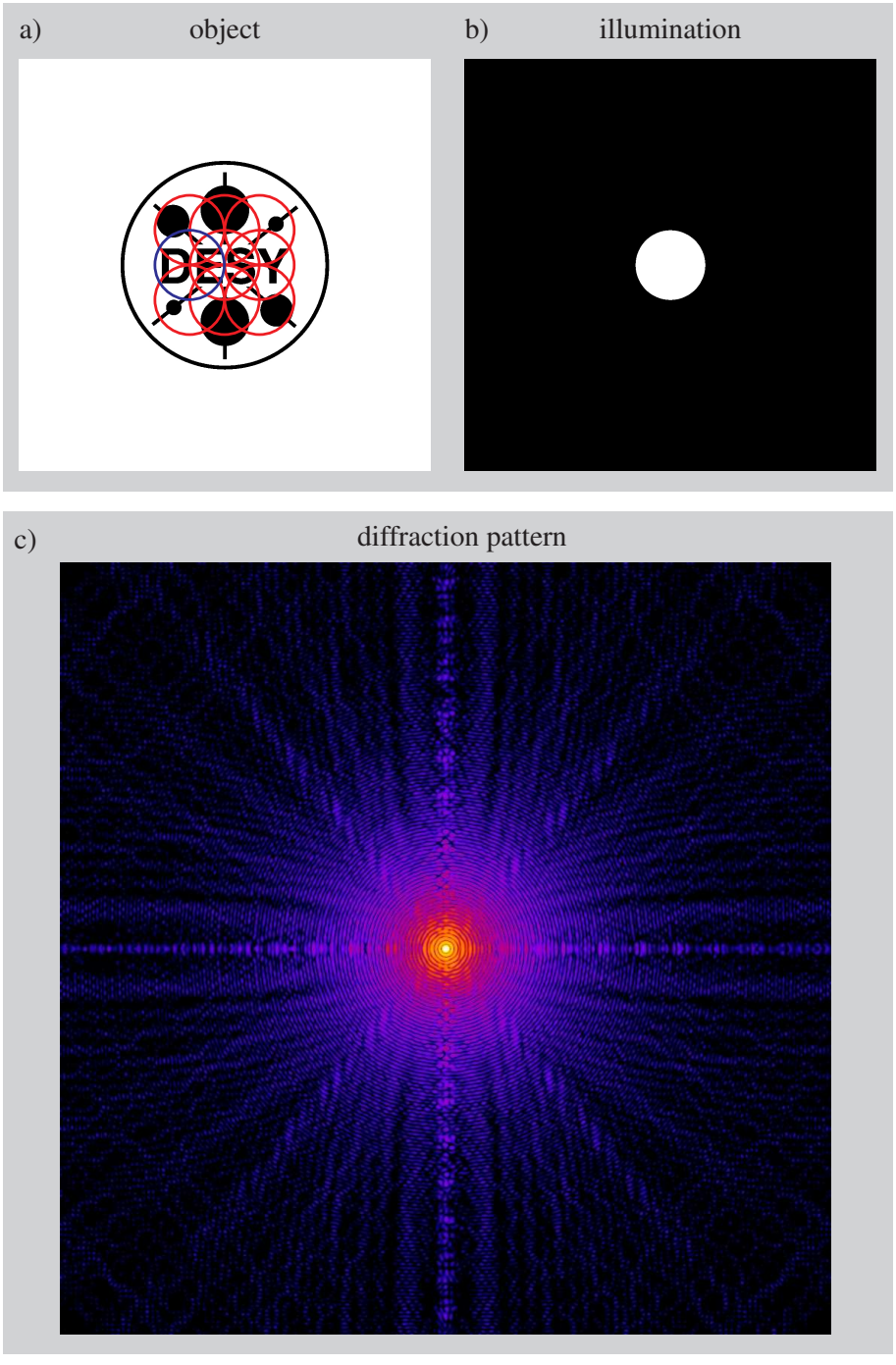

Figure 5.20: a) 2D-Au-sample with a size of 15 µm. The circles define different illuminated regions. For each of them a distinct diffraction pattern is calculated. b) Illumination function used with a diameter of 5 µm. c) Calculated diffraction pattern of the sample related to the area indicated by the blue circle in image a).

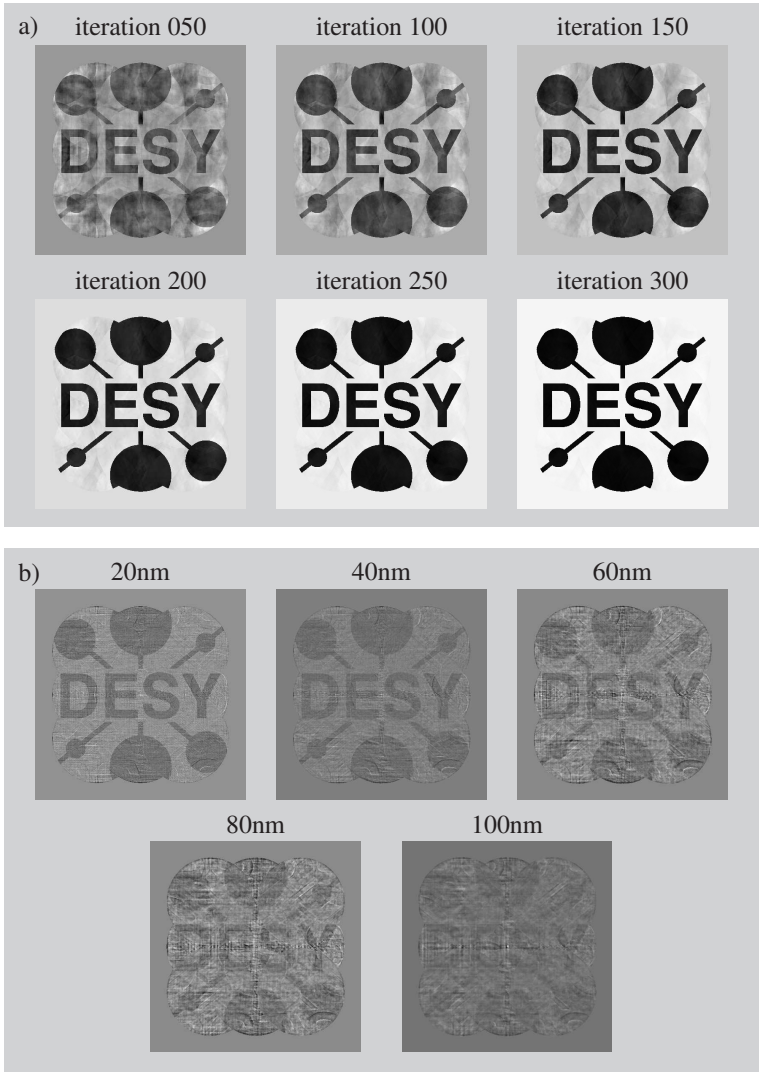

Figure 5.21: a) Reconstruction with exact knowledge of the position of the illumination function. After 300 iterations the complex exit wave field has been perfectly recovered by the algorithm. b) Reconstruction result after 2 000 iterations in case that the position of the illumination function was intentionally assumed to be slightly offset from the real value. The exact offset is indicated in each image.

The discrepancy in the positioning of the illumination function leads to a fast decrease of contrast in the reconstructed image. It signifies that the positioning of the illumination function in discrete steps has to be carried out with a similar precision as can be expected from phase recovery of an individual diffraction pattern. This is an important aspect that has to be taken into account in future experiments. Additionally, it may be conceivable that the algorithm refines besides the phases of the diffraction pattern also the position and shape of the illumination function during the iterative procedure.
First evidence that the ptychographic method is experimentally feasible was presented by J. M. Rodenburg [Rod07].

5.6 Discussion

A main limitation in the experiment was the difficulty to properly measure low-resolution diffraction data due to the high intensity of parasitic scattering close to the direct x-ray beam. In order to reduce this scattering Silicon-corners were tested in the experiment. However, at harder x-rays ($E = 8\,\mathrm{keV}$) the efficiency of absorption as well as refraction of the corners is low and even in the case that multiple corners are stacked in series along the beam it is not sufficient to shadow the CCD from the parasitic scattering of the beam-defining slit. This observation was confirmed by numerical simulations in Sec. 5.1.1.

In Sec. 5.2 and Sec. 5.3 the influence of Poisson-noise and partial coherence on the result of a reconstruction has been discussed. Whereas a limited number of photons reduces only the final resolution of the inverted image partial coherence effects introduce severe artifacts in the reconstructed image due to the fact that the loss of contrast is falsely interpreted by the HIO-algorithm. In the latter case hot spots of electron density appear typically in the reconstructed image.

The photon flux of 10^{15} photons/mm^2 necessary to achieve a resolution of 30 nm for a gold sample with a size of 5 µm and a thickness of the Au-layer of 150 nm is in good agreement with the discussion of the resolution limit in the diffraction pattern of gold spheres presented in Sec. 4.3. Nevertheless, a more thorough theoretical investigation is necessary with regard to the connection of sample size and achievable resolution. Focusing techniques will be certainly necessary in future CXDI-applications on non-periodic objects if sub-nanometer resolution is desired.

The ptychographic phase retrieval technique turns out to be very promising for high-resolution imaging of extended object. The algorithm works very efficiently if the shape and position of the illumination wave function is accurately known. Further investigation is necessary concerning the improvement of the algorithm if the illumination has to be refined beside the reconstruction of the complex object.
A genetic algorithm for phase retrieval was implemented and tested. The main advantage of this algorithm is the possibility to introduce further experimental parameters such as

partial coherence effects or a distorted illumination field. However, compared to the other reconstruction methods the convergence of this algorithm is very slow. It can be a good alternative method for phase retrieval problems with lower dimensionality.

6 Reconstruction from Measured Data

In this chapter reconstruction results from measured data are shown. Details about the measurements and the recording of the data were presented in Chap. 4. These results are compared and discussed in the context of simulation results shown in Chap. 5.

6.1 Euro-sample

The analysis of the data presented in Sec. 4.1.4 showed that the visibility of the fringes in the diffraction pattern (cf. Fig. 4.6) is quite reduced. The qualitative comparison between measured and calculated data reveals a smearing of the diffraction pattern corresponding to a convolution with a Gaussian of 3 pixels FWHM. This is related to a transverse coherence length of approximately 8.2 µm at the sample position. Using these data without any correction of the reduced visibility the reconstruction with the HIO-method does not inspire much confidence in the result as was theoretically explained in Sec. 5.3.

In the following, a short explanation of the Wiener-deconvolution method is given. Consider a certain function $I'(\mathbf{x})$ that is smeared, or convolved, by a certain point spread function $f(\mathbf{x})$, i.e. $I'(\mathbf{x}) = I(\mathbf{x}) \otimes f(\mathbf{x})$, where '$\otimes$' denotes the convolution operation. This convolution of the image corresponds in frequency space to a multiplication of the individual Fourier transforms: $\tilde{I}'(\mathbf{k}) = \tilde{I}(\mathbf{k}) \cdot \tilde{f}(\mathbf{k})$, where $\tilde{I}'(\mathbf{k}) = \mathscr{F}(I'(\mathbf{x}))$, $\tilde{f}(\mathbf{k}) = \mathscr{F}(f(\mathbf{x}))$, and $\tilde{I}(\mathbf{k}) = \mathscr{F}(I(\mathbf{x}))$. This means that the Fourier-representation of the deconvolved image would be just given by $\tilde{I}(\mathbf{k}) = \tilde{I}'(\mathbf{k})/\tilde{f}(\mathbf{k})$. However, this division is problematic if the function $\tilde{f}(\mathbf{k})$ contains zeros or very small numbers. For this reason, a small additive regularization term α has to be introduced in the denominator in order to prevent the division by zero. This leads finally to the expression

$$\tilde{I}(\mathbf{k}) = \frac{\tilde{I}'(\mathbf{k})\tilde{f}^*(\mathbf{k})}{|\tilde{f}(\mathbf{k})|^2 + \alpha}. \tag{6.1}$$

The asterisk denotes the complex conjugate of the complex function. The corrected image is then given by $I(\mathbf{x}) = \mathscr{F}^{-1}(\tilde{I}(\mathbf{k}))$. This procedure to correct for the smearing of some image is called a Wiener-deconvolution and can be applied if the point-spread function $f(\mathbf{x})$ is known. The result of this deconvolution method is quite sensitive to the choice of the parameter α. The diffraction pattern of the Euro-sample presented in Fig. 4.6 was deconvolved using this method.

Additionally, it is known that this method amplifies noise in the image and, therefore, only the central part with a size of 512×512 pixels of the original diffraction pattern was used for the deconvolution. The original size of the diffraction pattern was 1340×1300 pixels. In Fig. 6.1(a) the diffraction pattern after Wiener deconvolution using a Gaussian with full width at half maximum (FWHM) of 3 pixels and a regularization factor of 10^{-2} is shown. For these parameters best reconstruction results were obtained.
The application of the Wiener deconvolution strongly pushes the minima of the diffraction pattern to very low values which appears somewhat artificial. Nevertheless, the high contrast of the diffraction fringes is necessary for the success of the HIO-algorithm. Reconstruction attempts on simulated data that were first convolved with a Gaussian and afterwards deconvolved with the Wiener filter proved that the application of this method is convenient to correct for a partial smearing of the diffraction pattern. The reconstruction from the deconvolved data gives much better results compared to the smeared data. In general however, the knowledge of the exact mutual coherence function is important for the proper deconvolution of the diffraction pattern. In the present case, the deconvolution of the diffraction pattern has to considered as a first approach to correct for partial coherence effects.

Certain parts of the deconvolved diffraction pattern (cf. Fig. 6.1(a)) were strongly contaminated by x-ray scattering from the slits and could not be used for the iterative phase retrieval. These parts are indicated by the black color in the mask-image shown in Fig. 6.1(b). In these areas of the diffraction pattern the intensity was not restricted during the iterative reconstruction procedure.

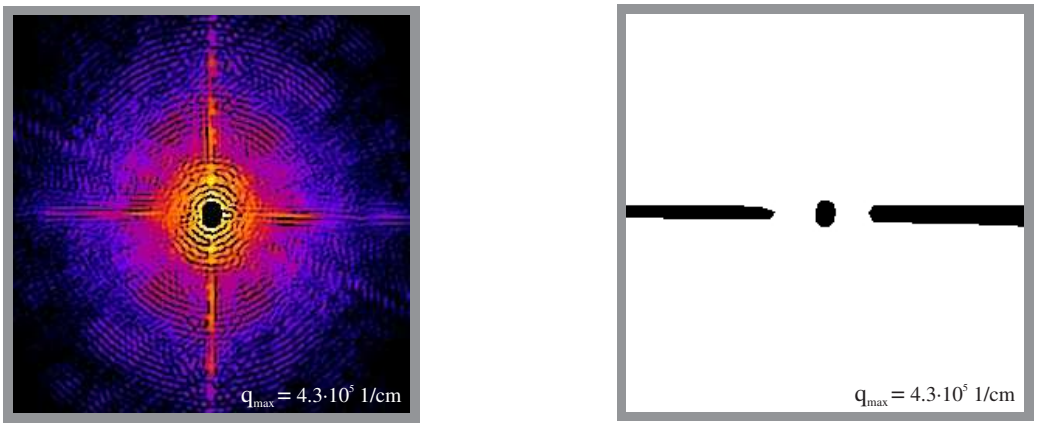

(a) Diffraction pattern after deconvolution. **(b)** Mask

Figure 6.1: a) Diffraction pattern used for reconstruction. In order to correct for partial coherence effects a Wiener-filter was applied to deconvolve the original diffraction pattern.
b) Areas of the diffraction pattern with strong contribution of slit scattering, indicated by black color, were not considered in the reconstruction. The maximum scattering vector is the same in both images.

In Fig. 6.2(a) and Fig. 6.2(b) best reconstruction results with a fixed support and using

the shrink-wrap method are shown. Both reconstructions were carried out using the modified HIO-algorithm with parameters of $\beta = 0.95$ and $\alpha = 0.5$. The starting phases were randomized and the initial guess of the object was enclosed by a relatively tight support. The frame of the support is indicated by a red line in Fig. 6.2(a). The tight support is especially important if too much low frequency information is missing. Nevertheless, despite the missing low frequency data the sample is clearly recognizable and in certain areas sharp edges can be noticed. Nevertheless, since the reconstruction method relies on the pure Fourier-transform of the object the signal due to slit scattering and partial coherence is not properly interpreted by the algorithm. For this reason a laterally extended background signal appears in the reconstructed image.

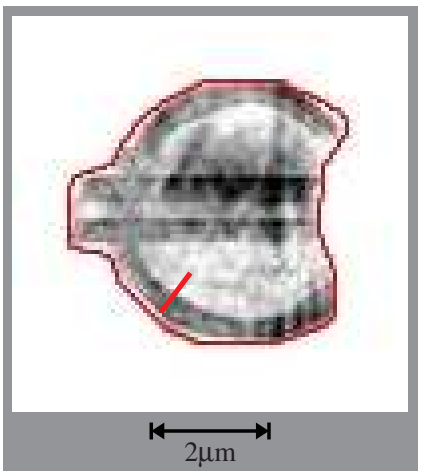

(a) Fixed support

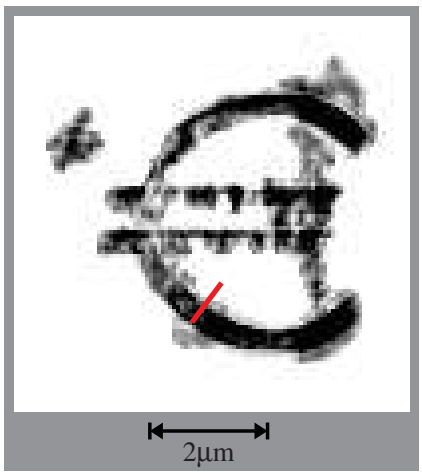

(b) Shrink-wrap

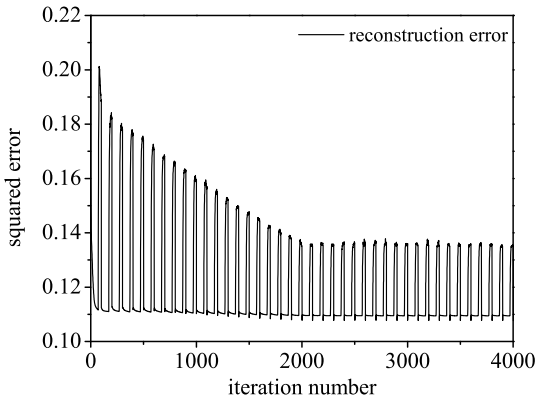

(c) Reconstruction error

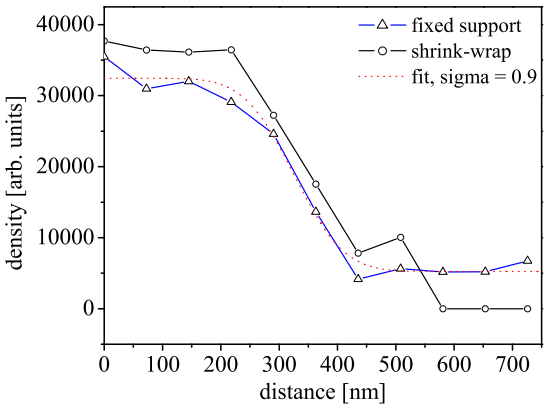

(d) Line profiles from Figs. (a) and (b)

Figure 6.2: Reconstruction results achieved using the HIO-algorithm with a tight support (a) and using additionally the shrink-wrap method (b). c) Evolution of the χ^2-error during the reconstruction process. d) Line profiles along the red line of Figs. (a) and (b) show a sharp contrast of 2 pixels in certain areas of the reconstructed image.

In this case, the application of the shrink-wrap method turns out to give slightly better results due to its capability to shrink, or if necessary also increase, the size of the support during the iteration process. This means, the algorithm has more freedom to find the appropriate solution and, especially in the case that further, eventually unknown, scatterers were present around the object, the latter method turns out to be advantageous. The reconstruction result shown in Fig. 6.2(b) and the fine structured interference already mentioned in Sec. 4.1.4 support this conclusion. Unfortunately, due to the damage of the sample directly after the measurement, a verification with a scanning electron microscope was not possible.

The reconstructions presented in Figs. 6.2(a) and 6.2(b) were carried out with subsequent switching between the error-reduction algorithm for 70 iterations and the HIO-algorithm for 30 iterations. During the application of the HIO-constraints the error typically increases as can be seen in Fig. 6.2(c) for the reconstruction with the tight support. The total number of cycles was 20 000 for both reconstructions shown. Nevertheless, beyond iteration number 4 000 the algorithm stagnates and no dramatic improvements of the reconstructed image can be observed. The error stagnates at a level of about 0.1 as shown in Fig. 6.2(c) indicating that, despite the correction of the data, there is still a relatively high inconsistency between measured and calculated data. The low convergence of the HIO-algorithm is attributed to the quality of the data.

The analysis of line profiles taken along a specified direction which is indicated by a red line in Figs. 6.2(a) and 6.2(b), proves a sharp contrast of approximately 2 pixels FWHM for both reconstruction trials (cf. Fig. 6.2(d)). It corresponds to a resolution of about 145 nm. The maximum possible resolution defined by the total size of the CCD would have been 57 nm.
Nevertheless, it has to be mentioned that the position of the background signal between individual reconstruction attempts changes considerably, and, therefore, the summation over many trials would downgrade the overall resolution. In the present case only the best reconstruction results are presented.

Assuming that the convolution with a gaussian of 3 pixels FWHM is the proper description for the influence of partial coherence in this measurement the lateral coherence length at the sample position can be derived from Eq. (2.75) to $l_t \approx 8.2\,\mu\text{m}$. The ratio of transverse coherence length to sample size is similar as in the reconstruction result from simulated smeared data presented in Fig. 5.16(c) of Sec. 5.3. Thus, a correction for the smearing of the diffraction pattern was certainly necessary in this case.
The lateral coherence length found in this measurement is well below the value expected for a low-beta source. It is most probably due to vibrations of the monochromator and a slight sagittal bending of the second monochromator crystal at that time.

6.2 Siemens-Star, Spiral and TU-Dresden logo

Regarding the coherence properties of the x-ray beam the measurement at ID10C turned out to be slightly better than at ID01. Nevertheless, also in this case the reconstruction of the samples from measured data only turned out to be difficult due to the background signal from the Si_3N_4-membrane, loss of low frequency information, partially reduced visibility of interference fringes and inhomogeneity of the illumination. In this section the influence of these effects on the reconstruction result is shown and will be discussed in the same order.

6.2.1 Background Signal

The illuminated area on the sample position was effectively about $3-4$ times larger than the sample size. This approach was intentionally chosen in order to ensure an almost flat illumination over the size of the sample. At the same time due to the internal structure of the 200 nm-thick Si_3N_4-membrane, this larger illumination produces a strong background signal at small q-values. Effectively, there is even a certain distribution of very small speckles visible. However, these are not properly sampled by the detection system. First reconstruction tests on the raw data proved that the subtraction of this background signal from the measured is mandatory. In order to determine the background the scattering signal only from the Si_3N_4-membrane was measured (cf. Fig. 6.3(a)).

By subtracting this pattern from the measured diffraction pattern of a sample allows to make a correction for this background signal. In a first test the diffraction pattern of the TU-Dresden logo was used and the diffraction pattern of the membrane multiplied by a certain factor was subtracted from it. The multiplication factor was varied in a certain range which gives a series of diffraction patterns with different degree of background correction. The exposure time of the membrane diffraction pattern was similar as in the measurement of the TU-Dresden logo and, thus, best reconstruction results can be expected for a multiplication factor around one or slightly larger due to the continuous decrease of synchrotron current during measurements. These data were directly used as input data for the HIO-algorithm producing a series of different reconstructed real space images. In Fig. 6.3(b) the final result is summarized. The specific multiplication factor is indicated in each individual image of Fig. 6.3(b).
These reconstructions were carried out using the modified-HIO-algorithm with $\beta = 0.8$ and $\alpha = 0.9$. Data in the central part with a diameter of 40 pixels, i.e., approximately two fringes, were not considered. The fixed support is indicated in image II) where regions outside the support are highlighted in red color. It was necessary to exclude a certain area inside the object in order to break a mirror symmetry of the object. Without that the algorithm often stagnates as a result of the twin-image problem (cf. Sec. 2.7.1). The support defined in this way is only consistent with one orientation of the object and forces the algorithm to follow the trajectory towards one solution.
The reconstruction series demonstrates that in case of a low background subtraction (cf. Fig. 6.3(b) I)) the MHIO-reconstruction is not able to produce the correct result.

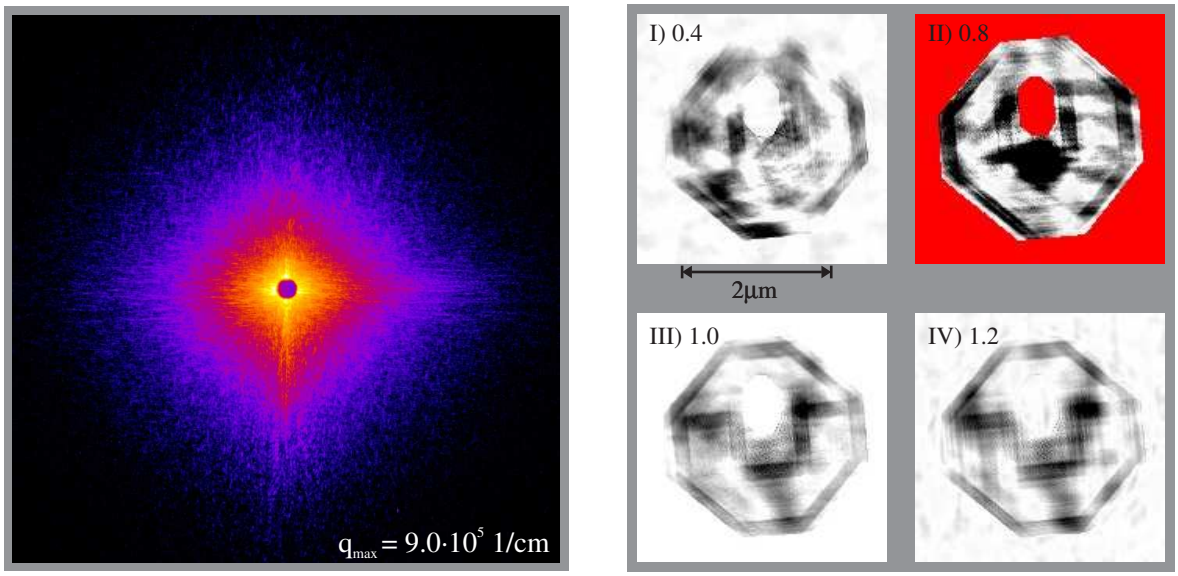

(a) Scattering signal from the Si_3N_4-membrane only. **(b)** Reconstruction results

Figure 6.3: Reconstruction tests on measured data of the TU-Dresden logo which were background corrected using the diffraction pattern of the Si_3N_4-membrane without object shown in image a). The multiplication factor applied to the background image before subtracting it from the measured data is indicated in each sub-image of b).

Even the shape of the object can hardly be recognized. In the case of a stronger subtraction the reconstruction result improves, though often, hot spots appear in the reconstruction that are typically related to partial coherence of the incoming beam (cf. Fig. 6.3(b) II)) [Var01, Var03a, Var03b, Rob03]. The reconstruction result of Fig. 6.3(b) III) shows the best reconstruction results. Though, still a high background level is visible. For stronger background corrections the quality of the reconstructed images decreases again.

6.2.2 Reconstruction Results

The diffraction patterns recorded from the lithographically prepared Au-structures were corrected for background scattering signal in the way described in the previous part. In Figs. 6.4 a), c), e) the diffraction patterns with subtracted background are shown. The original data were presented in Figs. 4.11, 4.10, and 4.9. In the right panel of Fig. 6.4 the diffraction patterns after deconvolution with a Wiener-filter using a Gaussian of 3 pixels FWHM and a regularization factor of 10^{-2} are presented.

Additionally, the diffraction patterns shown in Fig. 6.4 a) and Fig. 6.4 e) were symmetrized in an area with a radius of 300 pixels around the center in order to further decrease parasitic scattering signals. Since the diffraction pattern of the sample shows inversion symmetry relative to the central pixel a large deviation of intensity for one

pixel indicates that this signal is dominated by parasitic scattering. A strong deviation from inversion symmetry can be used for correction of certain bad pixels. The numerical implementation of the symmetrization-routine is described in App. A (tomo-routine: 809).

In Fig. 6.5 reconstruction results from diffraction patterns presented in Fig. 6.4 are shown. The panels correspond to each other, e.g. the reconstruction shown in Fig. 6.5 a) is the result of the diffraction pattern presented in Fig. 6.4 a).
Typically, the β-value of the HIO-algorithm was in the range between 0.8 and 0.95. A fixed support was used in these reconstruction series. In the case of the TU-Dresden logo the shape of the support is indicated in Fig. 6.5 e). The red color marks regions that are outside the support. A round support of 130 pixels and 122 pixels was used for the spiral- and siemens-star sample (Figs. 6.5 a), b) and d)), respectively. In the reconstruction shown in Fig. 6.5 c) a slightly tighter support was applied in order define more accurately the orientation of the sample. Nevertheless, a considerable improvement of the reconstructed image has not been observed for the tight support.

The reconstructions of the TU-Dresden logo and the spiral were carried out using the modified HIO-algorithm (cf. Sec. 2.7.3) in order to restrict the central pixel which is related to total electron density of the object. However, it is also sufficient to set a maximum intensity as limitation. This was pursued in the reconstructions of the siemens-star sample. In case of the reconstructions of the TU-Dresden logo and siemens-star the number of iterative cycles was 10 000 whereas for the spiral-sample only 2 000 iterations were performed. More iterative cycles did not improve the reconstructed image. Typically, it was switched between the error-reduction algorithm (ER) and the HIO-algorithm in intervals of 60 cycles ER and 40 cycles HIO.

Despite the background correction it turned out that still a relative large part of the diffraction pattern around the beam-stop is contaminated with parasitic scattering. These parts were not considered for the reconstruction, but were allowed to freely evolve during the iterative process, i.e., a circular area with a radius of 35 pixels, 40 pixels and 25 pixels was rejected in case of the siemens-star, spiral- and TU-Dresden-diffraction pattern, respectively. Typically, the use of more low frequency information from the measured diffraction pattern made the reconstruction result worse.

Reconstruction results from the deconvolved data sets presented in Fig. 6.4 b), d) and f) typically show slightly sharper details of the object. However, dramatic improvements could not be noticed which indicates that the lateral coherence length at ID10C was sufficient for this kind of samples with a size of 3 µm.

Whereas in the case of the TU-Dresden sample the reconstruction result shows very sharp and detailed features (cf. Figs. 6.5 f)) the reconstruction results of the siemens-star- and the spiral-sample clearly reveal the stagnation of the algorithm. Especially surprising were the reconstruction results of the siemens-star. In all reconstruction at-

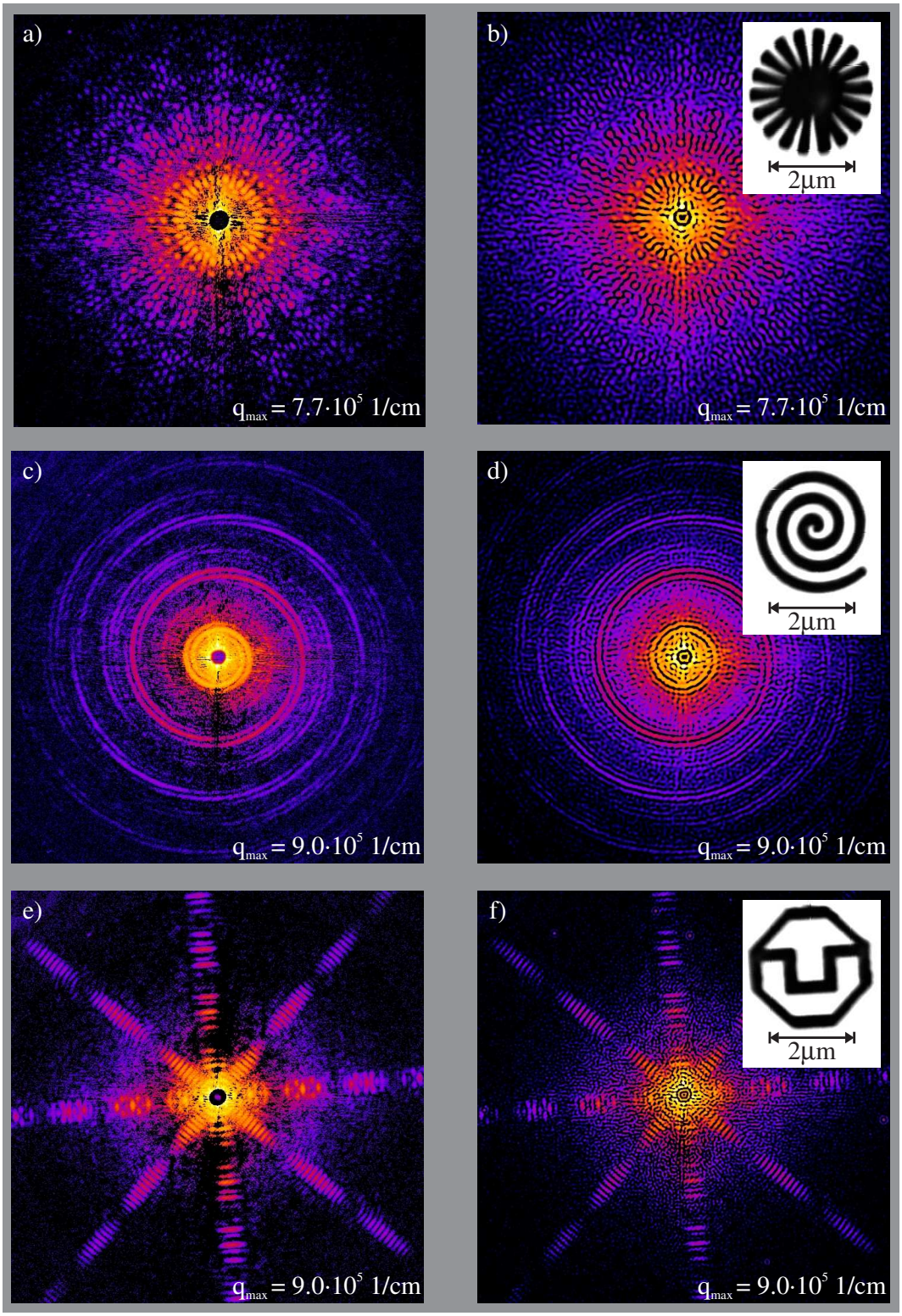

Figure 6.4: Left panel: Background corrected diffraction patterns of the lithographically prepared gold-structures. Right panel: The diffraction patterns shown in Figs. 4.9, 4.10 and 4.11 were deconvolved using the Wiener-deconvolution routine. The central part of about 30 pixels in radius was not considered in the following reconstructions. SEM-images of the 2D-samples are shown in the insets of Figs. b), d), f).

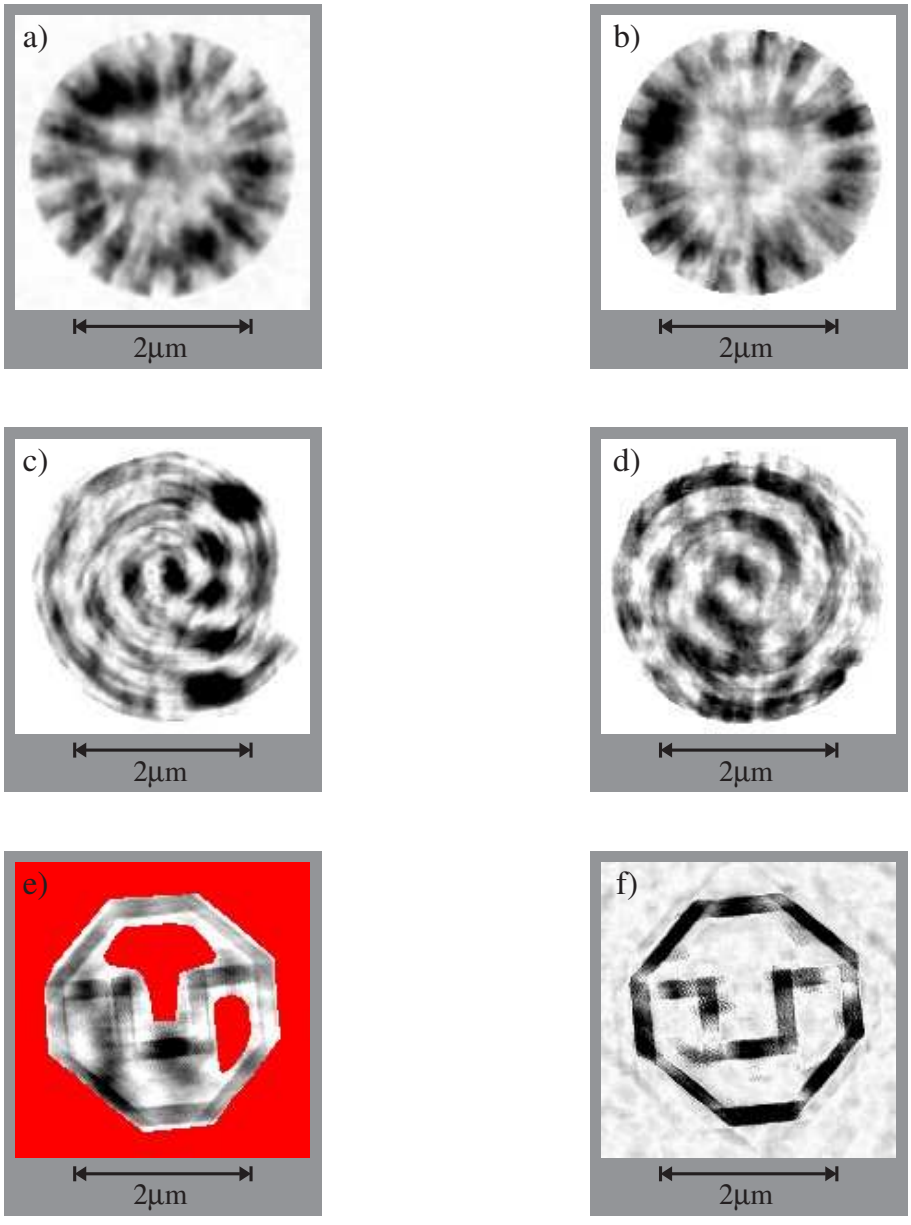

Figure 6.5: Reconstruction results from the diffraction data presented in Fig. 6.4. The left panel corresponds to the left panel of Fig. 6.4. The right panel are reconstructions from deconvolved diffraction data presented in the right panel of Fig. 6.4.

tempts the HIO-algorithm reduced the amount of electron density in the center of the object. This area is quite dense and poor of fine structure and, since the length scales involved are relatively large, the information on this region is preferentially encoded in the central part of the diffraction pattern. This artifact of the reconstruction is discussed in detail on simulated data in Sec. 6.2.3. Furthermore, the shape of the sample allows for a large variety of different possible orientations with nearly the same diffraction pattern which additionally hinders the convergence of the algorithm.
The reconstruction of the spiral-sample turned out to suffer from the same problem of missing data. Though in this case, the difficulty in reconstructing the object is mainly related to the high symmetry of the object. Simulations showed that even if only a very small amount of low frequency information is missing the probability that the HIO-algorithm stagnates in a superposition of different solutions is strongly increased.

Best reconstruction results were obtained on the TU-Dresden logo which is mainly related to the possibility to define a relatively tight support. Additionally, the possibility to include two small areas inside the object into the fixed support allows to break the symmetry between the object and its twin-image. Nevertheless, the reconstruction result from the membrane corrected diffraction pattern in Fig. 6.5 e) shows a strong variation of density on a longer length scale indicating that low spatial frequencies of the object are not well recovered by the algorithm. The most probable reason for that is the contamination of the data in the very central part of the diffraction pattern. Nevertheless, the rejection of more low q-data hinders the reconstruction and the unique way to stabilize the algorithm is by defining an even tighter support.

This approach of applying a very tight support was followed in another reconstruction attempt. It allowed to enlarge the central part of the measured diffraction pattern which is not used in the reconstruction procedure to 40 pixels in radius which corresponds to approximately four diffraction fringes. Despite the missing information the algorithm works stable and higher spatial frequencies of the object are well recovered by the algorithm. Of course, this approach can not be considered as an ab-initio reconstruction of the object but is rather a refinement in a strongly restricted parameter space.

For the following reconstruction the background-corrected diffraction pattern of the TU-Dresden logo presented in Fig. 6.4 e) was used. In Fig. 6.6 a) the evolution of the recovered electron density during the first 150 iterations is shown. Since the object is real-valued and the support is tight the convergence of the HIO-algorithm to the final solution is very fast (cf. Fig. 6.6 a)).
In Fig. 6.6 b) the final reconstruction result with a very tight support is shown. The support was chosen so tight that individual bars of the object were embedded in a frame only 4-5 pixels wider than the width of the bars of the TU-Dresden sample (cf. Fig. 6.6 c)). The definition of such a tight support requires of course previous knowledge of the object. In Fig. 6.6 d) the diffraction pattern calculated from the reconstructed object is shown. The comparison between measured and calculated data confirms a good agreement. The central part of the diffraction pattern could freely evolve during the reconstruction pro-

cess. The final result of the recovered intensity at low q-values is visualized in the inset of Fig. 6.6 d).

Another reconstruction from the same diffraction pattern and starting with the same tight support was carried out with the shrink-wrap algorithm (cf. Sec. 2.7.4). Nevertheless, the tight support was only applied during the first twenty iterations with the error-reduction algorithm. Afterwards, the support was adapted based on the current guess of the object in intervals of 20 iterative cycles. The threshold for the amplitude in real space was set to 10 % of the maximum value of the recovered electron density. This test revealed that the shrink-wrap algorithm (SW) provided with a good initial guess, i.e., with a tight support, works efficiently (cf. Fig. 6.7). Nevertheless, due to the unrestricted lower frequencies the SW-algorithm tends to decrease the support size too much. The given intensity data of higher frequency information are not sufficiently attractive to push the algorithm to perfectly recover the low frequency information. In Fig. 6.7 the final shape of the support after 20 000 iterations is shown.
Interestingly, this reconstruction method suggests to include a small region at a distance of 4.1 µm from the center of the object into the support. The small object acts as a reference scatterer which produces a finer structure in the diffraction pattern and which is oriented in lines perpendicular to the direction between sample and scatterer. The period is approximately 120 µm which corresponds to the real space distance of 4.1 µm and the variation in intensity can be recognized in the inset of Fig. 6.7 c). A detailed examination of the measured diffraction pattern confirms this intensity variation on smaller length scale than the speckle size. Additionally, the autocorrelation image of the sample, which is calculated just by a Fourier transform of the measured diffraction data, also supports the assumption that a small object might be present nearby the sample. Here, a convolved version of the sample can be noticed in the autocorrelation image (cf. Fig. 6.8).

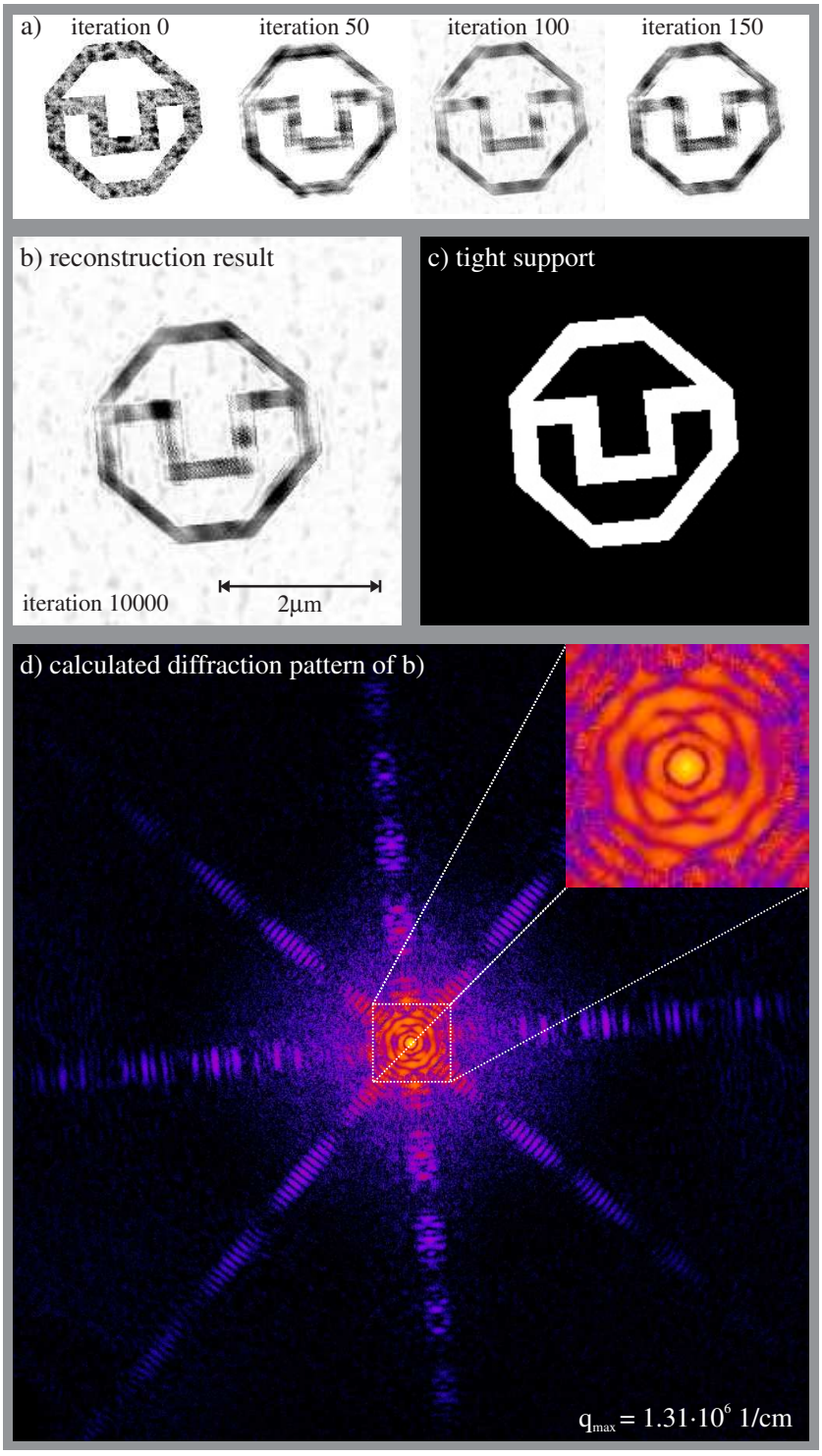

Figure 6.6: Reconstruction with a very tight support allows to increase the area of low-resolution data that is not used for the reconstruction. The size of this area is 80 pixels in diameter. a) Evolution of the electron density during the first 150 iterations. b) The final reconstruction result after 10 000 iterations. c) Very tight support applied during the iterative reconstruction. d) Diffraction pattern calculated from the reconstruction result presented in b).

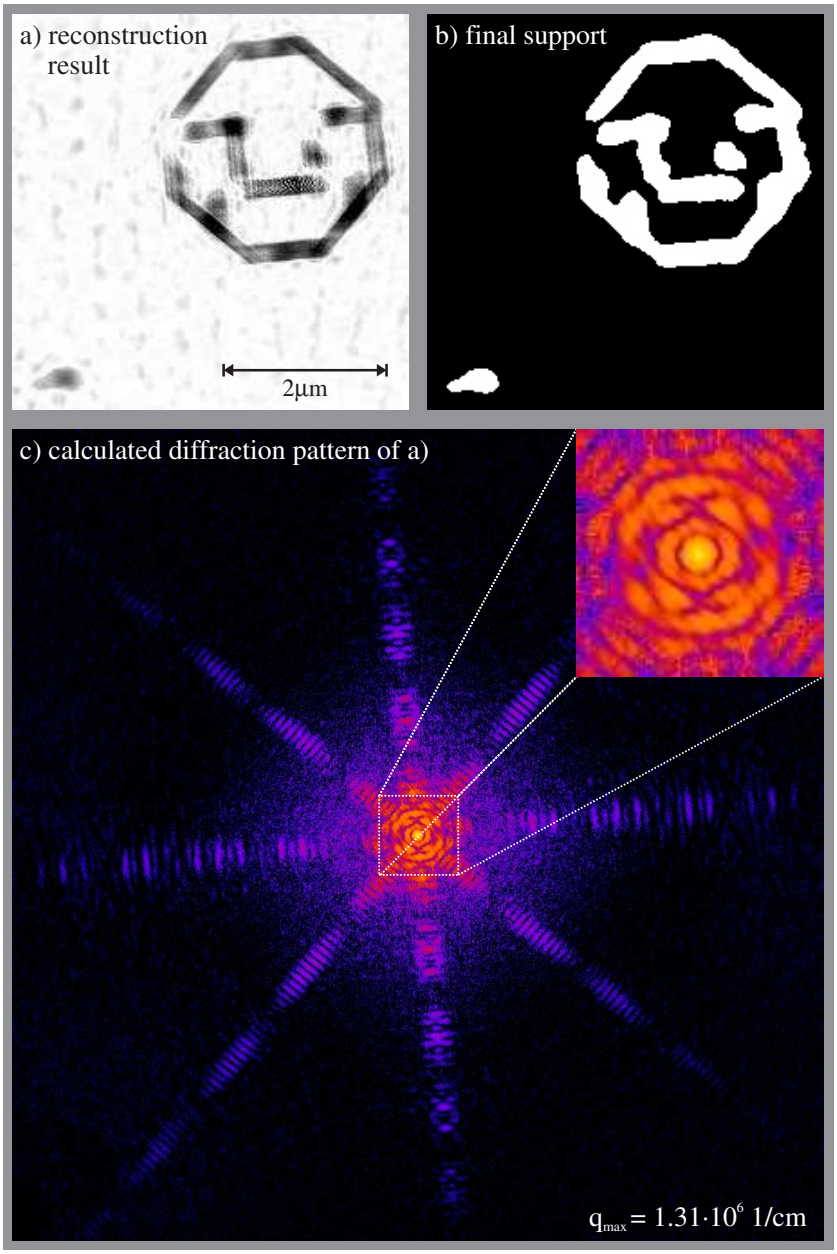

Figure 6.7: a) Result of a reconstruction with the shrink-wrap algorithm. The support at the beginning was the same as in the previous reconstruction but was allowed to adapt to the current guess of the object. b) Final support after 10 000 iterations enlarged by a small area in the lower left corner. The distance between sample and reference scatterer is approximately 4.1 µm giving rise to a fine oscillation of the intensity with a spatial frequency of 120 µm at the detector position. The existence of this finer oscillations can be recognized in the measured diffraction pattern. c) Calculated diffraction pattern of the inverted image shown in a).

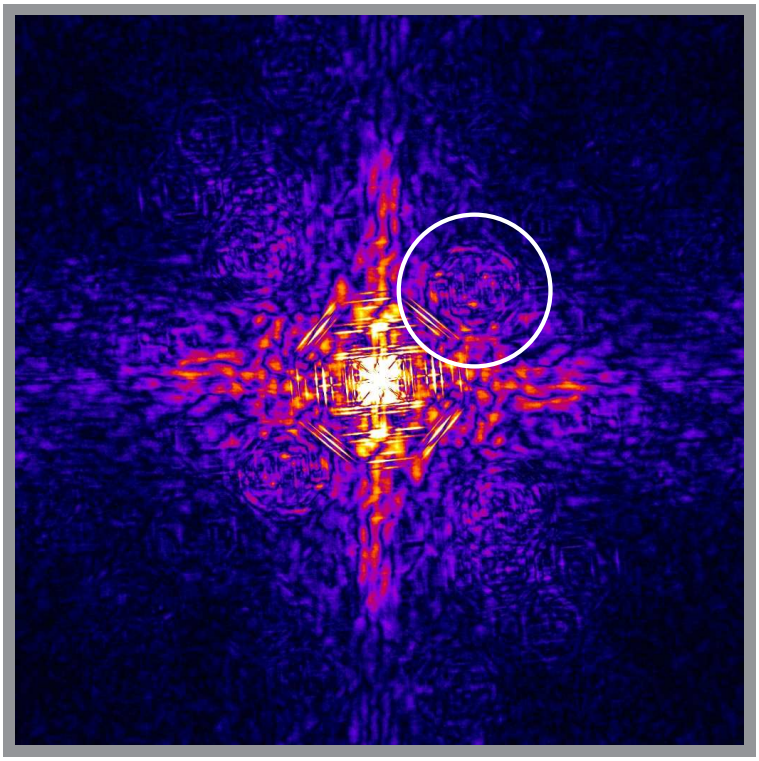

Figure 6.8: Autocorrelation image of the object obtained from the TU-Dresden logo diffraction pattern shown in Fig. 6.4 e). A careful inspection reveals that a reference scatterer was present nearby the Au-sample. It is indicated by a white circle.

6.2.3 Missing Low Frequency Data

The comparison of measured and calculated diffraction data reveals that in the central part of the diffraction pattern a region of approximately $3-4$ times the speckle size could not be measured properly due to slit scattering and a certain contribution of third harmonic photons. This means that all information about the distribution of the electron density corresponding to $\Delta q < 1.18 \cdot 10^{-5}\,1/\mathrm{cm}$, i.e., length scales larger than 530 nm, is lost which makes the phase retrieval considerably more difficult. In these areas the HIO-algorithm has to recover besides the phase additionally the correct amplitude which turns out to be especially difficult for the siemens-star- and the spiral-sample as will be explained in this section. The diffraction pattern of the siemens-star (cf. Fig. 6.9 a)) is used for reconstruction tests from incomplete diffraction data.

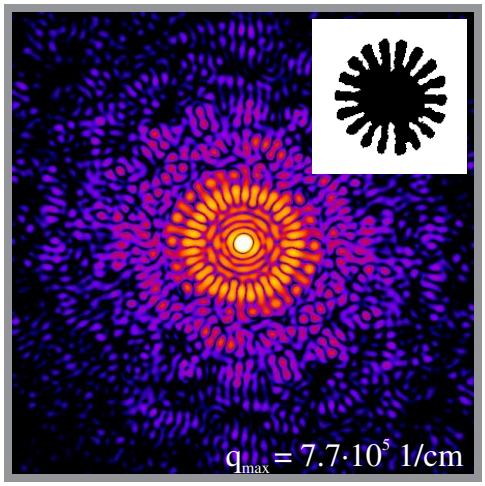

(a) Siemens-star-sample.

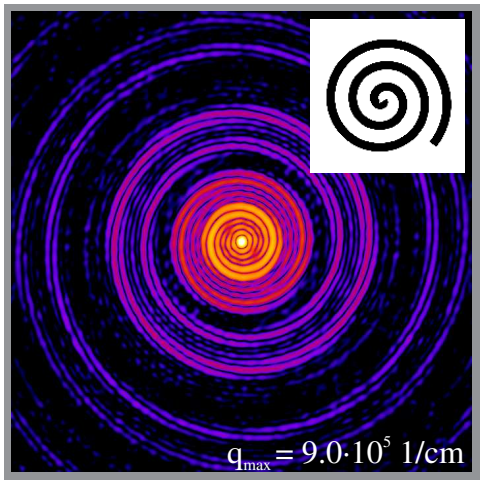

(b) Spiral-sample

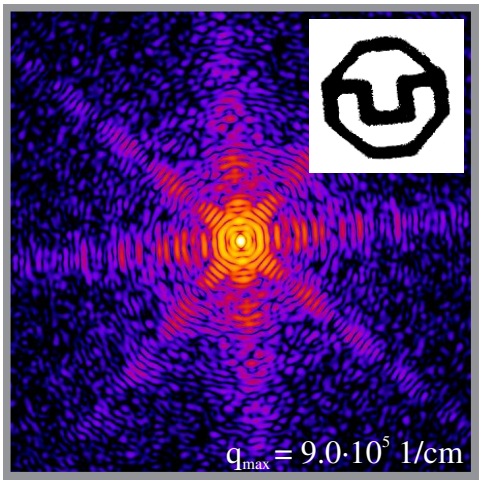

(c) TU-logo-sample.

Figure 6.9: Different diffraction patterns calculated SEM-images with lower resolution.

Due to the round shape of siemens-star- and spiral-sample, the definition of a tight support which roughly provides beforehand parts of low frequency information and breaks internal symmetries of the object is difficult. Therefore, the lost low resolution speckles are completely unconstrained. The number of solutions which have different orientations of the sample and which are in good agreement with the measured data at larger q-values is very large. The competition between these solutions results in a high probability that the algorithm stagnates in a local minimum.

Similar experiences were reported in [Sha05] in the context of the reconstruction of an unstained yeast cell using soft x rays with energy of 750 eV. Nevertheless, in that work the loss of low frequency information was much smaller, i.e., about two diffraction orders, and the problem could be solved by choosing the two least constraint modes of the corresponding unknown amplitudes such as to minimize the variance of the object. Thus, this approach produces a continuous diffraction pattern and additionally keeps the introduction of sharp features which are not related to the measured data small.
Unfortunately, the loss of low frequency information is much larger for the diffraction data presented in this work and, therefore, the proposed method could not be applied. The unique possibility to support the HIO-algorithm in order to find the correct amplitudes at low q-values is by defining a tight support.

In order to learn about the difficulties in recovering this information a series of HIO-reconstructions was carried out on the calculated data of Fig. 6.9(a). A circular area of 20 pixels in the center of the diffraction pattern of the siemens-star was omitted and the algorithm had to recover the lost speckles. The actual size of this area is indicated in Fig. 6.10 a) by a white circle. Although this region of reciprocal space is quite small, i.e., only about 2 fringes, the algorithm has difficulties to reconstruct the object. In Fig. 6.10 the results of 8 different reconstruction attempts carried out always with identical reconstruction parameters, but different starting phases, are presented (cf. Fig. 6.10 a)-h)). In Fig. 6.10 i) the object sought-after is given. It is highlighted by a red frame.
The first remarkable conclusion from this test series is the large number of different reconstruction results. Although the amount of unrestricted low frequency speckles is only two diffraction orders there is a large degree of freedom in setting the low-resolution data. Interestingly, all reconstructions where the central area of the siemens-star sample is completely filled with material are distinguishable from the other results through the wider central diffraction peak. This can easily be understood since the central part of the object does not contain high-frequency information and, therefore, Fourier-components close to the central peak become large. Thus, for this kind of sample the low-resolution data are especially important for the recovery of the central flat region of the object.
Finally, only in one of 10 reconstruction trials the correct solution was nearly found. Unfortunately, also this reconstruction stagnate at the end due to the twin-image problem (cf. Fig. 6.10 h)).
The same reconstruction series was carried out with even one more diffraction speckle hidden. In this case, all of the reconstructed images show the empty region in the center of the object and not one reconstruction attempt lead to the correct result.

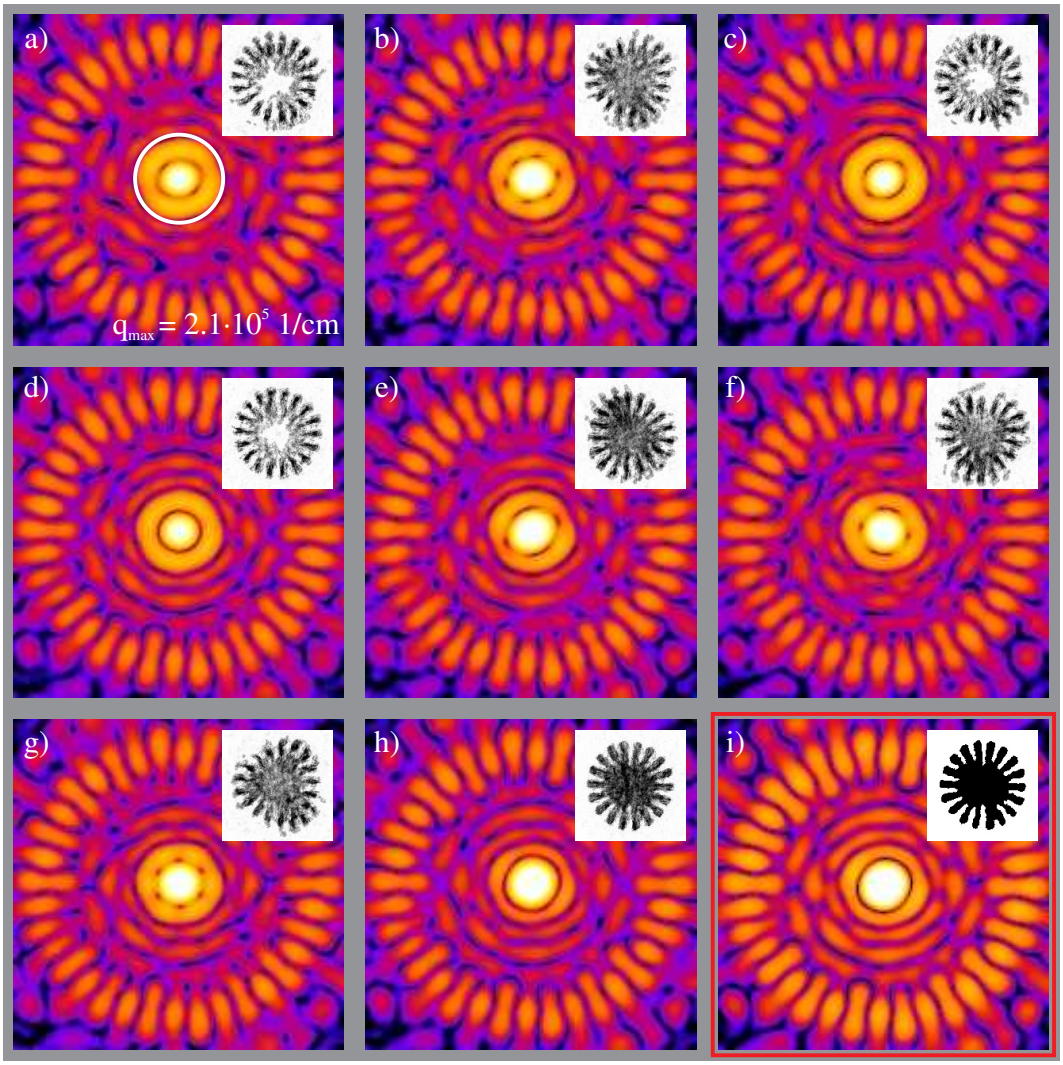

Figure 6.10: Series of HIO-reconstructions where the central area of the calculated data with a radius of 20 pixels indicated by a white circle in image a) was hidden. The correct result is presented in image i). From 10 trials only one reconstruction found almost the correct object (image h)).

Since the lack of low-frequency data is even much larger in the case of the measured data than in this simulation, the results of Sec. 6.2.2 become much more comprehensible. A large amount of scattering signal related to the central area of the object could not be measured and even the shrink-wrap-method, which often turns out to be advantageous in recovering this information, can not help to define a suitable support for this kind of object.

In conclusion, in case of a generic object it turns out to be very important that

all speckles at low q-values are accurately measured. Only then the algorithm works reliably and the convergence of the algorithm towards the correct solution is guaranteed. Especially in the case of the siemens-star even the position of the first minimum around the central peak contains very important information.

6.2.4 Inhomogeneous Illumination

A further aspect that needs to be considered in the context of modified low-frequency diffraction data is the structure of the complex wave-field incident upon a sample. Obviously, in the experiment optical components such as the monochromator crystals modify the wavefront in a certain way leading to the introduction of phase shifts in the wavefront. This situation was observed at beamline ID10C. Since the monochromator was located quite close to the sample position imperfections of the monochromator crystals create under coherent illumination a specific speckle pattern (cf. Fig. 6.11).

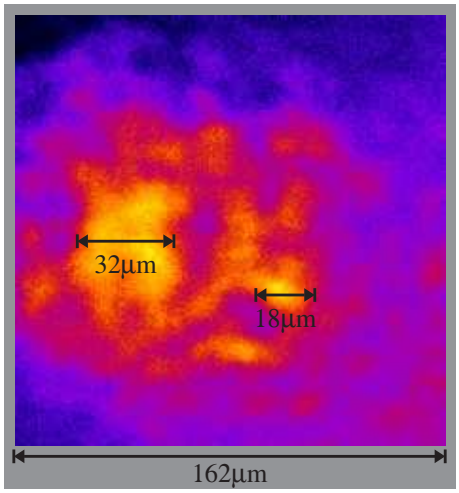

Figure 6.11: Intensity variation at the sample position measured with the high-resolution detector with 20×-magnification. The origin of the speckles is related to the imperfections of the monochromator crystals. The typical speckle size is about 15 µm.

Moving the monochromator crystals relative to the x-ray beam changed the speckle pattern and certain features of the intensity distribution appeared and disappeared in a reproducible way. The distribution of the illumination has a phase variation that can not be neglected and shows a typical feature size of about 15 µm.

The influence of such an illumination function can be simulated by introducing a random phase plate in the x-ray beam. The numerical routine calculates the phase shift that would have been created by a carbon layer with a variation in thickness of 10 µm. The spatial frequency of the random lateral variation of the thickness can be defined. The resulting wavefront in the sample plane is illustrated in Fig. 6.12 a). The propagation of this wave-field to the diffraction plane gives the result as presented in Fig. 6.12 b).

Obviously, since the typical spatial frequency range of the illumination function is small, primarily small q-values are affected and a broad scattering background can be observed in the central part of the simulated diffraction pattern (Fig. 6.12 b)).

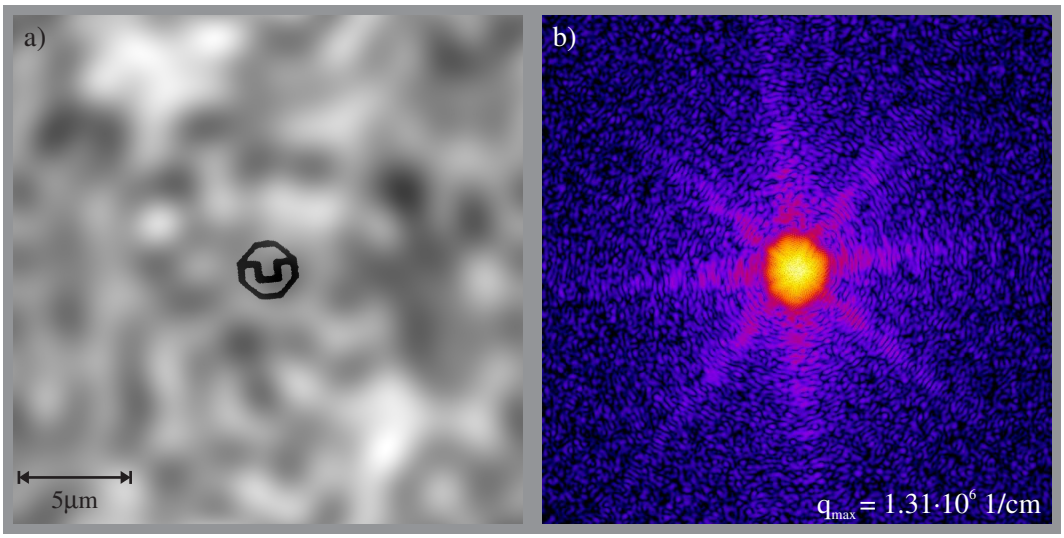

Figure 6.12: a) Simulated wave-field with certain phase variation. b) The inhomogeneous illumination smears low frequency information.

Although the size of the illumination is much larger in the simulation than in the real experiment it emphasizes the importance of a flat x-ray beam for CXD-experiments. In our experiment at ID10C the speckle size at the sample position could be increased by closing a pair of slits just in front of the monochromator. The smaller illumination of the monochromator crystals produces larger speckles and by searching a suitable position of the beam-defining slits an almost flat region of the x-ray beam could be selected. In this way effects of an inhomogeneous illumination could be reduced.

6.3 Discussion

In this chapter it was demonstrated that the inversion of diffraction patterns collected from lithographically prepared gold structures is feasible if previous knowledge of the object of interest is available. However, new experimental difficulties were encountered when using hard x rays with a photon energy of about 8 keV. It involves mainly the correct measurement of low-resolution data and the visibility of diffraction fringes. Both points make the reconstruction of the object difficult and prevent until now a quantitative reconstruction of the electron density.
During the iterative reconstruction process the low resolution information is not restricted in reciprocal space giving the reconstruction algorithm a large degree of freedom to define low resolution speckles. The recovered intensity is mostly incorrect leading to the stagnation of the algorithm in local minima. The only way to support the al-

gorithm in the recovery of this information is by introduction of a tight support if it is available. This approach was followed using the data of the TU-Dresden logo. The tight support was determined from a lower resolution SEM-image of the object. In some cases, depending on the shape of the 2D-object, the shrink-wrap method turns out to be advantageous for the recovery of the low-resolution information. However, for a generic object it is generally necessary that the complete diffraction pattern including the first diffraction orders is properly measured.

The second implication due to partial coherence effects is more difficult to characterize experimentally. It depends strongly on the specific beamline layout and the quality of the optical components that are used upstream of the sample. While the influence of partial coherence was less important in the results of the experiment carried out at ID10C a correction for this effect was certainly necessary for the data collected at ID01. It may further be mentioned that a smearing of the diffraction pattern can also be caused by slight movements of optical components during the measurement.

7 Summary and Outlook

Coherent x-ray diffraction imaging has been proven to work efficiently in the soft x-ray-regime and various successful phase reconstructions from biological samples, three-dimensional structures and even reconstruction from a diffraction pattern produced by a single VUV-pulse were reported in various contributions during the last years, see e.g. [Thi06, Cha06a, Cha06b]. The extension of the CXDI-method to the harder x-ray regime is a logical consequence since only at these wavelengths structure determination with very high resolution may be achievable. This is especially interesting with regard to upcoming x-ray sources of the fourth generation which are supposed to deliver a coherent and intense hard x-ray beam. The main focus of this thesis was on the investigation of the CXDI-method in the hard x-ray regime, i.e., using photons with an energy larger than 6 keV.

Since absorption and scattering in air would substantially reduce the quality of the data it was necessary in a first step to build a vacuum chamber which is especially adapted to the requirements of the CXDI-method.
One of the main difficulties encountered in the experiment was the cleaning of the incoming x-ray beam from parasitic scattering due to optical components upstream. It was tried to reduce this parasitic scattering close to the beam-stop by introducing two pairs of guard slits with especially polished blades after the beam-defining slits. The exact positioning of the blades to suppress the scattering of the beam-defining slits turned out to be very important in the experiment. The simulations presented in Sec. 5.1 confirmed that it is especially favorable to position the edges of the blades into the minima of the diffraction pattern of the beam-defining slits very close upstream the sample. The implementation of a scintillator-based high-resolution detector for the purpose to image the incoming wave front at the sample position proved very valuable to control the exact position of the slit blades with micrometer-accuracy during the measurement (cf. Sec. 3.2.3). The lateral resolution of this detector is approximately $2 - 3\,\mu$m.
Another important experimental requirement is the positioning of the sample with very high accuracy which is in particular valid for the ptychographic phase retrieval method where the sample has to be moved through the x-ray beam in well defined steps. Theoretical results predict that the scanning of the sample needs to be done with the same accuracy as the resolution expected to be recovered from the individual diffraction patterns (cf. Sec. 5.5). The characterization of the different technical components and their implementation in the experimental setup was presented in Chap. 3.

During this work, a series of diffraction patterns from lithographically prepared two-dimensional gold structures was successfully recorded at beamlines ID01 and ID10C at

the ESRF. The analysis of the data and the following reconstruction using the Hybrid-Input-Output algorithm (HIO) revealed that the effects of missing low-resolution data and partial coherence are the main factors that can impair a successful reconstruction from measured data only (Chap. 6). Thereupon, these effects were thoroughly investigated in a series of reconstructions with artificially modified simulated data in order to quantify their influence in iterative phase retrieval.

The speckle size of the diffraction pattern scales with the wavelength and, at harder energies, typically more low resolution information which is imprinted at low diffraction angles of the diffraction pattern is lost due to background scattering in this area of reciprocal space. This factor of missing data at low q-values introduces an additional degree of freedom and, since the low-frequency modes of the object are unrestricted, the probability that the HIO-algorithm gets trapped in local minima of the search space is strongly enhanced. However, it has been observed that, depending also on the geometrical shape of the object, reconstruction from incomplete data may be possible using additionally the shrink-wrap method (Sec. 2.7.4). The shrinking of the support during iterative phase retrieval may help in some cases to accurately recover low resolution diffraction data without introduction of calculated data from SEM-images with lower resolution. However, the results show that for a generic object it is necessary to measure the complete diffraction pattern including the very first diffraction orders. They define the overall shape of the object and are very important for the successful reconstruction of the object. The influence of missing low-resolution data is discussed in Sec. 6.2.3.
The CXDI-method requires that the object is coherently illuminated which also becomes more difficult at higher photon energies. The lateral coherence length at third generation x-ray sources scales with the wavelength of the radiation. For this reason only small objects of a few micrometers in size could be investigated in the experiment. The reduced visibility of diffraction fringes due to partial coherence effects is not correctly expressed by current phase retrieval algorithms since these algorithms are based on the direct application of the forward and inverse Fourier-transform and do not consider convolution effects. Even a slight smearing of the diffraction pattern produces strong artifacts in the reconstruction result. Effects of partial coherence are certainly main limitation factors of the CXDI-method. This topic has been discussed in Sec. 5.3 and Sec. 6.1.

Finally, the number of incident photons available in the experiment defines the achievable resolution of the inverted image and different simulations presented in Sec. 5.2 have been addressed to this topic. Additionally, experimental data of a cluster of gold-spheres were analyzed with regard to photon flux. Due to the weak interaction of x rays with matter the scattered intensity at large q-values is very low. Typically, the intensity decrease towards larger q-values shows a q^{-4}-power law behavior which turned out to be very critical with regard to very high resolution imaging (cf. Sec. 4.3). Future studies in this field should also focus on biological samples and radiation damage.

During this work an alternative algorithm for phase retrieval has been developed. This so-called genetic algorithm is a pure search algorithm and is based on the principles of

evolution. It has the main advantage that only the numerical implementation of the forward propagation of the wave field from the sample to the diffraction plane is required and partial coherence effects and wavefront distortions can be introduced in the model. The forward propagation is applied for the calculation of the so-called fitness of the population members which is used to distinguish between better and worse members. Its working principle is simply based on stochastics and finally, only the best members, i.e., the ones that fulfill the necessary condition to have the correct Fourier-amplitude, survive in analogy to the real evolution. In comparison to other phase retrieval algorithms the convergence of the genetic algorithm is much slower and especially the fine structures of the object are very difficult to recover. Nevertheless, at least for inverse problems of lower dimensionality it is a very interesting alternative to state-of-the-art phase retrieval methods. Further development has to be done in order to improve the convergence of the algorithm. Different reconstruction results on simulated data are presented in Sec. 5.4.

As a main result of this work the ptychographic reconstruction method which was introduced in Sec. 2.7.5 theoretically proves to be the most promising method for x-ray imaging with high-resolution. Different simulations show that the convergence of the algorithm is very fast and even complex-valued objects are easily reconstructed within a few hundreds of iterations. Phase retrieval of a complex object from a single diffraction pattern is much more challenging and the support of the object has to be known very accurately. Since in ptychography the incoming illumination wave field defines the area of the sample that contributes to an individual diffraction pattern it is possible to image extended objects. In principle, the illumination function acts as the compact support which is used in other phase retrieval algorithms. Nevertheless, for a successful reconstruction it is necessary to accurately know the complex incident wavefield as well as the position of the illuminated area with a similar accuracy as is desired to achieve in the inverted image. Different simulation results devoted to this topic were presented in Sec. 5.5. The precise knowledge of the illumination is the main limiting factor. However, it is conceivable to extend the algorithm that it refines besides the phases of the diffraction patterns also the position and shape of the illumination function. This is a very promising topic for future investigations.
First experimental steps to test the method were carried out at the ESRF and a series of diffraction patterns with overlapping illumination function were recorded. But due to the mentioned advanced requirements of the knowledge of the illumination function the reconstruction has not worked yet. Nevertheless, it is certainly worth to investigate the method further and resolutions of the order of 10 nm or slightly lower might be achievable in the future.

A Software Utilities

A series of software tools related to phase retrieval and image processing has been developed during this thesis. Most of these are part of a C++-program so-called "tomo". After the start of the program in a terminal application a menu with an overview of different available programs can be displayed on screen by typing "-1". Each sub-program is then selectable by a certain number. In the following a short description of some of these sub-programs is given. The file-extension ".edf" or ".bin" refers to the binary file format developed at the ESRF.

106: Routine to convert edf-files to tif-files (16bits or 32bits).

114: Extraction of line profiles from edf-images. The start- and end-point can be set arbitrarily. Points on the connecting line are linearly interpolated. The output is written to an ASCII-file.

116: Subtraction of the median from an image.

117: Conversion of tif-files (16bits or 32bits) to binary format.

118: Adds a series of images and writes the sum and the mean image into binary files.

119: Applies a round mask on the image. The central pixel as well as a certain radius has to provided. The area inside, or alternatively outside, this circle will be set to zero. A transition area can be introduced by defining a certain FWHM-value. The larger this value the smoother is the transition area.

120: Applies an arbitrary mask on the image. The mask-image has to provided by an ASCII-file. Areas inside the mask will be set to zero.

121: Adds two images with arbitrary dimensions. The common pixel of the upper left corner has to be defined.

122: Turn image around a specified point. Linear interpolation is used.

123: Multiply image with a constant factor.

126: Crop image around a specified point.

127: Iterative deconvolution of an image using a maximum entropy method. The convolution function is assumed to be Gaussian and the FWHM-values in x- and y-direction have to be provided for this deconvolution routine.

129: Merge a series of diffraction patterns to one image.
This routine is especially useful if several diffraction patterns with different sizes of the beam-stop were recorded. The first image provided will fill the central part of the final merged image whereas the data of further images successively fill outer areas. The transition region from one image to the next has to be specified by a certain radius value. In order to guarantee a smooth transition between neighboring areas originating from different images a certain weighting function with the shape of a radial step function having a certain sharpness of the edge is multiplied on the image. The result is added to the subsequent image which was multiplied before with the inverted step function. The sharpness of the transition region is defined by a certain FWHM-value. A scaling factor can be provided for each image which serves to correct the different diffraction patterns for varying exposure times.

257: Calculate transmission function of an arbitrary two-dimensional thin object.
The shape of the object has to be provided by an ASCII-file containing values from 0 to 255. This grayscale image is converted to specific thickness values of the material. From the thickness of the material the complex transmission function of the 2D-object is calculated. Further necessary parameters are the size of the 2D-object, the pixel size, the atomic number of the material, the maximum thickness of the material and the photon energy.

800: Calculates the Fraunhofer diffraction pattern from the transmission function.
The effect of partial coherence can be introduced by convolution of the diffraction pattern with a Gaussian function. By defining a certain incoming photon flux the effect of Poisson-noise can be simulated.

803: Implementation of the genetic algorithm.
Main parameters that have to be given are the population size, the number of iterations per generation, the probability of crossover and mutation, the support area and in case that the diffraction pattern is only partially coherent the FWHM-values of Gaussian convolution.

805: HIO-algorithm.
A series of parameters and input data has to be provided for this numerical implementation. It mainly concerns the illumination function, the support region, the areas of the diffraction pattern which are not restricted during the reconstruction process, the number of subsequent error-reduction- and HIO-cycles, and specific parameters used in HIO and shrink-wrap (cf. Sec. 2.7.3).

806: Calculation of the diffraction pattern of a real-valued object.

807: Creates a number of artificial diffraction patterns that can be used for testing purposes of the ptychographic-reconstruction. The illumination function as well as a table defining the offset between different illumination areas (ASCII-file with two columns with offset in x- and y-direction in millimeters) has to be provided.

808: Calculates the autocorrelation image of a diffraction pattern.

809: Find center of diffraction pattern and symmetrize it.
This routine is only applicable if the diffraction pattern has a center-symmetry. In order to help the program to find the center of the diffraction pattern it is necessary to provide a guess of the central pixel. Based on the assumption that this pixel is the central one the symmetric diffraction pattern is determined and the correlation between these images is calculated. The same procedure is done for a number of pixels around the guessed central pixel. The pixel inside this area yielding the highest degree of correlation is assumed to be the actual central pixel of the diffraction pattern.

Once the central pixel is known, the diffraction pattern can be symmetrized. The numerical implementation is done by comparing the intensity values of all pixel pairs. Herein, one pair consists of a certain pixel and its symmetric equivalent one. The routine calculates the real photon flux from the measured ADC-units. It is done by multiplication of the measured diffraction pattern with a certain conversion factor defining the relation between photon flux and ADC-units. For the directly-illuminated Princeton CCD used in experiments the conversion factor is about 800 counts per photon at 8 keV photon energy. Afterwards, it determines the standard deviation $\sigma = \sqrt{I_{\text{low}}}$ from the lower intensity value I_{low} on the basis of Poisson-statistics. Using this value the routine checks if the intensity of the second pixel is smaller than $I_{\text{low}} + 3\sigma$. If this is the case, then the measured values are considered to be in good agreement and the intensity is set in both pixels to the mean value. If this condition is not fulfilled the intensity of the pixel with larger intensity is rejected and is set to the value of the lower one. Obviously, this procedure has to be done for all pixel pairs and of course, it only improves the quality of the diffraction data if at least one pixel of the pair is not contaminated with parasitic scattering.

811: Implementation of the Ptychography-algorithm (Rodenburg-Faulkner).
Input data are the diffraction patterns recorded from different illuminated areas and a table defining the lateral offset between them. The diffraction patterns must have filenames of the form "*diffXXXX.bin", where X is a replacement character for some number. It is preferable that the files are sorted with continuously ascending number. The first image read from the hard disk will be associated to the offset values defined in the first line of the offset-table, etc.. Further necessary parameters were introduced in Sec. 2.7.5.

831: Integration of intensity of a diffraction pattern at constant $|q|$. The output is an ASCII-file providing the mean-intensity as function of $|q|$. This is useful to plot the power spectrum of a diffraction pattern.

B Stepper Motor Parameters

The stepper motors used in the experimental setup are controlled via Sincos-power stages (Phytron)[SIN]. The device was driven in mode 6, i.e., each full step is divided into 20 sub-steps (sinusoidal phase). Various parameters like maximum current and conversion factor have to be defined for each motor. For example a conversion factor a -4000 for the samx-motor means that 4000 steps correspond to a movement of 1 mm. The sign defines the direction of the linear movement. Since the Sincos-power stage is driven in mode 6 this corresponds to 200 full steps per millimeter. Furthermore, 200 full steps correspond in this case to a single revolution of the stepper motor and consequently, the slope of the spindle driving the linear stage is 1 mm per revolution. Further parameters are the slew rate and the backlash. These values are summarized for each motor in table B.1.

Motor #	Motor alias	Max. I [A]	Conversion	Slew rate	Backl. (mm)
mot1	samx	1.2	-4000	4000	0.2
mot2	samy	1.2	-4000	4000	0.2
mot3	samz	2.5	200000	10000	0.05
mot4	ccdy	2.5	-4000	4000	0.1
mot5	ccdz	2.5	-4000	4000	0.1
mot6	bsy	2.5	2000	4000	0.1
mot7	bsz	2.5	200000	10000	0.1
mot8	sl2x	2.5	-4000	4000	0.1
mot9	sl1b	0.6	-8000	8000	0
mot10	sl1t	0.6	8000	8000	0
mot11	sl1l	0.6	-8000	8000	0
mot12	sl1r	0.6	8000	8000	0

Table B.1: Motor Calibration (CXD-Experiment)

The motors samx, samy and samz are used for the positioning of the sample and the motors ccdy and ccdz allow to move the camera optics in a plane perpendicular to the x-ray beam. Motors bsy and bsz control the position of the beam-stop and sl2x is used to move the last guard slit in beam-direction. The last set of stepper motors with alias sl1* is used to control the slit system from Advanced Design Consulting, USA.

Acronyms

CXDI coherent x-ray diffractive imaging

ESRF European Synchrotron Radiation Facility

APS Advanced Photon Source

SPring-8 Super Photon Ring-8

XFEL X-Ray Free Electron Laser

LCLS Linac Coherent Light Source

BM bending magnet

ID insertion device

Bibliography

[ADC] `http://www.adc9001.com`.

[AN01] J. Als-Nielsen and D. McMorrow. *Elements of Modern X-Ray Physics*. John Wiley & Sons Ltd, New York (2001).

[Bal04] K. Balewski, W. Brefeld, W. Decking, H. Franz, R. Röhlsberger, and E. Weckert. *PETRA III: A Low Emittance Synchrotron Radiation Source*. Technical report, DESY, Hamburg (2004).

[Bar84] R. Barakat and G. Newsam. *Necessary conditions for a unique solution to two-dimensional phase recovery*. J. Math. Phys. **25**, 3190–3193 (1984).

[Bar07] A. Barty, S. Marchesini, H. N. Chapman, C. Cui, M. R. Howells, D. A. Shapiro, A. M. Minor, J. C. H. Spence, U. Weierstall, J. Ilavsky, A. Noy, S. P. Hau-Riege, A. B. Artyukhin, T. Baumann, T. Willey, J. Stolken, T. van Buuren, and J. H. Kinney. *Three-dimensional coherent X-ray diffraction imaging of a ceramic nanofoam: determination of structural deformation mechanisms* (2007).
URL `http://www.citebase.org/abstract?id=oai:arXiv.org:0708.4035`

[Bat82] R. H. T. Bates. *Fourier phase problems are uniquely solvable in more than one dimension. I. Underlying theory*. Optik **61**, 247–262 (1982).

[Ben05] B. Benner. *Imaging with Parabolic Refractive X-Ray Lenses*. Ph.D. thesis, Aachen University (RWTH) (2005).

[BER] Center for X-Ray Optics, `http://www.cxro.lbl.gov`.

[Bor99] M. Born and E. Wolf. *Principles of Optics*. Cambridge University Press, Cambridge (1999).

[Cha95] C. T. Chantler. *Theoretical Form Factor, Attenuation and Scattering Tabulation for $Z = 1 - 92$ from $E = 1 - 10\,\mathrm{eV}$ to $E = 0.4, 10.0\,\mathrm{MeV}$*. Journal of Physical and Chemical Reference Data **24**, 71 (1995).

[Cha05] W. Chao, B. D. Harteneck, J. A. Liddle, E. H. Anderson, and D. T. Attwood. *Soft X-ray microscopy at a spatial resolution better than 15 nm*. Nature **435**, 1210–1213 (2005).

[Cha06a] H. N. Chapman. *Femtosecond diffractive imaging with a soft-X-ray free-electron laser*. Nature Physics **2**, 839–843 (2006).

[Cha06b] H. N. Chapman, A. Barty, S. Marchesini, A. Noy, S. P. Hau-Riege, C. Cui, M. R. Howells, R. Rosen, H. He, J. C. H. Spence, U. Weierstall, T. Beetz, C. Jacobsen, and D. Shapiro. *High-resolution ab initio three-dimensional x-ray diffraction microscopy*. J. Opt. Soc. Am. A **23**, 1179–1200 (2006).

[Cla04] J. A. Clarke. *The Science and Technology of Undulators and Wigglers*. Oxford University Press, Oxford (2004).

[Els03] V. Elser. *Phase retrieval by iterated projections*. J. Opt. Soc. Am. A **20**, 40–55 (2003).

[Els07] V. Elser, I. Rankenburg, and P. Thibault. *Searching with iterated maps*. PNAS **104**, 418–423 (2007).

[ESR07] ESRF-Highlights 2006*, Facts and Figures*, p. 122 (2007).

[Fau04] H. M. L. Faulkner and J. M. Rodenburg. *Movable Aperture Lensless Transmission Microscopy: A Novel Phase Retrieval Algorithm*. Phys. Rev. Lett. **93**, 023903 (2004).

[Fau05] H. M. L. Faulkner and J. M. Rodenburg. *Error tolerance of an iterative phase retrieval algorithm for moveable illumination microscopy*. Ultramicroscopy **103**, 153–164 (2005).

[Fie78] J. R. Fienup. *Reconstruction of an object from the modulus of its Fourier transform*. Opt. Lett. **3**, 27–29 (1978).

[Fie82] J. R. Fienup. *Phase retrieval algorithms: a comparison*. Applied Optics **21**, 2758–2769 (1982).

[Fie86] J. R. Fienup and C. C. Wackerman. *Phase-retrieval stagnation problems and solutions*. J. Opt. Soc. Am. A **3**, 1897–1907 (1986).

[Fie87] J. R. Fienup. *Reconstruction of a complex-valued object from the modulus of its Fourier transform using a support constraint*. J. Opt. Soc. Am. A **4**, 118–123 (1987).

[Fie90] J. R. Fienup and A. M. Kowalczyk. *Phase retrieval for a complex-valued object by using a low-resolution image*. J. Opt. Soc. Am. A **7**, 450–458 (1990).

[Flü04] J. Flügge. *Entwurf und Konstruktion einer hochauflösenden 2D Röntgenkamera*. Diplomarbeit, Technische Fachhochschule Wildau (2004).

[Fri82] W. R. Fright and R. H. T. Bates. *Fourier phase problems are uniquely solvable in more than one dimension. III: Computational examples for two dimensions*. Optik **62**, 219–230 (1982).

[Gar82] K. L. Garden and R. H. T. Bates. *Fourier phase problems are uniquely solvable in more than one dimension. II: One-dimensional considerations*. Optik **62**, 131–142 (1982).

[Ger72] R. W. Gerchberg and W. O. Saxton. *A practical algorithm for the determination of phase from image and diffraction plane pictures*. Optik **35**, 237–246 (1972).

[Goo85] J. W. Goodman. *Statistical Optics*. John Wiley & Sons, Inc., New York (1985).

[Gün03] T. F. Günzler. *Element-specific X-ray Fluorescence Microtomography*. Ph.D. thesis, Aachen University (RWTH) (2003).

[Heg70] R. Hegerl and W. Hoppe. *Dynamische Theorie der Kristallstrukturanalyse durch Elektronenbeugung im inhomogenen Primärstrahlwellenfeld.* Ber. Bunsenges. phys. Chem. **74**, 1148–1154 (1970).

[Hel94] S. W. Hell and J. Wichmann. *Breaking the diffraction resolution limit by stimulated emission: stimulated-emission-depletion fluorescence microscopy.* Opt. Lett. **19**, 780–782 (1994).

[Hop69a] W. Hoppe. *Beugung im Inhomogenen Primärstrahlwellenfeld. I. Prinzip einer Phasenmessung von Elektronenbeugungsinterferenzen.* Acta Cryst. A **25**, 495–501 (1969).

[Hop69b] W. Hoppe and G. Strube. *Beugung im Inhomogenen Primärstrahlwellenfeld. II. Lichtoptische Analogievesuche zur Phasenmessung von Gitterinterferenzen.* Acta Cryst. A **25**, 502–507 (1969).

[Jac82] J. D. Jackson. *Klassische Elektrodynamik.* de Gruyter, Berlin (1982).

[Jac99] C. Jacobsen. *Soft x-ray microscopy.* Trends in Cell Biology **9**, 44–47 (1999).

[Jef07] K. Jefimovs, O. Bunk, F. Pfeiffer, D. Grollimund, J. F. van der Veen, and C. David. *Fabrication of Fresnel zone plates for hard X-rays.* Microelectronic Engineering **84**, 1467–1470 (2007).

[Jia08] H. Jiang, D. Ramunno-Johnson, C. Song, B. Amirbekian, Y. Kohmura, Y. Nishino, Y. Takahashi, T. Ishikawa, and J. Miao. *Nanoscale Imaging of Mineral Crystals inside Biological Composite Materials Using X-Ray Diffraction Microscopy.* Phys. Rev. Lett. **100**, 038103 (2008).

[Kan06] H. C. Kang, J. Maser, G. B. Stephenson, C. Liu, R. Conley, A. T. Macrander, and S. Vogt. *Nanometer Linear Focusing of Hard X Rays by a Multilayer Laue Lens.* Phys. Rev. Lett. **96**, 127401 (2006).

[Kle29] O. Klein and Y. Nishina. *Über die Streuung von Strahlung durch freie Elektronen nach der neuen relativistischen Quantendynamik nach Dirac.* Zeitschrift für Physik A **52**, 853–868 (1929).

[Kur05] O. Kurapova. *Development of Nanofocusing Refractive X-Ray Lenses.* Ph.D. thesis, Aachen University (RWTH) (2005).

[Len96] B. Lengeler. *27. IFF-Ferienkurs: Streumethoden zur Untersuchung kondensierter Materie.* Forschungszentrum Jülich, Jülich (1996).

[Mar03] S. Marchesini, H. He, H. N. Chapman, S. P. Hau-Riege, A. Noy, M. R. Howells, U. Weierstall, and J. C. H. Spence. *X-ray image reconstruction from a diffraction pattern alone.* Phys. Rev. B **68**, 140101 (2003).

[Mar07] S. Marchesini. *Phase retrieval and saddle-point optimization.* J. Opt. Soc. Am. A **24**, 3289–3296 (2007).

[Mia99] J. Miao, P. Charalambous, J. Kirz, and D. Sayre. *Extending the methodology of X-ray crystallography to allow imaging of micrometre-sized non-crystalline specimens.* Nature **400**, 342–344 (1999).

[Mia00a] J. Miao, J. Kirz, and D. Sayre. *The oversampling phasing method.* Acta Cryst. D **56**, 1312–1315 (2000).

[Mia00b] J. Miao and D. Sayre. *On possible extensions of X-ray crystallography through diffraction-pattern oversampling.* Acta Cryst. A **56**, 596–605 (2000).

[Mia02] J. Miao, T. Ishikawa, B. Johnson, E. H. Anderson, B. Lai, and K. O. Hodgson. *High Resolution 3D X-Ray Diffraction Microscopy.* Phys. Rev. Lett. **89**, 088303 (2002).

[Mia03a] J. Miao, K. O. Hodgson, T. Ishikawa, C. A. Larabell, M. A. LeGros, and Y. Nishino. *Imaging whole Escherichia coli bacteria by using single-particle x-ray diffraction.* PNAS **100**, 110–112 (2003).

[Mia03b] J. Miao, T. Ishikawa, E. H. Anderson, and K. O. Hodgson. *Phase retrieval of diffraction patterns from noncrystalline samples using the oversampling method.* Phys. Rev. B **67**, 174104 (2003).

[Mia05] J. Miao, Y. Nishino, Y. Kohmura, B. Johnson, C. Song, S. H. Risbud, and T. Ishikawa. *Quantitative Image Reconstruction of GaN Quantum Dots from Oversampled Diffraction Intensities Alone.* Phys. Rev. Lett. **95**, 085503 (2005).

[Mia06] J. Miao, C.-C. Chen, C. Song, Y. Nishino, Y. Kohmura, T. Ishikawa, D. Ramunno-Johnson, T.-K. Lee, and S. H. Risbud. *Three-Dimensional GaN-Ga_2O_3 Core Shell Structure Revealed by X-Ray Diffraction Microscopy.* Phys. Rev. Lett. **97**, 215503 (2006).

[Mil90] R. P. Millane. *Phase retrieval in crystallography and optics.* J. Opt. Soc. Am. A **7**, 394–411 (1990).

[Mil97] R. P. Millane and W. J. Stroud. *Reconstructing symmetric images from their undersampled Fourier intensities.* J. Opt. Soc. Am. A **14**, 568–579 (1997).

[Mil02] D. M. Mills. *Third-Generation Hard X-ray Synchrotron Radiation Sources: Source Properties, Optics, ad Experimental Techniques.* John Wiley & Sons, Inc., New York (2002).

[Mim05] H. Mimura, S. Matsuyama, H. Yumoto, H. Hara, K. Yamamura, Y. Sano, M. Shibahara, K. Endo, Y. Mori, Y. Nishino, K. Tamasaku, M. Yabashi, T. Ishikawa, and K. Yamauchi. *Hard X-ray Diffraction-Limited Nanofocusing with Kirkpatrick-Baez Mirrors.* Jpn. J. Appl. Phys. **44**, L539–L542 (2005).

[Mit98] M. Mitchell. *An Introduction to Genetic Algorithms.* The MIT Press, Cambridge, Massachusetts (1998).

[Nel95] P. D. Nellist, B. C. McCallum, and J. M. Rodenburg. *Resolution beyond the 'information limit' in transmission electron microscopy.* Nature **374**, 630–632 (1995).

[Nel97] P. D. Nellist and J. M. Rodenburg. *Electron Ptychography. I. Experimental Demonstration Beyond the Conventional Resolution Limits.* Acta Cryst. A **54**, 49–60 (1997).

[Nis03] Y. Nishino, J. Miao, and T. Ishikawa. *Image reconstruction of nanostructured nonperiodic objects only from oversampled hard x-ray diffraction intensities.* Phys. Rev. B **68**, 220101 (2003).

[Pat03] J. Patommel. *Entwicklung einer hochauflösenden Kamera für die Mikroskopie mit harter Röntgenstrahlung.* Diplomarbeit, Aachen University (RWTH) (2003).

[Pfe06] M. A. Pfeifer, G. J. Williams, I. A. Vartanyants, R. Harder, and I. K. Robinson. *Three-dimensional mapping of a deformation field inside a nanocrystal.* Nature **442**, 63–66 (2006).

[PIN] `http://www.physikinstrumente.com/en/products/prdetail.php?sortnr=201750`.

[Rob03] I. K. Robinson, C. A. Kenney-Benson, and I. A. Vartaniants. *Sources of decoherence in beamline optics.* Physica B **336**, 56–62 (2003).

[Rod04] J. M. Rodenburg and H. M. L. Faulkner. *A phase retrieval algorithm for shifting illumination.* Appl. Phys. Lett. **85**, 4795–4797 (2004).

[Rod07] J. M. Rodenburg, A. C. Hurst, A. G. Cullis, B. R. Dobson, F. Pfeiffer, O. Bunk, C. David, K. Jefimovs, and I. Johnson. *Hard-X-Ray Lensless Imaging of Extended Objects.* Phys. Rev. Lett. **98**, 034801 (2007).

[Rön95] W. C. Röntgen. *Ueber eine neue Art von Strahlen.* Sitzungsberichte der physikal.-medizin. Gesellschaft page 132 (1895).

[Say98] D. Sayre, H. N. Chapman, and J. Miao. *On the Extendibility of X-ray Crystallography to Noncrystals.* Acta Cryst. A **54**, 232–239 (1998).

[Sch05] C. G. Schroer, O. Kurapova, J. Patommel, P. Boye, J. Feldkamp, B. Lengeler, M. Burghammer, C. Riekel, L. Vincze, A. van der Hart, and M. Küchler. *Hard x-ray nanoprobe based on refractive x-ray lenses.* Appl. Phys. Lett. **87**, 124103 (2005).

[Sel90] J. H. Seldin and J. R. Fienup. *Numerical investigation of the uniqueness of phase retrieval.* J. Opt. Soc. Am. A **7**, 412–427 (1990).

[Sha05] D. Shapiro, P. Thibault, T. Beetz, V. Elser, M. Howells, C. Jacobsen, J. Kirz, E. Lima, H. Miao, A. M. Neiman, and D. Sayre. *Biological imaging by soft x-ray diffraction microscopy.* Proc. Natl. Acad. Sci. U.S.A. **102**, 15343–15346 (2005).

[She04] Q. Shen, I. Bazarov, and P. Thibault. *Diffractive imaging of nonperiodic materials with future coherent X-ray sources.* J. Synchrotron Rad. **11**, 432–438 (2004).

[SIL] `http://www.silson.com`.

[SIN] `http://www.phytron.de/antrieb/index.php`.

[Spe03] J. C. H. Spence, J. S. Wu, C. Giacovazzo, B. Carrozzini, G. L. Cascarano, and H. A. Padmore. *Solving non-periodic structures using direct methods: phasing diffuse scattering.* Acta Cryst. A **59**, 255–261 (2003).

[Thi06] P. Thibault, V. Elser, C. Jacobsen, D. Shapiro, and D. Sayre. *Reconstruction of a yeast cell from X-ray diffraction data.* Acta Cryst. A **62**, 248–261 (2006).

[Tho01] A. C. Thompson and D. Vaughan. *X-Ray Data Booklet.* Lawrence Berkeley National Laboratory, Berkeley, California 94720 (2001).

[Var01] I. A. Vartaniants and I. K. Robinson. *Partial coherence effects on the imaging of small crystals using coherent x-ray diffraction.* J. Phys.: Condens. Matter **13**, 10593–10611 (2001).

[Var03a] I. A. Vartanyants and I. K. Robinson. *Imaging of quantum array structures with coherent and partially coherent diffraction.* J. Synchrotron Rad. **10**, 409–415 (2003).

[Var03b] I. A. Vartanyants and I. K. Robinson. *Origins of decoherence in coherent X-ray diffraction experiments.* Opt. Comm. **222**, 29–50 (2003).

[Var07] I. A. Vartanyants, I. K. Robinson, I. McNulty, C. David, P. Wochner, and T. Tschentscher. *Coherent X-ray scattering and lensless imaging at the European XFEL Facility.* J. Synchrotron Rad. **14**, 453–470 (2007).

[vC34] P. H. van Cittert. *Die wahrscheinliche Schwingungsverteilung in einer von einer Lichtquelle direkt oder mittels einer Linse beleuchteten Ebene.* Physica **1**, 201 (1934).

[vC39] P. H. van Cittert. *Kohaerenz-Probleme.* Physica **6**, 1129 (1939).

[Wil05] G. J. Williams. *Microscopy of gold microcrystals by coherent x-ray diffractive imaging.* Ph.D. thesis, University of Illinois at Urbana-Champaign (2005).

[Wil07] G. Williams, M. Pfeifer, I. Vartanyants, and I. Robinson. *Effectiveness of iterative algorithms in recovering phase in the presence of noise.* Acta Cryst. A **63**, 36–42 (2007).

[Zer38] F. Zernike. *The Concept of Degree of Coherence and its Application to Optical Problems.* Physica **5**, 785 (1938).

Danksagung

Zum Schluss bleibt mir die Ehre, mich bei den vielen Menschen, die mir bei dieser Arbeit geholfen und dazu beigetragen haben, zu bedanken.

Meinem Betreuer, Prof. Dr. Edgar Weckert, möchte ich ganz besonders für die Vergabe dieses aktuellen Promotionsthemas, die vielen Diskussionen und die wertvollen Anregungen danken. Trotz größerer Aufgaben im Rahmen des Petra III-Projektes hatte er immer ein offenes Ohr für die Anliegen eines Doktoranden und war selbst an so manchem Abend oder Wochenende für Diskussion und Planung von Experimenten verfügbar. Nicht zu vergessen sind auch seine persönlichen Einsätze während Messzeiten an der ESRF.
Prof. Dr. Christian Schroer gilt mein herzlicher Dank für viele wissenschaftliche Diskussionen, die Planung und Durchführung von Experimenten sowie für das Mitsuchen von Fehlern im dichten Dschungel-Code. Seine fröhliche, konstruktive und zuversichtliche Art haben zum Entstehen dieser Arbeit sehr viel beigetragen. Außerdem danke ich ihm und Prof. Dr. Wilfried Wurth für die Übernahme der Gutachterrolle bei der Promotion bzw. der Disputation.

Dr. Ivan Vartaniants möchte ich für viele Diskussionen und Ratschläge im Hinblick auf die Durchführung von Beugungsexperimenten mit kohärenter Röntgenstrahlung danken. Seine Erfahrung und Kenntnisse auf dem Gebiet der Phasenrekonstruktion haben die Implementierung und Entwicklung der notwendigen Software sehr erleichtert.
Ein großes Dankeschön möchte ich an Bernd Reime aussprechen. So hat er doch so manchen Tag und manche Stunde während den letzten drei Jahren mit der technischen Entwicklung des CXD-Vakuumtanks und der Verteilung der verschiedensten Aufträge an die unterschiedlichen Werkstätten verbracht. Außerdem danke ich ihm, sowie auch Simone Johnas, für die angenehme Atmosphäre im gemeinsamen Büro.
Besonders wichtig war auch die Mithilfe und Unterstützung von allen Mitarbeitern in den verschiedenen mechanischen Werkstätten des DESY und der Uni Hamburg, insbesondere von den Mitarbeitern der HASYLAB-Werkstatt um Jens Brehling. Auch unter großem zeitlichen Druck wurden die benötigten Teile doch immer noch rechtzeitig zum Experiment fertig.
Viel Unterstützung habe ich auch von der Software-Gruppe um Thorsten Kracht beim Zusammenstellen der elektronischen Hardware für die Steuerung des CXD-Aufbaus erfahren.

Die lithographisch hergestellten Proben für die Experimente an der ESRF wurden von Olga Kurapova und Pit Boye angefertigt. Nicht zu vergessen ist auch die Arbeit von Jens Patommel für die Entwicklung der Steuerungssoftware, die auch beim CXD-

Aufbau Verwendung fand. Seine Hilfsbereitschaft in dringenden Software-Notfällen war sehr beruhigend.

Den Mitarbeitern an Beamline ID01, Christian Mocuta und Hartmut Metzger, sowie an Beamline ID10, Aymeric Robert und Frederico Zontone sei gedankt für ihre Unterstützung während den Messzeiten. Anton Plech und Irina Snigireva haben bei der Präparation der Goldkügelchen-Probe und dessen Charakterisierung geholfen.

Den weiteren Lesern Dr. Ivan Vartaniants und Dr. Adrian Mancuso sei gedankt für das Korrigieren dieser Arbeit.

Desweiteren möchte ich all denjenigen danken, die an dieser Stelle zwar nicht persönlich erwähnt sind, sich aber dennoch für die gute Arbeitsatmosphäre in der Gruppe und im Institut verantwortlich zeigen und damit direkt oder indirekt zum Gelingen dieser Arbeit beigetragen haben.

Meiner Freundin Nina für die Geduld in der Endphase der Doktorarbeit.

Meiner Familie für ihre Unterstützung.